

Electrodynamic Tether Microsats at the Giant Planets

Final Report

Authors: J. R. Sanmartin¹, M. Charro¹, E. Lorenzini², H. Garrett³

Affiliation: Universidad Politécnica de Madrid¹, University of Padua², JPL-NASA³

ACT researcher(s): C. Bramanti and C. Bombardelli

Date: October 2006

Contacts:

Prof. Juan R. Sanmartin
Tel: +34 91 3366302
Fax: +34 91 3366303
e-mail: jrs@faia.upm.es

Advanced Concepts Team
Fax: +31(0)715658018
e-mail: act@esa.int



Available on the ACT website
<http://www.esa.int/act>

Ariadna ID: 05/3203
Ariadna study type: Standard
Contract Number: 19696/05/NL/CB

Electrodynamic tether microsats at the giant planets

Final Report, October 2006

J. R. Sanmartin, M. Charro

Universidad Politécnica de Madrid

C. Bramanti, C. Bombardelli

ESTEC - ESA

Collaborators

E. Lorenzini, University of Padua,

H. Garrett, JPL - NASA

1 – Introduction	p. 2
2 – Jovian mission concepts	p. 8
3 – The environment at Jupiter	p. 14
4 – Tethered-spacecraft capture at Jupiter	p. 19
5 – Constraints on the capture operation	p. 43
6 – Tether deployment, (rotational) dynamics, and power budget	p. 56
7 – Tether-operated Jovian missions	p. 70
8 – Conclusions	p. 98

1 - Introduction

A full study of the giant, complex Jovian system is a central goal in space science. There exists a pressing need for a spacecraft (S/C) to reach into a low orbit around moon *Europa*, as well as around moon *Io* and *Jupiter* itself. The approach here discussed for exploring the Jovian system would involve an electrodynamic (ED) tether, accounting for a moderate fraction of S/C mass, to tap Jupiter's rotational energy for both power and propulsion. The position of perijove and apojove in equatorial and elliptical, prograde orbits, relative to the synchronous or stationary orbit at $a_s = 2.24$ times Jupiter's radius R_J , would be exploited to conveniently make the induced Lorentz force to be drag or thrust, while generating power, and navigating the system. Capture and orbit evolution to visit the moons or acquire circular orbits at Jupiter, Io and Europa would appear possible.

A satellite corotates with its planet at the equatorial circular orbit of radius $a_s \equiv (\mu / \omega^2)^{1/3}$, where μ and ω are the gravitational constant and the spin of the planet. If one could have a corotating atmosphere beyond a_s , satellites in circular orbits of radius $a > a_s$ would be pushed by faster-moving air to higher though slower orbits, air thus exerting thrust rather than drag; the usual drag takes place for satellites at $a < a_s$. This is just a kinetic mechanism driving the planet-satellite system to thermodynamic equilibrium. Considering a small satellite as a mass point, only planet-spin and orbital motion contribute to mechanical energy \mathcal{E}_{mech} and angular momentum H , which can both be written in terms of just a and ω in case of an equatorial orbit. Conservation of angular momentum, $H = const$, determines a relation \mathcal{E}_{mech} vs a that may present a maximum and a minimum farther out, both extrema corresponding to rigid-body motion of the system, i.e., orbital angular velocity being equal to ω . The maximum is always unstable, any kinetic mechanism for dissipation driving the satellite away from rigid-body motion at $a(max)$, on either side of it. (Dissipation is due to tidal forces in case of natural moons; *Pluto's Charon*, has reached the stable \mathcal{E}_{mech} -minimum

of the system, with its spin, which contributes substantially to both ϵ_{mech} and H , being equal to ω , too.) For the comparatively extremely light artificial satellites, the maximum lies at the stationary orbit (the energy minimum lying beyond Universe limits even for multi-ton space stations).

In planets that have both magnetic field B and ionosphere/magnetosphere, an orbiting conductive tether provides an alternative dissipative mechanism. Consider the nonrelativistic equation for transforming the electric field,

$$\bar{E}(tether\ frame) - \bar{E}(plasma\ frame) = \bar{E}_m \equiv (\bar{v} - \bar{v}_{pl}) \wedge \bar{B},$$

where \bar{v} , \bar{v}_{pl} are the velocities of the S/C and the local corotating plasma, respectively. In the highly conductive plasma away from the tether, the electric field will be negligible in the frame moving with the corotating plasma, yielding, in the tether frame, $\bar{E}(outside) = \bar{E}_m$. This outside field will drive a current \bar{I} inside the tether, with $\bar{I} \cdot \bar{E}_m > 0$. Using the above equation for \bar{E}_m and the Lorentz force $L\bar{I} \wedge \bar{B}$, where L is tether length, the net mechanical power of the tether-plasma interaction becomes

$$L\bar{I} \wedge \bar{B} \cdot (\bar{v} - \bar{v}_{pl}) = -L\bar{I} \cdot \bar{E}_m < 0,$$

this lost (negative) power appearing in the tether electric circuit. Clearly, $L\bar{I} \wedge \bar{B} \cdot \bar{v}$ will be positive, corresponding to thrust acting on the tethered S/C, only if \bar{v} is opposite $\bar{v} - \bar{v}_{pl}$; this may be shown to recover the $a > a_s$ condition for thrust. In the case of retrograde orbits, the Lorentz force will be drag whatever the radius a .

The basic requirement for quasisteady ED-tether operation is establishing effective contact, both anodic and cathodic, with the ambient plasma. Electron ejection is not an issue. Hollow cathodes are presently reaching ratios of current to expellant mass-flow-rate as large as 10^2 A / mg s⁻¹ (which is about the charge-to-mass ratio of protons). This results in fully negligible expellant consumption at a hollow cathode (HC); for $B \sim 1$ Gauss and a tether length of tens

of kilometres, the ratio of the Lorentz force to the expellant mass-flow-rate is well over 10,000 km/s, which is several orders of magnitude larger than the exhaust velocity in electrical thrusters. As regards the problem of anodic contact with a highly rarefied plasma, it was solved in 1992 (J.R.Sanmartin, M.Martinez-Sanchez and E. Ahedo, J. Prop. Power **9**, 353 / 1993), when it was proposed that, instead of using a big end-collector, the tether be left bare of insulation, allowing it to collect electrons over the segment coming out polarized positive, as a giant cylindrical Langmuir probe in the orbital-motion-limited (OML) regime. A length-averaged tether current, I_{av} , should then figure in the Lorentz force. Collection can be efficient if the cross-section dimension is thin; the collecting area of a thin bare tether can still be large because the anodic segment may be tens of kilometers long.

The cylindrical geometry allows a final bonus; a thin tape collects the same OML-current as a round wire of equal cross-section perimeter and will be much lighter. The optimal tether is thus characterized by three quite disparate dimensions, $L \gg w$ (*tape width*) $\gg h$ (*tape thickness*). As we shall see, all dimensionless or characteristic numbers, such as a design value for the ratio M_{SC}/m_t (with m_t tether mass and M_{SC} the full SC mass), are independent of width. A tether-system mass can then be scaled up by just using wider tapes. One must just require the width w to be less than 4 times the ambient Debye length and less than twice the electron gyroradius: both conditions are satisfied, say, beyond 1.5 Jupiter radii, for $w < 15$ cm. The spacecraft mass M_{SC} is made up of m_t and two tether-end masses which, for definiteness, we shall take equal.

The Jovian system is a particularly appropriate place to use an ED-tether for thrusting, as well as dragging, with no outside power source. The basic operating conditions require plasma beyond the radius a_s to be *i*) dense enough, and *ii*) corotating with the planet. The stationary orbit for a planet is readily shown to satisfy the relation

$$a_s / R \propto (\rho / \omega^2)^{1/3}.$$

Jupiter has both low mean density ρ and rapid rotation; as a result the stationary orbit lies close to Jupiter, at $a_s \approx 2.24 R_J$ as mentioned, which is one third the relative distance for Earth. Further, the surface magnetic field is ten times greater at Jupiter than at Earth; magnetic stresses are thus 10^2 times greater in Jupiter, and allow for corotating plasma beyond a_s (where the centrifugal-to-gravitational force ratio exceeds unity; equilibrium here, if in absence of magnetic field, would require pressure to increase outwards). A Jovian plasmasphere reaches to about $3.8 R_J$, which is well beyond a_s .

In addition, moon Io is both at a 1:2 *Laplace* resonance with Europa, and ten times relatively closer to its planet than the *Moon* is to Earth ($a_{Io} \approx 5.89 R_J$). This leads to tidal deformations inside Io that produce extreme tectonics and volcanism. Neutral gas continuously ejected by Io is ionized and accelerated by the fast-flowing Jovian magnetosphere, and made to corotate as a giant plasma torus that is denser than the plasmasphere and reaches from about the plasmasphere to Europa, which orbits at $a_{Eu} \approx 9.38 R_J$.

Tether drag/thrust would only be effective within either plasmasphere or torus. The tether current could be (nearly) shut off at convenience by switching off the HCs or plugging a large resistance in the tether circuit; also, the tether can serve as power source whenever an electric load is plugged in its circuit. A substantial amount of energy could be possibly tapped (and used locally or saved for later use) from the giant power developed during the S/C capture and other high-current operations with negligible effect on its dynamics. Current could also be switched on, however, away from those operations to just generate power.

The proposed Jovian tour would exploit the positions of perijove in the orbit coming from Earth (and of perijove/apojove after capture) relative to the ‘drag sphere’ of radius a_s , to exert either drag or thrust; notice that that radius a_s only roughly indicates which type of force applies in case of noncircular orbits. The apojove could be lowered following capture

through a sequence of perijove passes, allowing for frequent flybys of the Galilean moons (Fig. 1). The apojove could also be lowered all the way down to reach a low circular orbit around Jupiter.

With the apojove in the fast-flowing plasma torus, or further down in the outer region of the plasmasphere, switching the tether current off around perijove and on around apojove would produce a sequence of orbits with increasingly higher perijove. With current conveniently on and off it might be possible to finally carry the S/C deep in the torus, allowing Io to capture the SC. Note that period in the sequence of orbits would increase from under to over 1 day, Io's orbital period being only 1.77 days, the entire operation possibly being short in time. Since Io's radius is 1820 km and its 'sphere of influence' against Jupiter is only 7200 km, it may be necessary to finely tune tether-thrust in Io's ionosphere to keep a low orbit stable. In principle, thrusting within the torus might make capturing the S/C into low Europa orbit possible too.

The tether mission concept might result in a direct trip from Earth and in higher data-handling and scientific payload capabilities, and it should allow for a fast manoeuvring, 'free-lunch' tour (using gravity-assist manoeuvres and chemical propulsion sparingly). Since tether performance is dependent on ambient magnetic field and plasma density, the critical phase is S/C capture. Important side issues requiring detailed consideration include ambient model uncertainties; tape heating at high current operation; S/C survival, under radiation, through the inner Jovian belts and around the moons; and constraints on tether spinning, which is required to keep it taut under Jupiter's low gravity gradient and strong lateral Lorentz forces (HCs at each tether end take turns in becoming cathodic as the tether rotates).

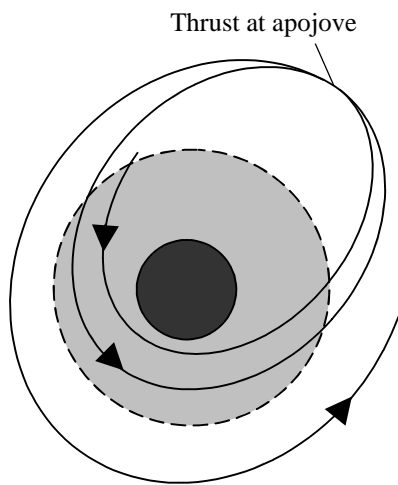
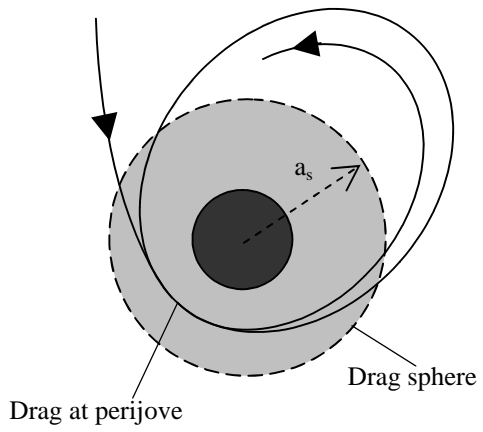


Figure 1. Jovian tour phases: Capture and lowering apojove. Raising perijove.

2 - Jovian mission concepts

Following the *Galileo* mission, the US National Research Council prepared a document on goals and issues as regards planetary exploration, in particular exploration of the Jovian system with emphasis on moon Europa (*New Frontiers in the Solar System: An Integrated Exploration Strategy*, NRC Decadal Survey, 2003). A more recent document was prepared by NASA (*The Solar System Exploration Roadmap*, NASA, July 2006). Basic issues involved are power and propulsion needs, trip times, and harsh radiation environment in the case of Jupiter. Other issues involve data transmission capability, Deep Space Network upgrades, landers, probes.

The successful Galileo mission was a handcuffed mission in the light of the basic issues. The low dry/wet mass fraction for chemical propellants reduced orbital manoeuvring after capture and kept scientific payload to a few percent in mass. Jointly with launcher limitations, the low dry/wet mass fraction led to a protracted trip requiring gravity assist manoeuvres (GAs). The power source used, Radioisotope Thermal Generators (RTGs), was too weak. Capability for data transmission was very low. Though orbiting Jupiter, the Galileo mission might actually be considered as a sequence of moon or Jupiter-perijove flybys.

A variety of proposed approaches to a challenging Jovian mission have rapidly followed each other in time. As early as 1999 the National Research Council made full scientific planning for a mission to Europa, the *Europa Orbiter*, which would use RTG's for power, and chemical propulsion for capture, as in the Galileo mission. The Europa Orbiter (EO), however, would be launched on a direct trajectory to Jupiter, skipping GAs; with wet mass limited by launcher capability, dry mass was just 1000 kg, and payload mass was around 20 kg (average instrument power was 27 w). EO introduced a second novelty: use of gravity assists through a Jovian-moon tour to acquire in several months a low Europa orbit, where it

would stay around 30 days. Radiation tolerant electronics development – computers, avionics, memory – was lagging at the time. NASA cancelled EO in 2001, when in Phase B.

At about that time, NASA embarked in *Project Prometheus*, on the use of nuclear reactors for power, and for powering high specific-impulse electrical thrusters (NEP). The first mission, the *Jovian Icy Moons Orbiter* (JIMO), involved a giant system, with about 1500 kg payload and data capability of 700 MB, ambitiously intended to address a full range of science issues in the Jovian system. JIMO was later changed to a less complex system, *Prometheus 1*, to be launched around 2015, the SC still being 58 m long, its mass lying somewhere between 29 and 36 metric tons. It was deferred indefinitely, later in 2005.

Recently NASA approved *JUNO*, a *New Frontier* mission to Jupiter with more limited goals, to be launched in 2010/2011. JUNO moved a step back to an indirect trajectory, requiring a 5-year cruise. It also pioneered a kind of reversion for outer-planet exploration, replacing RTGs with cell-arrays for solar power. JUNO would be a Jovian polar orbiter, addressing Europa issues in no specific way; the baseline mission involves 32 orbits around Jupiter, with perijove at 5000 km altitude (at distance $1.07 R_J$ from Jupiter's center) and a 11 days period. An assessment of expected radiation dose over sample JUNO orbits is now being carried out, using an updated Divine/Garrett model of radiation to be discussed in Ch. 3.

Late Jet Propulsion Laboratory studies for NASA have reconsidered Europa missions (Europa Exploration: Challenges and Solutions, T.V.Johnson *et al.*, *Lunar and Planetary Science Conference*, March 2006), driving the point that, given chemical-propulsion dry/wet mass fractions and launcher limitations, indirect trajectories, which increase trip time but allow delivering a bigger payload, should be favored: a direct trajectory would allow for 1 ton SC; one Earth GA trajectory would allow 2 tons; combined Venus-Earth GAs, 3 Tons. Science objectives relating first to the *Europa Geophysical Explorer*, then to the *Europa Explorer Concept*, have been discussed within some OPAG subgroup (see below). The EE

concept involves SC dry and wet masses of 2600 kg and 6900 kg (with a launch mass capability over 7200 kg); 8 MM-(Multiple-Mission)-RTGs plus battery; a 900 N bipropellant main engine; 4.5 and 32.5 N monopropellant thrusters; and 180 kg instruments mass (including shielding and contingency). Also, indirect trajectories that allow for mass margins in radiation shielding (along with margins for science and power), advances in radiation hardening that followed developments by US Department of Defense and NASA (during EO/JIMO programs), and better knowledge of the Jovian belts from the Galileo mission, should allow a prime mission of 1.5 years in the Jupiter system plus 3 months in orbit at Europa, with over 3 Mrad(Si) radiation dose (although designed for 0.15 Mrad(Si), Galileo accumulated 0.7 Mrad(Si) at end of its extended mission).

Missions to other Galilean moons have been also considered. The NRC's *Decadal Survey* included a Report from the Io-Community Panel (J. Spencer, lead), updated for OPAG. Io is the most dynamic body in the Solar System (the only place beyond Earth to watch large-scale geology in action), involving from tidal heating to deep magnetospheric effects. EO experience suggested that an Io Orbiter, as proposed in previous roadmaps, would be unrealistic for the entire next decade, while flyby missions appeared insufficient. Best option would be a Jovicentric Orbiter, with multiple flybys of the same hemisphere at 1-month spacing, to provide spatial and temporal coverage. Galileo's flybys had been quite limited, given Io's unique time-variability. As regards radiation, Galileo survived 7 Io flybys, adding 40 krad(Si) each. Use of half the EO hardness (2 Mrad) would allow 50 Io flybys.

A coupled *Ganymede Exploration Orbiter – Jovian System Observer* mission concept, leading to a *Space Physics of Life* proposal (J.F.Cooper *et al.*), would remotely sense the entire Jovian system. Ganymede has an intrinsic magnetic field, and is Laplace-resonant with Europa. Following a flyby of Jupiter and Callisto, a SC would spiral to Ganymede in 3 months, observing Europa for over 5 years from an equatorial, 100 km altitude Ganymede

orbit. It would also serve as relay to the *European Extreme Environment Orbiter with Probes* launched 1 year later, which would spiral into Europa in 3 months to reach a 100 km orbit stable for about 30 days.

NASA's Planetary Science Division chartered the *Outer Planets Assessment Group* (OPAG) in November 2004, with an Europa Subgroup established in 2005 (there exists an Europa Focus Group, dependent on NASA's Astrobiology Institute, outside OPAG). An OPAG, July 2006 Report recommended a mission-size mix (*Flagship, New Frontiers, Discovery*); scientists working closely with mission engineers; and mission concept studies. The Report declared that "Europa is the top-priority science destination in the Outer Solar System", precluding a claim to a prior mission to *Titan-Enceladus*, promoted on the basis of recent *Cassini/Huyghens* results. There is agreement an Europa Orbiter is needed, but getting into Europa is hard: there is little solar flux at the faraway Jovian system, while Europa itself lies in Jupiter's deep gravitational well, embedded in its radiation environment. A mission might involve a 6 years, Earth-Venus-Earth GAs trip to Jupiter; 2-year use of GAs at moons to reduce orbit capture needs; 90 days at an Europa, 100 km, 2 hour period orbit; and 200 kg of scientific instruments.

Propulsion and power issues had been discussed at an OPAG meeting in October 2005. Chemical propulsion appeared as the only current high-thrust option. There is a small gain in moving from bipropellant systems with $I_{sp} \sim 320$ s, to cryogenic bipropellants with $I_{sp} \sim 420$ s, but LH2 storage remained an issue (though being worked on for the VSE return to the Moon); use of LOX-CH4 would be a possibility. Solar Electric Propulsion, well tested in DS-1, is limited by the need for solar arrays; Nuclear Electric Propulsion considered under Project Prometheus is no longer pursued; Radioisotope Electric Propulsion is promising but it needs reducing its specific mass; Solar sails remain elusive, while Aerobraking, as in the

retrograde capture proposed for the *Neptune-Triton* mission – orbiter or flyby, with multiple probes -, requires a well known target atmosphere, and is yet to be demonstrated,

As it regards power, Europa may require 1 kw. Again, solar power, though being used by JUNO, would prove insufficient (there is no present SP program at NASA). Radioisotope Power Sources remain the present option, though both fuel and hardware developments are required. The SiGe thermocouples used from Galileo to the *New Horizons* Pluto's mission, are no longer produced; just a few RTG units, each 290 w, are left. Also, there is little Pu 238 available; the US Department of Energy will start production at the Idaho National Laboratory around 2013, but less than 2.5 kg/year would proceed to NASA. NASA keeps a program to develop high efficiency RPSs by 2013. Specific power above 8 w/kg may be required, as compared with Cassini's 5 w/kg value. Current MMRTGs are too heavy (< 4 w/kg); 2.5 w/kg MMRTGs will be used in Mars. Stirling Radioisotope Generators having high specific power must eliminate EMI noise.

An ESA/NASA working group on exploration of the Jupiter system (not just Europa), which was chartered in June 2005, met in Cambridge-UK in September 05; at UCLA, Dec. 2005; and in Paris, April 2006. Discussions involved EO and JIMO documents, JPL Europa studies, OPAG science requirements, and the ESA concept introduced in ESA's *Cosmic Vision / 2015-2025* (2004), which is somehow equivalent to the NRC's Decadal Survey.

ESA has made plans about a *Jovian Minisat Explorer* (presented by Falkner & Atzei at an OPAG, May 2006 meeting), which would keep some *Galileo* features: chemical-rocket capture at Jupiter, and an indirect 5.9 years trajectory from Earth (VEE GAs, driven by Venus synoptic period). ESA, however, would move from RTGs back to solar power; regarding RTGs, ESA faces ITAR restrictions on US technology, and an ecological worry about problems at Earth flybys, in addition to the limitations NASA itself faces at present. ESA plans to use "Dutch windmill" arrays, and solar concentrators as in Boeing's HS-702

communications satellite. ESA would use GaAs (instead of less efficient Si) *Low Intensity Low Temperature* (LILT) cells. However, only LILT-Si cells (which were considered for JUNO use) have already been developed in Europe; also, exposure to both Venus and Jupiter environments may be hard on cells. In case its solar power program fails, ESA would revert to RTGs.

JME's baseline launch date, on a Soyuz-Fregat 2B (Ariane would perform better but is more expensive), is 2017. Wet mass for chemical propulsion (with SEP backup) would be 3000 kg. After capture by Jupiter the *JME* would split into a *Jovian Relay Satellite* (JRS) and a *Jovian European Orbiter* (JEO). JRS is due to acquire a Jovian elliptical orbit (apojove $26.3 R_J$, perijove $12.7 R_J$) at 3:1 resonance with Europa, in about 450 days, through an extended series of moon GAs. JEO would take 100 days longer in attaining a polar circular orbit, at 200 km altitude above Europa. JRS would both do science and relay JEO data to Earth. JRS operational lifetime could be 2 years, JEO's over 60 days. JEO hardware should be radiation tolerant to 1 Mrad(Si) behind 10 mm aluminium shielding. ESA is developing a Highly Integrated Payload Suites (*HIPS*) program to reduce payload mass; as a bonus, HIPS reduce payload volume and thus shielding mass too. The relay satellite has good potential for cooperation; also, JUNO's focusing on Jupiter itself could appear as complementary to the JME mission. ITAR restrictions would seem to make ESA/NASA collaboration harder than for Cassini, however.

3 - The environment at Jupiter

The model of the Jovian environment that was prepared by N. Divine and H. B. Garrett [*Journal of Geophysical Research* **88**, 6889-6903 (1983)] has served as reference for all Jovian missions following Voyager 1 and 2. It would here serve, in principle, as reference model too. The Divine/Garret (**D/G**) model was basically constructed from *Pioneer* 10 and 11 and Voyager 1 and 2 *in situ* data, supplemented by Earth-based observations of synchrotron emission; it models the magnetic field, and energetic, warm, and thermal populations of charges. However, there have been corrections since, and alternative partial models, which need be examined.

The Jovian regions of most interest for this Study are the plasmasphere (extending as already noticed to $3.8 R_J$ radial distance from Jupiter's center), the Io vicinity and its torus, and the Europa vicinity just beyond. All three regions lie within the so called inner magnetosphere, where the magnetic field is dominantly produced by currents inside Jupiter (see below, however). With a current-free magnetic field, a limited number of measurements can determine dominant terms in a multipole expansion. As a consequence, the variety of magnetic models that have been proposed (O4, O6, VIP4,...) differ little among each other, particularly at low magnetic latitudes, as regards the analysis of interest here. An offset, tilted-dipole model is very suitable except for precise trajectory determinations, but actually a no-tilt, no-offset dipole model will do in our case. The model may fail at radial distances beyond $8 R_J$, where a current sheet starts contributing to the local magnetic field, and at the cold inner region of the torus, at distances less than $5 R_J$, where the torus is thin and its definite location may depend sensibly on the magnetic field model. In either case, the plasma density is so low that, whatever its value, it has little effect on the dynamics of the SC

As regards charge populations, engineering emphasis on all previous mission-concepts was on the energetic particles (radiation), which can severely affect electronic components.

Although radiation will still prove important, the most critical issue in the concept considered here lies in the ambient-electron current collected by the anodic tether segment, which is the fundamental performance number. Since it has a much greater density, the thermal component of the ambient plasma will determine the tether current; current from the other populations can be easily checked out at all stages in the study, however. In the past, thermal plasma models were mainly of interest in discussing magnetospheric physics.

For either type of population, uncertainties are much greater than in the magnetic field case because there is no simple a priori model for the spatial structure of plasma density and temperature. The **D/G** model gives average values and acknowledges uncertainties. Uncertainties, and temporal variations away from average or nominal values, make for a critical issue; a mismatch between model and actual values would be particularly problematic for the capture phase.

As regards radiation, there exist two basic modifications of the **D/G** model, which had originally covered the magnetic shell range $1.09 < L < 16$. Late analysis of data from the Galileo *Energetic Particle Detector* led to modifications over the range $8 < L < 16$, in a so called **GIRE** (*Galileo Interim Radiation Electron*) model, which is freely available on line. **GIRE** does reduce the dose rate, as compared with the **D/G** model, at such important locations as the Europa and Ganymede orbits [H.B.Garrett *et al.*, *Icarus* **178**, 386 / 2005 / (Fig.8); P.Renard *et al.*, *System Concepts...*, IAC-04-Q.2a.02 Paper / 2004 / (Fig,4)]; it leaves the $L < 8$ range (dominant as regards radiation) unmodified, however, and thus has little relative effect on the dose per orbit for orbits that reach very close to Jupiter.

A second modification of the **D/G** radiation model covers the $L < 4$ range, well in the inner magnetosphere. It arised in recent analyses fitting synchrotron emission data from Earth based measurements, and affect relativistic (multi-Mev) electron energies [Garrett *et al.*, *Geophysical Research Letters* **32**, L04104 (2005)]. Again, it hardly affects the electron flux

except in the narrow range $2 < L < 2.3$, and will be ignored here. In the course of either analysis, temporal variations in the radiation environment by a factor 2-3 were found. The study of radiation effects on electronic components, however, is usually an estimate of failure probability, allowing for such variability; the case for tether current collection and thermal plasma is clearly different.

As regards the thermal population, the equatorial **D/G** radial profiles for density and temperature are shown in Fig. 2. Plasmasphere and torus are modelled separately. The model for the plasmasphere, which has the Jovian radius as scale height, arose from early work by L.A.Frank *et al.* (J. Geophys. Res. **81**, 457 / 1976), G.L.Siscoe (J. Geophys. Res. **83**, 2118 / 1978), and D.D.Sentman and C.K.Goertz (J. Geophys. Res. **83**, 3151 / 1978). The model has approximate spherical symmetry and allows for errors of the order of a factor of 2. It will be used throughout Chs. 4-7 for calculations on capture, and its constraints, and on lowering apojove operations; only the plasma density profile, which has a simple analytical representation, as described by Eq.(36) in Ch. 4, is involved in the calculations.

As regards the torus, early 2D models by F.Bagenal, J.D.Sullivan, and G.L.Siscoe (Geophys. Res. Lett. **7**, 41 / 1980) and F.Bagenal and J.D.Sullivan (J. Geophys. Res. **86**, 8447 / 1981) based on Voyager 1 data were used to construct the **D/G** model, which must be adjusted by a later correction arising from a factor of 2 error in published ion temperatures (F.Bagenal *et al.*, J. Geophys. Res. **90**, 1755 / 1985); this results in a torus more extended latitudinally than predicted by the **D/G** model. The radial density profile in the torus, which is actually slightly tilted with respect to the Jupiter equator as discussed in Ch.7, exhibits several peaks and troughs, as seen in Fig.2, which have resulted in a variety of torus-region names (“precipice”, “ribbon”, “ledge”,...); further latitudinal broadening in the “ribbon” region, from $5.7 R_J$ to $5.9 R_J$, was reported by F. Bagenal (J. Geophys. Res. **99**, 11043 / 1994). In general, possible temperature differences among species and possible temperature

anisotropies keep a degree of uncertainty in torus thickness. Later Galileo data suggest plasma density in the torus is higher by a factor of 2 than indicated by Voyager data (F.J.Crary *et al.*, J. Geophys. Res. **103**, 29359 / 1998).

Galileo data also showed that Io itself has a substantial ionosphere, with electron densities at hundreds of kilometers above Io's surface reaching values $\sim 10^5 \text{ cm}^{-3}$, well above the ambient magnetospheric density; and with plasma that arises from Io, and goes into its torus, corotating with the Jupiter's magnetosphere at distances from Io's center as close as 7 times Io's radius, or about 13,000 km only (D.P.Hinson *et al.*, J. Geophys. Res. **103**, 29343 /1998; D.A.Gurnett *et al.*, J. Geophys. Res. **106**, 26225 / 2001). All this might be used for tether fine-tuning of the orbit of a SC at Io, to keep it stable. Galileo data exhibit substantial plasma density enhancements at low altitudes above Europa too (A.J.Kliore *et al.*, Science **277**, 355 / 1997; D.A.Gurnett *et al.*, Geophys. Res. Lett. **25**, 237 / 1998). Quite recent analyses from a Cassini flyby show long term variations in plasma conditions in the Io torus, from the Voyager 1, 2 era, but also monthly and even hourly variations (P.A.Delamere and F. Bagenal, J. Geophys. Res. **108** (A7), 1276 / 2003; A.J. Steffl, A. Ian F. Stewart, and F. Bagenal, Icarus **172**, 78 / 2004).

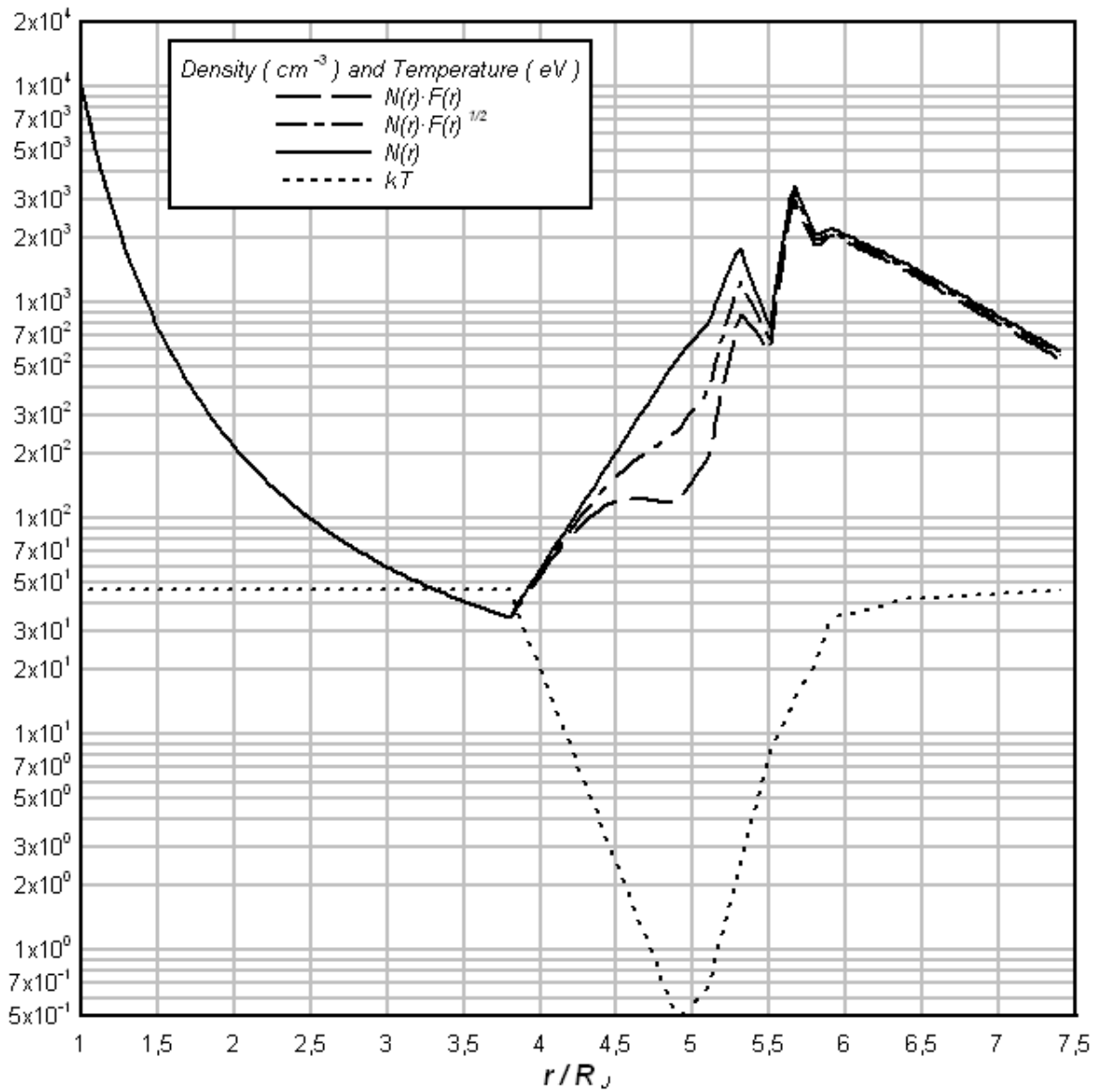


Figure 2. Radial profiles of equatorial electron density (full line) and ion temperature (dotted line), from *Divine and Garrett (1983)*. The dashed and dash-dotted lines correspond to two “mean” (longitude-averaged) densities in the torus, arising from its tilt to the equator (to be discussed in Ch. 7).

4 – Tethered-spacecraft capture at Jupiter

The Jovian tour may start with a spacecraft approaching Jupiter at the relative velocity $v_\infty \approx 5.64$ km/s of a minimum-energy transfer, i.e. a Hohmann transfer when ignoring the 1.3 degrees inclination of Jupiter's orbit with respect to the ecliptic. After capture, closed orbits could evolve substantially under repeated Lorentz force. The critical phase is then the S/C capture. The issue is whether an electrodynamic (ED) tether system, accounting for a moderate fraction of the full S/C mass $M_{S/C}$, is able to perform capture; tether performance is dependent on the actual orbit geometry, which we assume equatorial, and on ambient conditions: plasma electron density N_e , motional electric field \bar{E}_m , and magnetic field B (in a no-tilt, no-offset dipole model, as advanced in Ch.1). Capture is doubly critical for a tether as compared with a mass-consuming thruster, which faces a separate critical issue in achieving closed-orbit evolution.

A simple estimate can relate the (full) S/C -to-tether mass ratio and the eccentricity of the first elliptic orbit after capture. Capture requires drag to make a minimum work W_C to take the orbital energy from a positive value $M_{S/C} v_\infty^2 / 2$ to some negative value, $-\beta \times M_{S/C} v_\infty^2 / 2$

$$M_{S/C} v_\infty^2 / 2 + W_C \rightarrow -\beta \times M_{S/C} v_\infty^2 / 2. \quad (1)$$

This drag work scales roughly as

$$-W_C = (1 + \beta) M_{S/C} v_\infty^2 / 2 \sim L I_{av} B \times r_p \quad (2)$$

where the length-averaged current I_{av} and the field B are characteristic values along the orbit, and r_p is perijove distance. Capture requires β to be positive; the greater is β the lower are the eccentricity and the apojove distance r_a of the orbit following capture.

The current can be estimated from knowledge of the impedances that are part of the tether-current circuit. The contact impedance of the hollow cathode ejecting electrons at the cathodic end will always be negligible. At this point we shall also neglect both the radiation impedance for current closure in the Jovian plasma, which is indeed negligible in Low Earth

Orbit (J.R.Sanmartin and M.Martinez-Sanchez, J. Geophys. Res. **102**, 27257 / 1997), and any power-output impedance, which we will consider in Ch.6. Then, assuming first that the ohmic resistance of the tether is negligible too, bare-tether analysis (to be recalled in Sec. 4.5) shows the tether to be biased positive throughout its length, and the average current to be 2/5 of the orbital-motion-limited (OML) current that would be collected by the tether if at uniform bias $E_m L$,

$$I_{av}(OML) = \frac{2}{5} \times \frac{2w \times L}{\pi} e N_e \sqrt{\frac{2e E_m L}{m_e}}, \quad (3)$$

where E_m is the projection of \bar{E}_m along the tether, which we assumed to be a thin-tape, its cross-section perimeter being twice the width w . Introducing now the tape mass $m_t = \rho_t \times Lwh$, where ρ_t is its density, yields a mass-ratio scaling

$$\frac{-W_C}{m_t v_\infty^2 / 2} = (1+\beta) \frac{M_{SC}}{m_t} \propto N_e \sqrt{E_m} B \times \frac{r_p}{v_\infty^2} \times \frac{L^{3/2}}{\rho_t h}. \quad (4)$$

Although mass, current, and power scale linearly with tape width, the mass ratio itself increases with both tether length and inverse thickness but is independent of w . We note that if, instead of a tape, a round wire were used, its radius would figure in place of the thickness h in Eq.(4), where it should be small, and instead of w/π in Eq.(3), where it should be large; a thin tape, as opposite a round wire, has a cross section with two disparate characteristic lengths, which serves our purposes.

There is a limit to the possible gain in mass ratio by increasing the ratio $L^{3/2}/h$ in Eq.(4) because ohmic effects will set in at some point: the OML / *short-circuit* current ratio

$$\frac{I(OML)}{I(short\ circuit)} \propto \frac{N_e \sqrt{E_m} \times w L^{3/2}}{\sigma_c E_m w h} \quad (5)$$

is also proportional to $L^{3/2}/h$. Increasing this ratio leads ultimately to the maximum current that a tape cross-section can carry, which is just the short-circuit current

$$I_{av} (short\ circuit) = \sigma_c w h E_m, \quad (6)$$

where σ_c is tether conductivity. As we shall discuss in Ch.5, tether length may also be limited by the tensile strength of the tape material.

Consideration of design values for all three r_p , h and L parameters, which is a main purpose in this study, requires a detailed calculation of the mass ratio, going beyond just scaling laws. Such calculation must take into account that the S/C will follow an orbit far from circular during capture. This involves accounting for the facts that ambient conditions vary along the orbit; that the motional field has a complex behaviour (the strict condition $r < a_s \approx 2.24 R_J$ for the Lorentz force to be drag not applyig in case of noncircular orbits, as already noticed); and that the orientation of the tether will be neither normal to the trajectory nor radially away from Jupiter. The fact that the gravity gradient in Jupiter is weak, as noticed in Chap.1, will require to set the tether spinning, a matter to be discussed in Chs. 5, 6 too.

4.1 - Capture by a fast rotating tether in parabolic orbit

A consistent analysis of S/C capture along an orbit that starts hyperbolic and ends elliptic as desired, could involve variations in parameters of conics, this being not too transparent, however. Fortunately the incoming orbit starts barely hyperbolic and may end barely elliptic. The eccentricity e_h of the incoming hyperbolic orbit is very close to unity, which is basically a result of the ratio $M_S R_J / M_J a_J$ being small, and the Jupiter and Earth orbits not being too disparate in size,

$$e_h - 1 = \frac{v_\infty^2 r_p}{\mu_J} \approx \frac{M_S}{a_J} \frac{r_p}{M_J} \times \left(1 - \sqrt{\frac{2 a_E}{a_E + a_J}} \right)^2 \approx 0.018 \frac{r_p}{R_J}; \quad (7)$$

here M_J , μ_J and a_J , are Jupiter's mass, gravitational parameter and semiaxis of orbit around the Sun; a_E is the Earth orbit semiaxis; and M_S is the Sun mass. To examine capture

feasibility we may assume that the S/C is barely captured, with the eccentricity of the elliptic orbit that would follow just below unity, the orbital energy per unit mass ε then being

$$\varepsilon = -\beta \frac{1}{2} v_\infty^2 \equiv -\frac{\mu_J}{2a_1} \equiv -\frac{\mu_J}{2r_p} (1 - e_1) \quad (8a)$$

$$\rightarrow 1 - e_1 = \beta \times (e_h - 1) \approx \beta \times 0.018 r_p/R_J \quad (8b)$$

with $\beta \sim 1$. All this means that, locally, the orbit is hardly affected, and that we can ignore all changes except the dramatic faraway effect of having the orbit changed from open to closed.

We may then introduce a first extraordinary simplification, assuming an undisturbed orbit throughout capture, the bonus being that a parabolic ($e = 1$) orbit fits best the approximation, further simplifying the analysis. The energy and conic equations just read

$$v^2 = 2\mu_J / r, \quad 1 + \cos \theta = 2r_p / r \equiv 2 / \tilde{r}, \quad (9a, b)$$

where we introduced the radius \tilde{r} normalized with its minimum (perijove) value. From Barker's equation, giving time t from perijove pass versus true anomaly θ , we obtain for later use

$$\frac{3}{2} \frac{v_p}{r_p} t = \sqrt{\tilde{r} - 1} (2 + \tilde{r}) \quad \Rightarrow \quad dt = \frac{r_p}{v_p} \frac{\tilde{r} d\tilde{r}}{\sqrt{\tilde{r} - 1}}, \quad (10a, b)$$

where v_p is the velocity at the perijove. We need only consider positive t and θ , the drag work on the symmetrical, $\theta < 0$ arc of trajectory being the same for both arcs. Figure 3 shows the relative orientations of unit vectors along the radial (local vertical) and azimuthal directions, and the outward normal and tangential directions, in the equatorial plane of the orbit. One then has

$$\bar{u}_\theta = \bar{u}_t \sin \alpha_r - \bar{u}_n \cos \alpha_r. \quad (11)$$

The relative velocity determining the motional field that drives the current is then

$$\begin{aligned}\bar{v}' &\equiv \bar{v} - \bar{v}_{pl} \equiv v'_t \bar{u}_t + v'_n \bar{u}_n = \\ &= (v - \omega_J r \sin \alpha_r) \bar{u}_t + \omega_J r \cos \alpha_r \bar{u}_n\end{aligned}\quad (12)$$

Since we have $\omega_J a_s = (\mu_J/a_s)^{1/2}$ the \bar{v}' components along tangent and normal are

$$v'_t = v (1 - \tilde{r} / \tilde{r}_M), \quad v'_n = v \tilde{r} \sqrt{\tilde{r} - 1} / \tilde{r}_M \quad (13a, b)$$

where we used $\sin \alpha_r = 1/\sqrt{\tilde{r}}$ from Eq. (9b), and defined

$$\begin{aligned}\tilde{r}_M &\equiv \sqrt{2} \times (a_s / r_p)^{3/2} \\ &\approx 4.74 (R_J / r_p)^{3/2}.\end{aligned}\quad (14)$$

A positive v'_t value is the condition for the Lorentz force to exert drag on the S/C. Since v'_t vanishes at $r = r_M = a_s \times \sqrt{2} \times \sqrt{a_s/r_p}$, drag may clearly operate well beyond the stationary radius a_s . This is due both to the fact that velocities at a parabolic orbit are corresponding circular velocities times $\sqrt{2}$, and to the fact that the corotational velocity appears in v'_t in Eq.(12) decreased by a factor for the tangential component of the azimuthal unit vector.

Equation (9b) now shows that drag will act beyond $\theta = \pi/2$ in case of a $\tilde{r}_M > 2$ orbit.

Also, the length of orbit arc where drag applies is

$$Arc\ length = r_p \times 2 \int_1^{\tilde{r}_M} \frac{\sqrt{\tilde{r}} d\tilde{r}}{\sqrt{\tilde{r}-1}} = 5.65 R_J \frac{\sqrt{\tilde{r}_M(\tilde{r}_M-1)} + \ln\left(\sqrt{\tilde{r}_M} + \sqrt{\tilde{r}_M-1}\right)}{\tilde{r}_M^{2/3}}, \quad (15)$$

which vanishes at $\tilde{r}_M = 1$ ($r_p \approx 2.82 R_J$) and reaches a maximum at $r_p = R_J$ ($\tilde{r}_M \approx 4.74$).

The time the S/C takes in describing this arc is readily computed from (10a),

$$\Delta t = 2 \times \frac{2r_p}{3v_p} \sqrt{\tilde{r}_M - 1} (2 + \tilde{r}_M) \approx \frac{\tilde{r}_M + 2}{\tilde{r}_M} \times \sqrt{\tilde{r}_M - 1} \times 2.11\ hours, \quad (16)$$

where we used both the parabolic velocity ($v_s = \sqrt{2\mu_J / a_s}$) at a_s and Eq.(14) to write

$$r_p/v_p = a_s \sqrt{2/v_s} \tilde{r}_M \approx 1.58 \tilde{r}_M^{-1} \text{ hours} \quad (v_s \approx 39.8 \text{ km/s}). \quad (17)$$

With the Jovian, no-tilt magnetic field ($-B\bar{k}$, $B > 0$) pointing south at the equator, as indicated in Fig.3, the motional field is now (Fig.4)

$$\bar{E}_m \equiv \bar{v}' \wedge \bar{B} = v' B \bar{u}_E, \quad \bar{u}_E = \frac{v'_n}{v'} \bar{u}_t - \frac{v'_t}{v'} \bar{u}_n, \quad (18a, b)$$

with $v' \equiv |\bar{v}'|$, and the unit vector \bar{u}_E being as shown in Fig.4. In Fig. 5 we present the angle between \bar{u}_E and the (inertially fixed) direction of the perijove, which is sum of the true anomaly and the angle between local vertical and motional field (Figs.3, 4),

$$\theta(\tilde{r}) + \alpha(\tilde{r}, \tilde{r}_M),$$

with α itself sum of angles $\alpha_r(\tilde{r})$ and $\alpha_E(\tilde{r}, \tilde{r}_M)$,

$$\theta = \arccos\left(\frac{2}{\tilde{r}} - 1\right), \quad \alpha = \arcsin\sqrt{\frac{1}{\tilde{r}}} + \arcsin\frac{\tilde{r}_M - \tilde{r}}{\sqrt{\tilde{r}_M^2 - 2\tilde{r}_M\tilde{r} + \tilde{r}^3}}. \quad (19a, b)$$

Note that the motional field \bar{E}_m keeps throughout capture almost antiparallel to the radius vector at perijove, α decreasing accordingly as θ increases.

Although there are limitations (to be discussed in Chap.5) to how fast can the tether rotate we shall now use significant simplifications that result in case of a high enough spin. First, the tether may be assumed kept straight by centrifugal forces. Taking the unit vector \bar{u} , lying along the tether, from the cathodic to the anodic end, that is, in the direction of the conventional current inside the tether, its projection on \bar{E}_m will be positive. We then have (Fig.4)

$$\bar{\mathbf{u}} \cdot \bar{\mathbf{u}}_E = \cos \varphi, \quad \bar{\mathbf{E}}_m \cdot \bar{\mathbf{u}} = v' B \cos \varphi \equiv \frac{E}{m} > 0; \quad (20a, b)$$

it will suffice, for the entire discussion, to consider the rotation of the tether in the range $-\pi/2 < \varphi < \pi/2$. If its angular velocity ω_t is high enough we will, secondly, have

$$\omega_t = d(\theta + \alpha + \varphi) / dt \approx d\varphi / dt, \quad (21)$$

with ω_t nearly constant during the time $\Delta t = \pi / (d\varphi / dt)$. An average (marked as $\langle \rangle$) in the calculations over the tether orientation angle in the range $-\pi/2 < \varphi < \pi/2$ will roughly equal the time-average in the interval Δt , at each position in orbit,

$$\frac{1}{\Delta t} \int_{\Delta t} dt \Rightarrow \int_{-\pi/2}^{\pi/2} \frac{d\varphi}{\pi}. \quad (22)$$

4.2 – Capture under no ohmic-effects

For a first simple analysis we start assuming that the tape is so short or so thick that its electric resistance has indeed negligible effects, corresponding to the OML law of Eq. (3). A vector length-averaged (conventional) current can now be rewritten as

$$\bar{I}_{av} = \frac{2}{5} \frac{2\omega L}{\pi} eN_e \sqrt{\frac{2eL}{m_e} v' B \cos \varphi} \bar{\mathbf{u}} \equiv \bar{I}_{av}(\varphi = 0) \times \sqrt{\cos \varphi} \bar{\mathbf{u}}. \quad (23)$$

The Lorentz force and the corresponding mechanical power are then

$$\bar{\mathbf{F}} = L \bar{I}_{av} \wedge \bar{\mathbf{B}} = L B \times I_{av}(\varphi = 0) \times \sqrt{\cos \varphi} \bar{\mathbf{k}} \wedge \bar{\mathbf{u}}, \quad (24)$$

$$\dot{W} = \bar{\mathbf{v}} \cdot \bar{\mathbf{F}} = v L B \times I_{av}(\varphi = 0) \times \sqrt{\cos \varphi} \bar{\mathbf{k}} \cdot (\bar{\mathbf{u}} \wedge \bar{\mathbf{u}}_t), \quad (25)$$

$$\bar{\mathbf{u}} \wedge \bar{\mathbf{u}}_t = -\bar{\mathbf{k}} (\sin \alpha_E \cos \varphi + \cos \alpha_E \sin \varphi). \quad (26)$$

Averaging over the angle φ at fixed r , with

$$\langle (\cos \varphi)^{3/2} \rangle \approx 0.556, \quad \langle \sqrt{\cos \varphi} \sin \varphi \rangle = 0, \quad (27a, b)$$

and using

$$v' \sin \alpha_E = v'_t \quad (28)$$

as seen in Fig. 4, one finds

$$\langle \dot{W} \rangle = - \frac{4\sqrt{2} \times 0.556}{5\pi} \times wL^2 eN_e B \times \sqrt{\frac{eBL}{m_e}} \times \frac{vv'_t}{\sqrt{v'}}. \quad (29)$$

Taking v'_t from Eq.(13a) we can write in a simple way,

$$vv'_t = v^2 - \omega_J r_p v_p. \quad (30)$$

Integrating next over the time on the full drag arc, using Eq.(10b), we obtain

$$W_C = \int \langle \dot{W} \rangle dt = -2 \int_1^{\tilde{r}_M} \frac{r_p}{v_p} \frac{\tilde{r} d\tilde{r}}{\sqrt{\tilde{r}-1}} \times 0.20 \times wL^2 eN_e B \sqrt{\frac{eBL}{m_e}} \times \frac{v^2 - \omega_J r_p v_p}{(v'_t{}^2 + v'_n{}^2)^{1/4}}. \quad (31)$$

Introducing this result in Eq.(1) we finally find an exact form for Eq.(4),

$$\frac{-2W_C}{m_t v_\infty^2} = (1+\beta) \times \frac{M_{SC}}{m_t} = 0.80 \times \frac{m_e f_N N_s a_s}{\rho_t h} \times \frac{\sqrt{v_s} (eB_s L / m_e)^{3/2}}{v_\infty^2} \times \Sigma \left(\frac{r_p}{R_J} \right) \quad (32)$$

$$\Sigma(\tilde{r}_M) \equiv \frac{\tilde{r}_M^2}{2^{5/4}} \int_1^{\tilde{r}_M} \frac{\tilde{r}_M - \tilde{r}}{\sqrt{\tilde{r}-1}} \times \frac{d\tilde{r}}{\tilde{r}^{17/4}} \times \frac{\exp \left[3.43 \left\{ (\tilde{r}_M^{2/3} / 2^{1/3} \tilde{r}) - 1 \right\} \right]}{\left[\tilde{r}_M^2 - 2\tilde{r}_M \tilde{r} + \tilde{r}^3 \right]^{1/4}}, \quad (33)$$

with $\tilde{r}_M (r_p/R_J)$ given by Eq. (14).

To obtain Eqs.(32) and (33) we used Eqs. (9a) and (14) to write

$$v = v_s \tilde{r}_M^{1/3} / 2^{1/6} \sqrt{\tilde{r}}, \quad (34)$$

and used both a no-tilt, no-offset dipole model of the magnetic field,

$$B = B_s \tilde{r}_M^2 / 2 \tilde{r}^3 \quad (B_s \approx 0.38 \text{ gauss}), \quad (35)$$

and, following the discussion in Ch. 3, the Divine-Garrett model of the thermal electron density in the plasmasphere, which approximately reads

$$N_e = f_N \times N_0 e^{r_0/r} = f_N \times N_s \exp \left[\frac{r_0}{a_s} \left(\frac{\tilde{r} M^{2/3}}{2^{1/3} \tilde{r}} - 1 \right) \right], \quad (36)$$

$$r_0 = 7.68 R_J, \quad N_0 = 4.65 \text{ cm}^{-3} \quad \Rightarrow \quad N_s \approx 1.44 \times 10^2 \text{ cm}^{-3},$$

for zero latitude. We introduced a factor f_N in the model to allow both a nominal value $f_N = 1$ and the estimated factor-of-two uncertainty ($1/2 < f_N < 2$).

Taking an aluminum tape and $v_\infty = 5.64 \text{ km/s}$, Eq. (32) now reads

$$(1+\beta) \times \frac{M_{SC}}{m_t} \approx 0.15 \times \lambda^{3/2} \times \Sigma \left(\frac{r_p}{R_J} \right), \quad (37a, b)$$

$$\lambda \equiv \left(f_N \frac{0.05 \text{ mm}}{h} \right)^{2/3} \times \frac{L}{50 \text{ km}}$$

Figure 6 shows $\Sigma(r_p / R_J) \times 0.15/2$, which is just the mass ratio $M_{S/C}/m_t$ in case $\beta \approx \lambda = 1$. Note its extremely rapid growth as the perijove is placed closer to Jupiter; it vanishes at $r_p = 2.82 R_J$ and reaches a maximum (with $\Sigma \approx 647.5$) at $r_p = R_J$. By just moving the perijove from $1.5 R_J$ ($\Sigma \approx 9.96$) to $1.2 R_J$ ($\Sigma \approx 89.5$), say, the mass ratio may be increased by a factor of 9. For $r_p = 1.2 R_J$ and $\lambda = 1$ ($L = 50 \text{ km}$, $h = 0.05 \text{ mm}$, $f_N = 1$, say), the tether could capture a S/C of full mass up to 13.4 times its own mass (into a first orbit, following capture, barely elliptical, $\beta \approx 0$). Note, however, that for this numerical result to be valid one must first check that ohmic effects are negligible for such long, thin tape. Also, as we shall see in Ch. 5, a perijove too close to Jupiter may arise spinning and heating issues.

4.3 - Dominant ohmic-effects limit

Consider next the limit opposite that of the previous section. Making use of the short-circuit law (6), the current vector can now be written as

$$\bar{I}_{av} = \sigma_c wh v' B \cos \varphi \times \bar{u}. \quad (38)$$

The Lorentz force and the corresponding mechanical power are then

$$\bar{F} = L \bar{I}_{av} \wedge \bar{B} = L B \sigma_c wh v' B \cos \varphi \times \bar{k} \wedge \bar{u}, \quad (39)$$

$$\dot{W} = \bar{v} \cdot \bar{F} = v L B \sigma_c wh v' B \cos \varphi \times \bar{k} \cdot (\bar{u} \wedge \bar{u}_t), \quad (40)$$

with $\bar{u} \wedge \bar{u}_t$ given in Eq.(26). Using Eqs.(27) and (30), and the average $\langle \cos^2 \varphi \rangle = 1/2$, yields

$$\langle \dot{W} \rangle = - \frac{1}{2} \sigma_c L wh B^2 (v^2 - \omega_{Jp}^2 r_p v_p). \quad (41)$$

We finally find

$$W_C = \int \langle \dot{W} \rangle dt = - 2 \int_1^{\tilde{r}_M} \frac{r_p}{v_p} \frac{\tilde{r} d\tilde{r}}{\sqrt{\tilde{r}-1}} \times \frac{1}{2} \times \sigma_c L wh B^2 (v^2 - \omega_{Jp}^2 r_p v_p), \quad (42)$$

and

$$\frac{-2W_C}{m_t v_\infty^2} = (1 + \beta) \times \frac{M_{SC}}{m_t} = \frac{\sigma_c B_s^2 a_s v_s}{2^{5/6} \rho_t v_\infty^2} \times S_\infty \left(\frac{r_p}{R_J} \right), \quad (43)$$

where

$$S_\infty \left[\tilde{r}_M \left(\frac{r_p}{R_J} \right) \right] \equiv \tilde{r}_M^{8/3} \times \int_1^{\tilde{r}_M} \frac{(\tilde{r}_M - \tilde{r}) d\tilde{r}}{\tilde{r}^6 \sqrt{\tilde{r}-1}}. \quad (44)$$

Again, for an aluminum tether and $v_\infty = 5.64$ km/s, Eq.(43) reads

$$(1 + \beta) \times \frac{M_{SC}}{m_t} = 2.11 \times S_\infty \left(\frac{r_p}{R_J} \right). \quad (45)$$

Figure 7 shows $S_\infty(r_p / R_J) \times 2.11 / 2$, which is just the mass ratio $M_{S/C}/m_t$ in case $\beta = 1$. Again, S_∞ is a rapidly growing function of r_p / R_J ; it vanishes at $r_p \approx 2.82 R_J$ and reaches a maximum ($S_\infty = 178.0$) at $r_p = R_J$. Moving the perijove from $1.5 R_J$ ($S_\infty = 14.25$) to $1.2 R_J$ ($S_\infty = 59.0$) increases the mass ratio by a factor of 4. For $r_p = 1.2 R_J$, a tether, if indeed in the dominant-resistance limit, could capture a S/C of full mass up to 124.5 times the tether own mass (into an orbit, following capture, barely elliptical, $\beta \approx 0$).

As already noticed, Eq. (32) is valid for $L^{3/2}/h$ low enough; in general, it gives an upper bound to the mass ratio. Similarly, Eq.(43) is valid for $L^{3/2}/h$ high enough; it gives an upper bound to the mass ratio, too. Figure 8 is a sketch showing how either bound depends on $\lambda \propto L/h^{2/3}$ as defined in Eq.(37b). Notice that neither plasma electron density nor tether geometry appears in Eq.(43). Since there is very little uncertainty in the ambient magnetic field in the inner magnetosphere, as discussed in Chap.3, Eq.(42) is a very powerful result. It strongly suggests that S/C capture could be successful in Jupiter, although a complete calculation, to be carried out next, must involve both tether resistance and bare-tether anodic collection impedance from start.

4. 4 - The case for Saturn

Equation (43) is a powerful tool to discuss whether a S/C could be reasonably captured by a tether at Saturn. Using

$$B_s \approx B_{sf} \times (R / a_s)^3, \quad \mu \propto \rho R^3, \quad (46a, b)$$

for either Jupiter or Saturn, with ρ and B_{sf} being mean density of the planet and magnetic field at its surface, we have

$$B_s^2 a_s v_s \propto B_{sf}^2 \times (R/a_s)^{11/2} \times R^2 \times \sqrt{\rho} \propto B_{sf}^2 \omega^{11/3} R^2 / \rho^{4/3}$$

where we used $\omega^2 a_s^3 = \mu_J \propto R^3 \rho$. With the magnetic field at the Saturn's surface about 1/20 of the corresponding value at Jupiter, and using the Saturn-to-Jupiter ratios for rotation speed, size and density, the factor 2.11 in Eq.(45) would become in case of Saturn, if keeping an aluminum tether,

$$2.11 \times \left(\frac{5.64 \text{ km/s}}{v_\infty} \right)^2 \times \left(\frac{1}{20} \right)^2 \times \left(\frac{0.410}{0.426} \right)^{11/3} \times \left(\frac{6.03}{7.14} \right)^2 \times \left(\frac{1.31}{0.69} \right)^{4/3} \approx 0.0098 \times \left(\frac{5.64 \text{ km/s}}{v_\infty} \right)^2.$$

Even for an incoming grazing orbit, $r_p = R$, we would have a mass ratio barely above unity ($M_{SC}/m_t \approx 1.74$ with $\beta \approx 0$ and $v_\infty \sim 5.6$ km/s). Superconductive tether material, as in Alfven's old scheme for solar-wind thrusting, appears necessary though possibly not sufficient for use in Saturn.

4.5 – Capture in the general case

In both drag and power generation operations, the electron current I on a bare tether starts from zero at the anodic end A and increases with distance s from A as electrons collected under the OML law,

$$\frac{dI}{ds} = \frac{2w}{\pi} eN_e \sqrt{\frac{2e\Delta V}{m_e}} \quad (\Delta V > 0), \quad (47)$$

pile up over the segment at bias ΔV positive with respect to the local plasma (Fig.9). The difference between ohmic and induced-voltage drops makes tether bias decrease at a rate,

$$\frac{d\Delta V}{ds} = \frac{I}{\sigma_c hw} - E_m, \quad E_m = v' B \cos \varphi \quad (48)$$

the rate itself decreasing as current increases, and vanishing where, and if, the current reaches the short-circuit value $\sigma_c E_m wh$. Also, since bias must be negative at the cathodic end C to

allow some device to eject electrons, there exists a point B where ΔV vanishes, the segment BC in Fig. 9 being at negative bias.

To analyze Eqs.(47), (48), one introduces a length L^* defined by the condition that a tether of such length, at uniform bias $E_m L^*$, would collect the short-circuit current (aside from a factor to just simplify the resulting dimensionless equations)

$$\frac{4}{3} e N_e \frac{2 w L^*}{\pi} \sqrt{\frac{2 e E_m L^*}{m_e}} \equiv \sigma_c E_m w h \Rightarrow L^* \propto E_m^{1/3} \times \left(\frac{\sigma_c h}{N_e} \right)^{2/3}. \quad (49)$$

The length L^* clearly gauges the bare-tether collection impedance against tether resistance.

Defining dimensionless variables,

$$s/L^* \equiv \xi, \quad \Delta V / E_m L^* \equiv \psi, \quad I / \sigma_c E_m w h \equiv i, \quad (50a, b, c)$$

Eqs.(47), (48) read

$$\frac{di}{d\xi} = \frac{3}{4} \sqrt{\psi} \quad (\xi < \xi_B), \quad \frac{d\psi}{d\xi} = i - 1 \quad (47') - (48'),$$

which have an immediate first integral (J.R.Sanmartin, M.Martinez-Sanchez and E. Ahedo, J. Prop. Power **9**, 353 / 1993)

$$\psi^{3/2} + 2i - i^2 = \psi_A^{3/2} = 2i_B - i_B^2. \quad (51)$$

Using (51) in Eq.(48') one finds

$$\xi = \int_{\psi}^{\psi_A} \frac{d\psi'}{\sqrt{1 - \psi_A^{3/2} + \psi'^{3/2}}} \leq \xi_B = \int_0^{\psi_A} \frac{d\psi'}{\sqrt{1 - \psi_A^{3/2} + \psi'^{3/2}}}. \quad (52)$$

Along the segment BC electrons leak out at the OML rate of impact of ions, which leave as neutrals,

$$\frac{di}{d\xi} = -\frac{3}{4} \sqrt{|\psi|} \times \sqrt{m_e / m_i} \quad (\xi_B < \xi < \xi_C), \quad (53)$$

where we ignored secondary yield.

For just drag or thrust, with no power load at C, its negative bias is the hollow-cathode bias, which, as already noticed, is comparatively very small. This simplifies the calculation of the average current,

$$i_{av} = I_{av} / \sigma_c E_m w h. \quad (50'c)$$

From Eq.(48') one readily finds

$$i_{av} \hat{L} \equiv \int_0^{\hat{L}} i(\xi) d\xi = \hat{L} + \int_0^{\hat{L}} (i-1) d\xi \approx \hat{L} - \psi_A \quad (\hat{L} \equiv L/L^* = \xi_C) \quad (54)$$

having set $|\psi_C| \approx 0$. Over the segment BC current collection is doubly small because of the mass ratio in (53) and because we have $|\psi| < |\psi_C|$ throughout, allowing to write (Fig. 9)

$$i \approx i_B \approx i_C \quad (\xi_B < \xi < \xi_C). \quad (55)$$

To determine $\psi_A(\hat{L})$, consider first the current $i_B = 1$, corresponding to values $\psi_A = 1$ and $\xi_B = 4$ (that is, a length $4L^*$ for the segment AB) in Eqs.(51) and (52). We then have both ψ and $d\psi/d\xi$ vanishing at B. Equations (48') and (55) now yield $\psi = const = 0$ and $i = const = 1$ throughout the segment BC, whatever its length; hence, we have $\psi_A = 1$ for any value $L > 4L^*$. Next consider values $i_B < 1$ ($\psi_A < 1$, $\xi_B < 4$). Integrating Eq.(48') from B to C would give $0 \approx (1 - i_B) \times (\hat{L} - \xi_B)$, requiring a negligibly short cathodic segment BC in Fig.9; for any length $L < 4L^*$, the bias at A will satisfy the condition $\xi_B(\psi_A) \approx L/L^*$, where ξ_B is given in (52). From Eq.(54) we finally find

$$i_{av}(\hat{L}) = 1 - \psi_A(\hat{L})/\hat{L}, \quad (56)$$

with $\psi_A(\hat{L})$ given by

$$\int_0^{\psi_A} \frac{d\psi}{\sqrt{1 - \psi_A^{3/2} + \psi^{3/2}}} = \hat{L} \leq 4; \quad \psi_A = 1, \quad \hat{L} \geq 4. \quad (57a, b)$$

Next, introducing $E_m = B v' \cos \varphi$ in Eq.(50) we have

$$\hat{L}^{3/2} = \frac{8\sqrt{2} e N_e}{3\pi \sigma_c h} \sqrt{\frac{e L^3}{m_e B v' \cos \varphi}}. \quad (58)$$

Using Eqs.(13) and (34)-(36) for v' , B and N_e , we then arrive at $\hat{L}(\lambda, \tilde{r}_M, \tilde{r}, \varphi)$,

$$\hat{L}^{3/2} = \frac{0.0583 f_N}{\sqrt{\cos \varphi}} \times \frac{e N_s}{\sigma_c h} \times \sqrt{\frac{e L^3}{m_e v_s B_s}} \times \left[\frac{\tilde{r}^{7/4}}{\tilde{r}_M^{2/3}} \times \frac{\exp(2.72 \tilde{r}_M^{2/3} / \tilde{r})}{(\tilde{r}_M^2 - 2\tilde{r}_M \tilde{r} + \tilde{r}^3)^{1/4}} \right], \quad (58')$$

showing $\hat{L} \propto \lambda / (\cos \varphi)^{1/3} \sigma_c^{2/3}$ with λ as introduced in Eq.(37b). Now, writing $I_{av} = \sigma_c E_m w h \times i_{av}$, Eqs. (39) and (41) become

$$\bar{F} = L \bar{I}_{av} \wedge \bar{B} = i_{av} L B \sigma_c w h v' B \cos \varphi \bar{k} \wedge \bar{u}, \quad (39')$$

$$\langle \dot{W} \rangle = -\sigma_c L w h B^2 (v^2 - \omega_J r_p v_p) \langle i_{av} \cos^2 \varphi \rangle, \quad (41')$$

Eqs. (42-45) then reading

$$W_C = \int \langle \dot{W} \rangle dt = -2 \int_1^{\tilde{r}_M} \frac{r_p}{v_p} \frac{\tilde{r} d\tilde{r}}{\sqrt{\tilde{r}-1}} \sigma_c L w h B^2 (v^2 - \omega_J r_p v_p) \langle i_{av} \cos^2 \varphi \rangle \quad (42')$$

$$\frac{-2W_C}{m_t v_\infty^2} = (1 + \beta) \times \frac{M_{SC}}{m_t} = \frac{\sigma_c B_s^2 a_s v_s}{2^{5/6} \rho_t v_\infty^2} \times S\left(\lambda, \frac{r_p}{R_J}\right) \quad (43')$$

$$\Rightarrow 2.11 \times S\left(\lambda, r_p / R_J\right), \quad (45')$$

$$S\left[\lambda, \tilde{r}_M\right] \equiv \tilde{r}_M^{8/3} \times \int_1^{\tilde{r}_M} \frac{(\tilde{r}_M - \tilde{r}) d\tilde{r}}{\tilde{r}^6 \sqrt{\tilde{r}-1}} \times \langle 2 \cos^2 \varphi \times i_{av} [\hat{L}(\lambda, \tilde{r}_M, \tilde{r}, \varphi)] \rangle. \quad (44')$$

Note that in the limit $\lambda \rightarrow \infty$, corresponding to dominant ohmic effects, we have $\hat{L} \rightarrow \infty$, $i_{av} \rightarrow 1$ in Eqs.(56), (57b) and (58'), thus readily recovering S_∞ in (44). Also, for λ small enough, \hat{L} will be small over most of the φ -range, leading in Eqs.(56), (57a) to

$$i_{av} \approx 0.3 \hat{L}^{3/2}, \quad \hat{L} \ll 1; \quad (59)$$

Eqs. (43'), (44') and (58') can be shown to then recover Eq.(32), (33), independent of conductivity σ_c , for the no ohmic-effects limit. Figure 10 represents $S(r_p/R_J) \times 2.11/2$, which is just the mass ratio in case $\beta = 1$, for several λ values. Note that a tether with λ as low as 0.63 could capture a S/C with ratio $M_{SC}/m_t > 7$ by having its perijove at $1.2 R_J$. Note, however, the provisos at the end of Sec. 4-2.

4.6 – Brief conclusions

At this point we can briefly summarize some preliminary conclusions:

- Calculations for a fast rotating tape-tether, with the orbital arc of capture approximated as parabolic, yield simple results relating the captured SC mass and the orbit eccentricity after capture.
- A tether would appear incapable of capturing a SC into an orbit around Saturn.
- On the contrary, a tether representing a moderate fraction of the full SC mass appears capable of capturing its SC into orbit around Jupiter. Capture will require a perijove very close to Jupiter unless the tape is long and thin enough.
- The tethered-SC mass just scales with tape width.
- Uncertainty in the plasma density in the inner plasmasphere (as reflected in the range $1/2 < f_N \leq 2$ for the factor introduced in the Divine-Garrett profile) may be a source of problems. To ensure capture for f_N in the low end of the range may require choosing too low a perijove,

and too long and thin a tape; if f_N falls actually at the high end of the range, resulting high values of current and power might lead to significant thermal and stress effects on the tether.

- Values of the parameter $\lambda \propto L/h^{2/3}$ introduced in Eq.(37b) about unity correspond to small ohmic effects (see Fig.10). The cross section need then not be all conductive; this might be made use of for mass reduction, stress resistance and thermal control purposes.

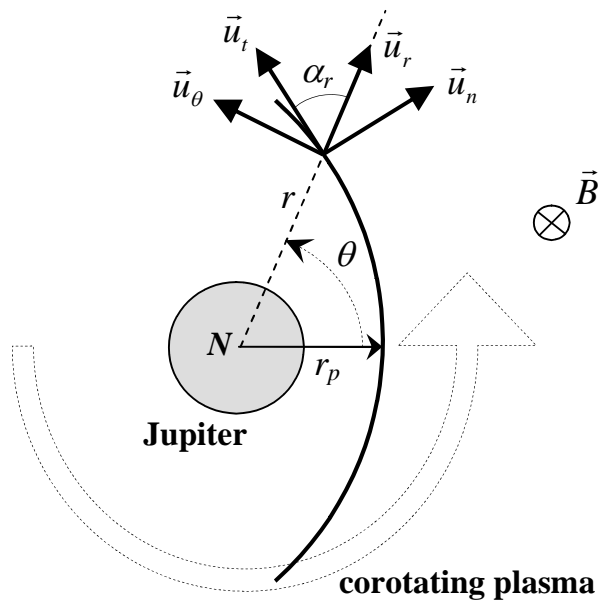


Figure 3. Schematics of geometry in equatorial parabolic orbit with magnetic field tilt ignored; $\alpha_r = \arcsin \sqrt{1/\tilde{r}}$.

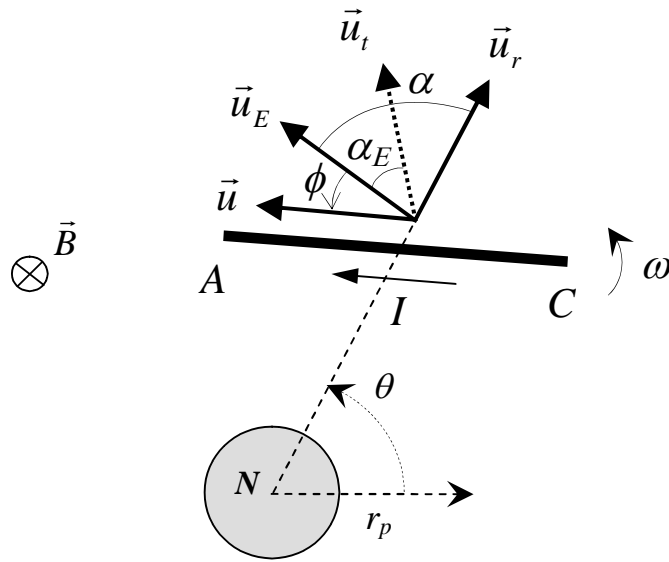


Figure 4. Relative positions of unit vectors for motional electric field and spinning tether, as in Fig.3; A and C are the anodic and cathodic ends, respectively.

$$\alpha_E = \arcsin \frac{\tilde{r}_M - \tilde{r}}{\sqrt{\tilde{r}_M^2 - 2\tilde{r}_M\tilde{r} + \tilde{r}^2}}, \quad \alpha = \alpha_r + \alpha_E$$

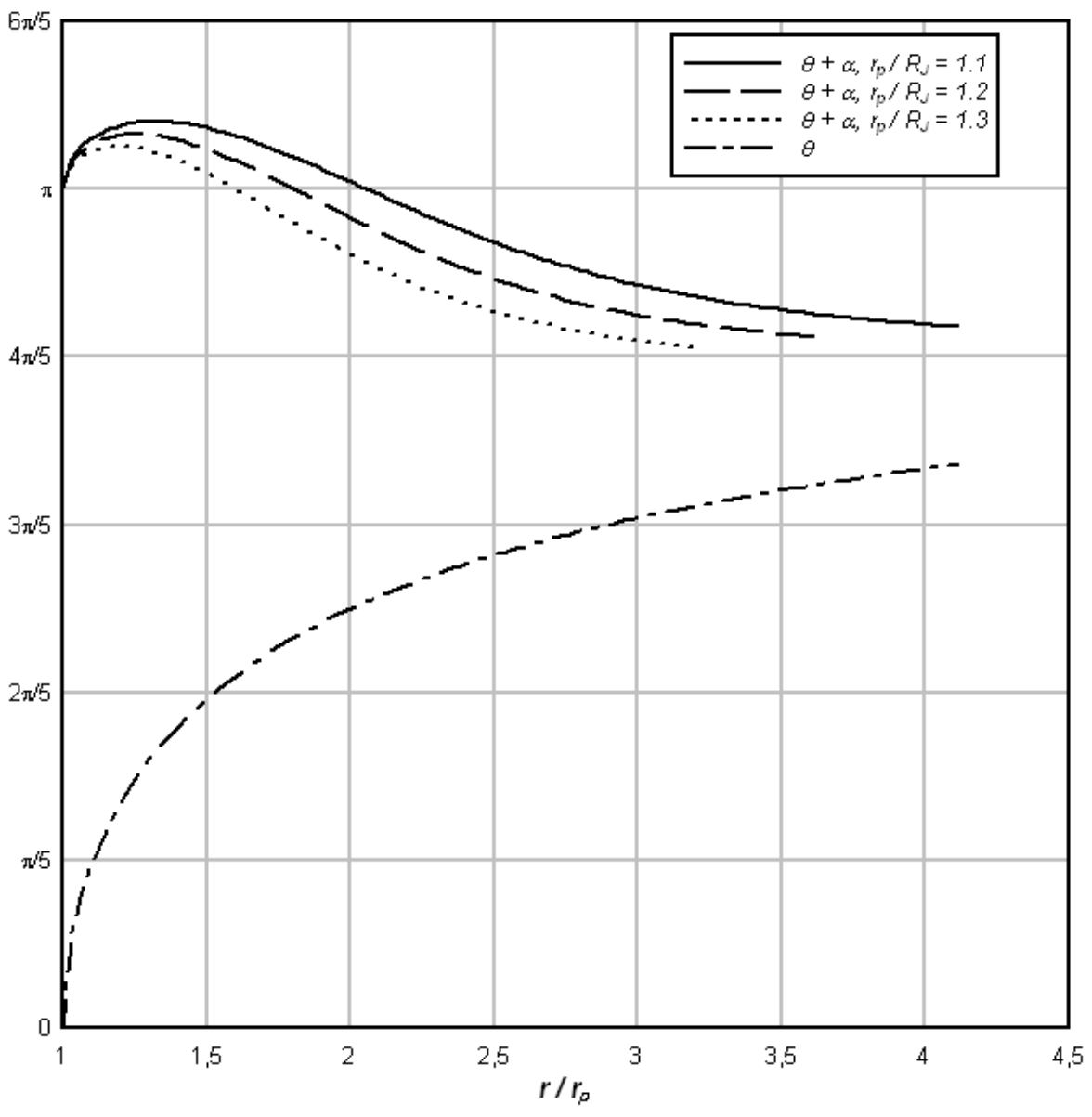


Figure 5. Variations along the drag arc of both anomaly θ and sum of anomaly and angle between motional field and local vertical, $\theta + \alpha$.

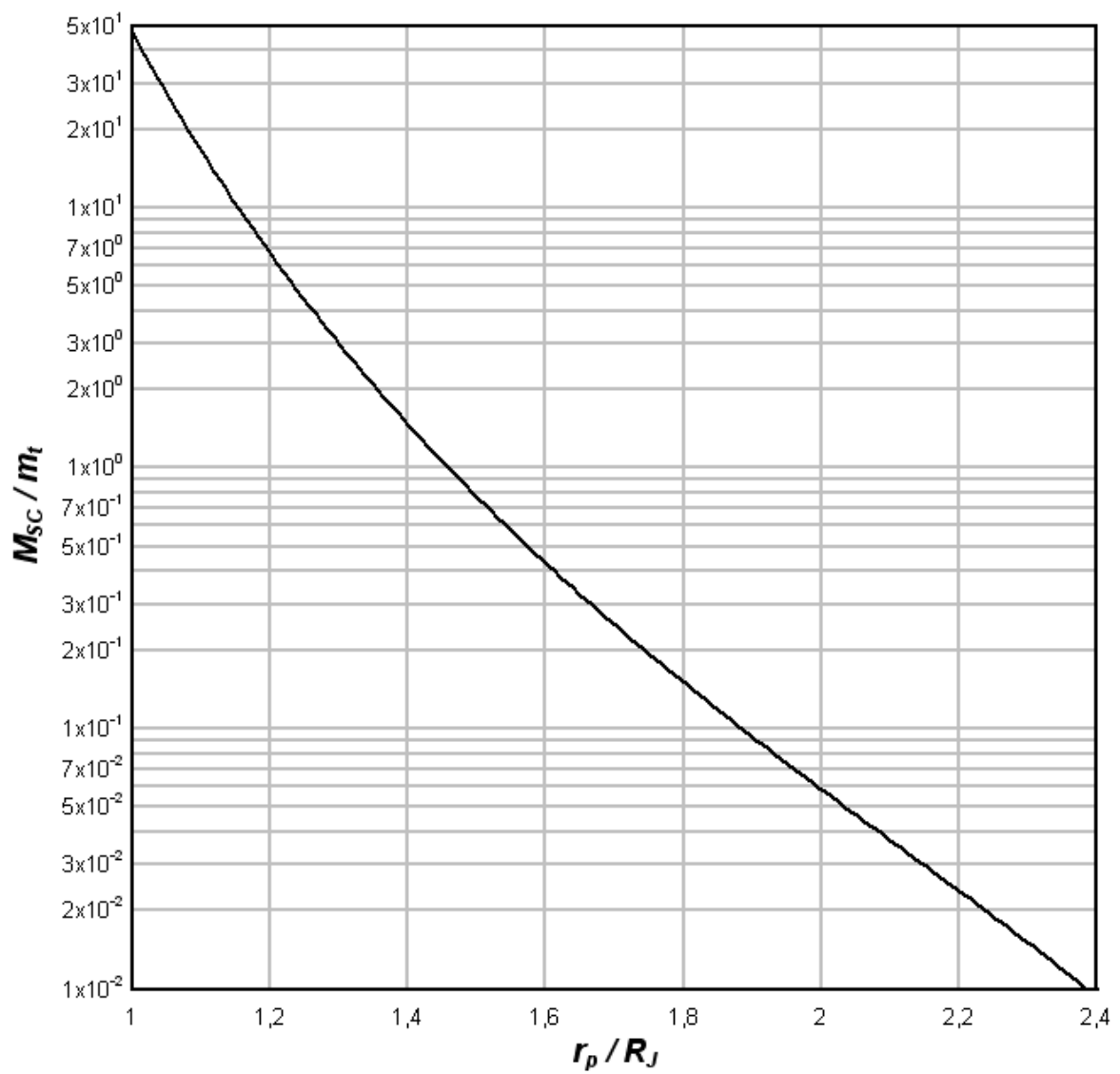


Figure 6. Mass-ratio versus perijove position for no ohmic effects, and $\beta = \lambda = 1$ in Eq. (37a); parameters β and λ defined in Eqs. (1) and (37b). The mass ratio scales as $\lambda^{3/2} \times 2 / (1 + \beta)$.

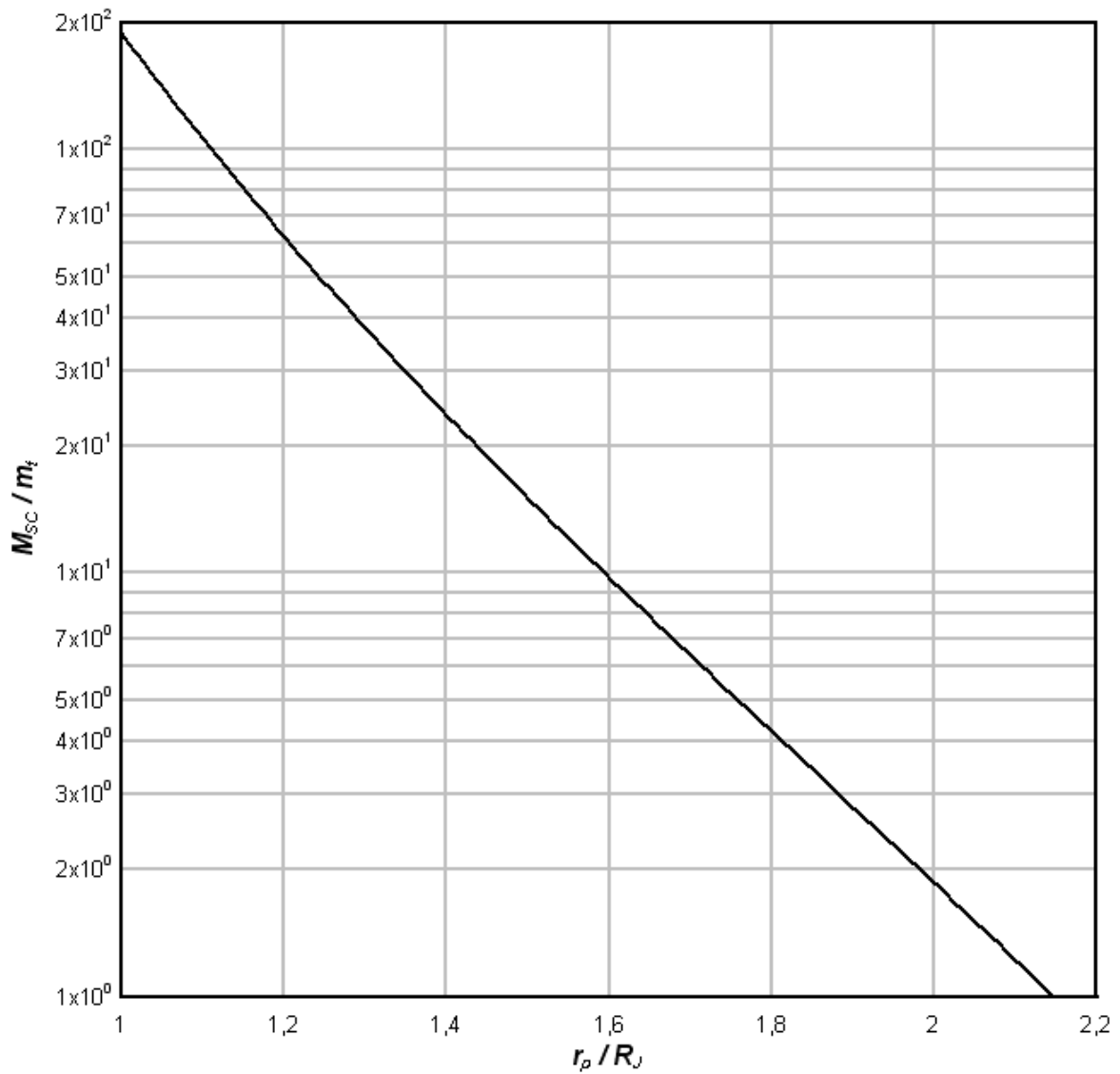


Figure 7. Mass-ratio versus perijove position for dominant ohmic effects and $\beta = 1$ in equation (43). The mass ratio scales as $2 / (1 + \beta)$.

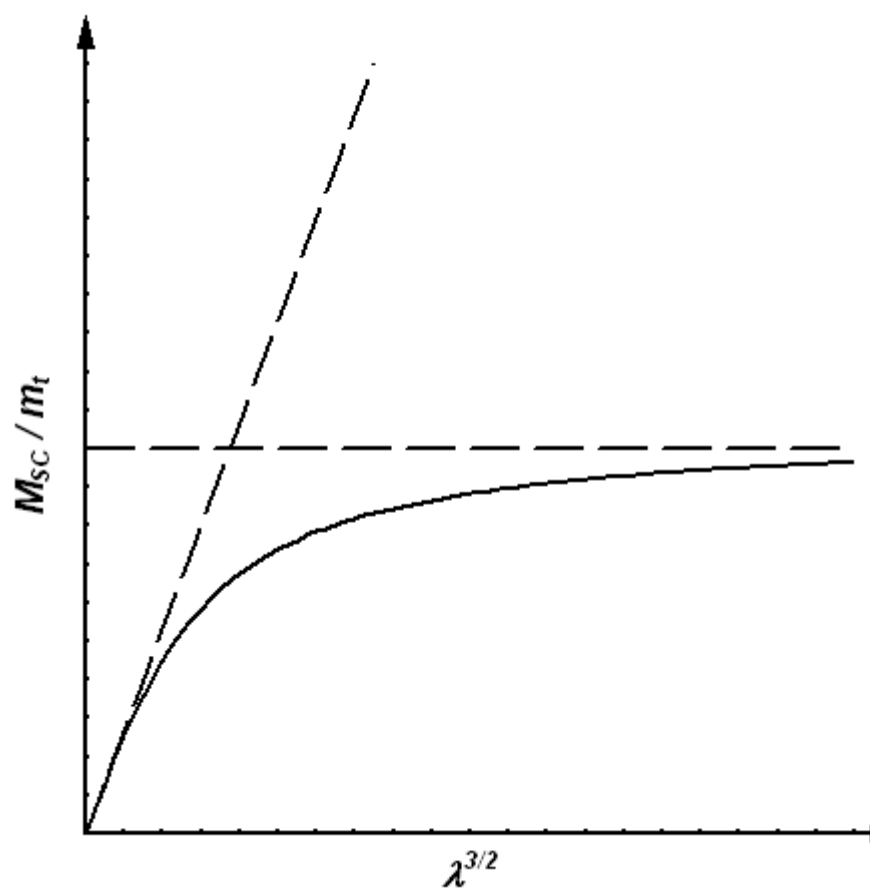


Figure 8. Sketch showing the mass-ratio dependence on parameter λ (for given values of β and perijove position). The dashed lines represent upper bounds as given by Eqs. (37a) and (45).

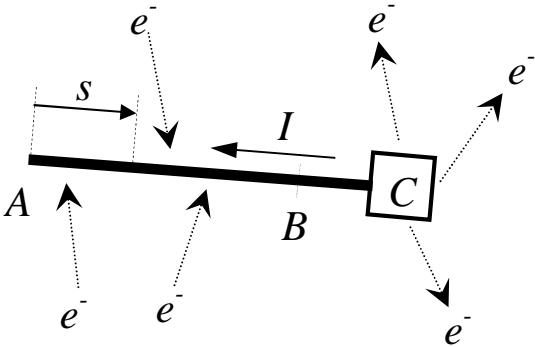


Figure 9. Sketch of bare-tether operation. Electrons are collected over an anodic

segment from end A to some point B. Bias is negative to the right of B; ion collection over the cathodic segment BC comes out to be negligible. Electrons are ejected at the hollow cathode at C. The hollow cathode at end A is off.

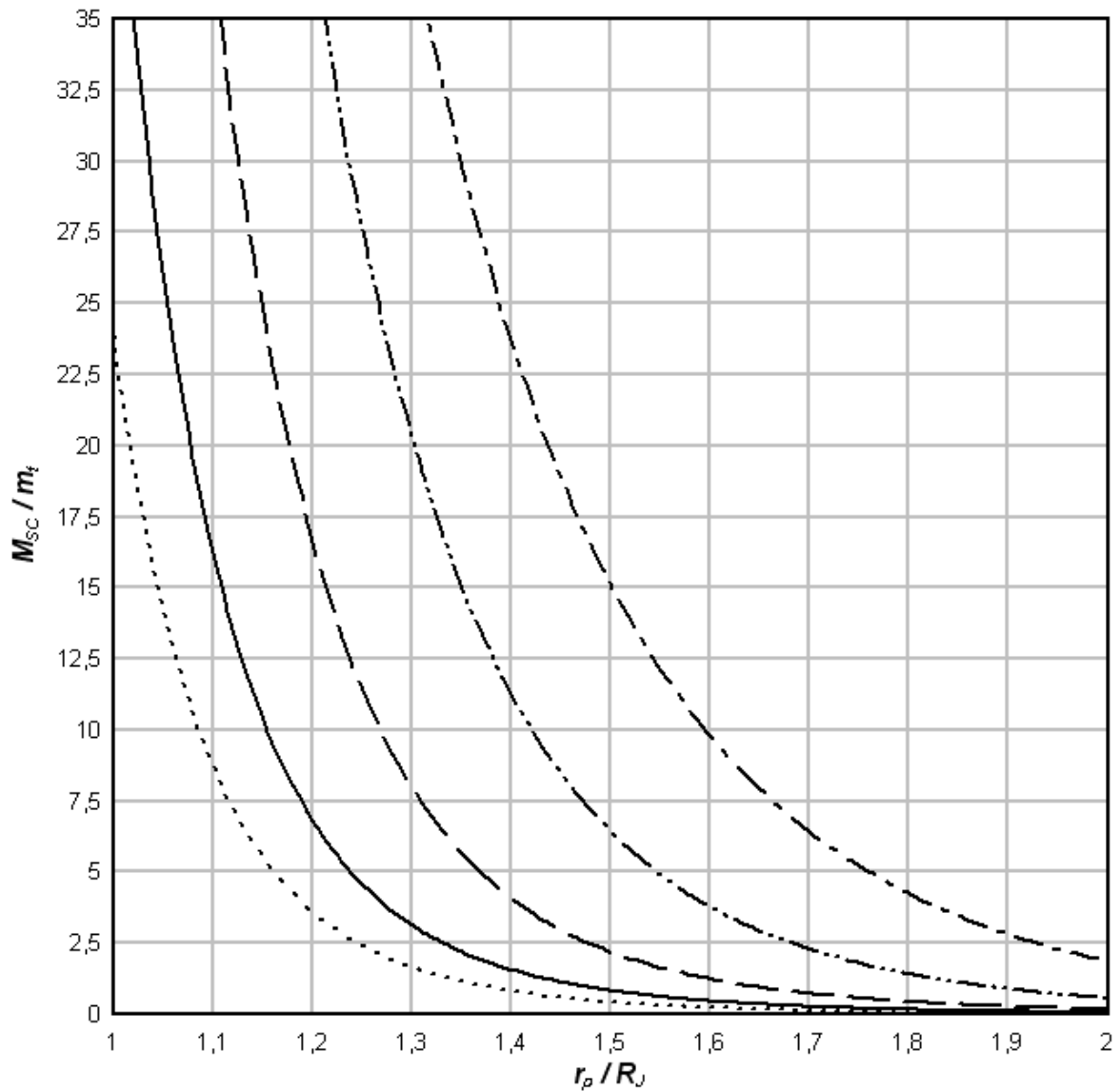


Figure 10. Mass ratio versus perijove position for $\beta = 1$ and several values of parameter λ in Eq.(45'). The mass ratio scales as $2 / (1 + \beta)$.

Dash-Dotted Line	Ohmic-dominated Limit	$\lambda \rightarrow \infty$
Dash-Double Dotted Line	L= 160km h = 0.05mm $f_N=2$	$\lambda \approx 5$
Dashed Line	L= 100km h = 0.05mm $f_N=1$	$\lambda = 2$
Full Line	L= 50km h = 0.05mm $f_N=1$	$\lambda = 1$
Dotted Line	L = 50km h = 0.1mm $f_N=1$	$\lambda \approx 0.63$
	L=80km h=0.1mm $f_N=1/2$	$\lambda \approx 0.63$

5 – Constraints on the capture operation

As seen in Fig.10 (with $\lambda \propto L/h^{2/3}$), the mass of the SC that a given tape-tether can capture is greater the longer and thinner is the tape and the closer to Jupiter gets the SC. As we shall now show, however, too powerful a capture, i.e. too high a ratio M_{SC}/m_t in Fig.10, may result in unacceptable tether temperature, and bowing or tensile stress, during capture. We will consider the hardest conditions, which occur at the perijove. We will take into account the rotation of the tether, but assume its position fixed at the perijove for simplicity in the discussion, making for slightly conservative estimates.

5.1 Local thermal balance

The energy equation determining the temperature $T(s)$ of an element of tether length δs in Fig. 9 is

$$wh\delta s \times \rho_t c_t \frac{\partial T}{\partial t} = \dot{w}_{th} \delta s - 2w\delta s \times \varepsilon_t \sigma_B T^4 + wh\delta s \times K_t \frac{\partial^2 T}{\partial s^2} \quad (60)$$

where c_t , ε_t and K_t are tether specific-heat, emissivity and thermal conductivity, respectively, and σ_B is the Stefan-Boltzmann constant. The last term above is entirely negligible compared with the first term, their ratio being of the order of $K_t/L^2\rho_t c_t \omega_t$; for aluminium we have

$$c_t \approx 0.90 \text{ J/gK}, \quad K_t \approx 2.11 \times 10^2 \text{ J/msK},$$

yielding a thermal diffusivity

$$K_t / \rho_t c_t \approx 8.7 \times 10^{-5} \text{ m}^2/\text{s},$$

whereas we have, for a tether spin period of 30 minutes and $L = 80 \text{ km}$ say,

$$L^2 \omega_t^2 \approx (80 \text{ km})^2 \times 0.0035 \text{ s}^{-1} \approx 2.24 \times 10^7 \text{ m}^2/\text{s}.$$

We will also ignore any small heating from the natural Jovian environment.

The heating power $\dot{w}_{th} \delta s$ is made of two contributions, one due to ohmic dissipation from the current $I(s)$ flowing through the element δs , and a second contribution due to the energy brought up to the element by the impact of collected electrons,

$$\dot{w}_{th} \delta s = \frac{I^2 \delta s}{\sigma_c wh} + \Delta V \times \frac{dI}{ds} \delta s, \quad (61)$$

where $I(s)$ and $\Delta V(s)$ are as determined by Eqs.(47) and (48). Integrating the first term above over the entire length of the tether readily yields

$$\frac{L}{\sigma_c wh} \times \int_0^L I^2 \frac{ds}{L} = R_t (I^2)_{av} \quad (62)$$

with R_t the full tether resistance, whereas the second term yields

$$\begin{aligned} \int_0^L \Delta V \frac{dI}{ds} ds &= I \Delta V \Big|_0^L - \int_0^L I \frac{d\Delta V}{ds} ds = - \int_0^L I \frac{d\Delta V}{ds} ds \\ &= - \int_0^L Ids \left(\frac{I}{\sigma_c wh} - E_m \right) = E_m LI_{av} - R_t (I^2)_{av}, \end{aligned} \quad (63)$$

where we used Eq.(48). The two terms do add up to the entire power from the Lorentz force, $E_m LI_{av}$, thus verifying that Eq.(61) fully accounts for the heating power.

5.2 Heating at perijove with dominant ohmic effects

For a simple illustration, we first consider the dominant ohmic-effects limit, which corresponds to taking $\lambda \rightarrow \infty$ in Fig.10; with actual low λ values, this will be a heavily conservative estimate, resulting in temperatures well above actual $\lambda \sim 1$ temperatures. We would then have $I = constant = \sigma_c E_m wh$ over the near entire length of the tether, collection only occurring over a very short tether segment near the anodic end, which we here ignore. The heating power is then reduced to the first term in Eq.(61),

$$\dot{w}_{th} \delta s \approx \sigma_c E_m^2 wh \delta s. \quad (61')$$

With $E_m = v' B \cos \varphi$, we use Eqs.(13a, b) and (34) for v' and Eq.(35) for B , at arbitrary \tilde{r} , to write

$$v' B = v_s B_s \times \frac{\tilde{r}_M^{4/3}}{2^{7/6} \tilde{r}^{7/2}} \times \sqrt{\tilde{r}_M^2 - 2\tilde{r}_M \tilde{r} + \tilde{r}^3}, \quad (64)$$

the energy equation at the perijove ($\tilde{r} = 1$) then reading

$$\frac{\partial T}{\partial t} = \frac{\sigma_c v_s^2 B_s^2}{c_t \rho_t} \times F_1 \left(\frac{r_p}{R_J} \right) \times \cos^2 \varphi - \frac{2\varepsilon_t \sigma_B}{c_t \rho_t h} T^4, \quad (65)$$

$$F_1 \equiv \left(\frac{\tilde{r}_M^{7/3} - \tilde{r}_M^{4/3}}{2^{7/6}} \right)^2, \quad (66)$$

with \tilde{r}_M given in Eq.(14). We now introduce the angle $\varphi = \omega t$ in Fig.4, and define

$$\hat{T} \equiv \frac{T}{T_\infty}, \quad T_\infty^4 \equiv \frac{h \sigma_c v_s^2 B_s^2}{2\varepsilon_t \sigma_B} \times F_1(\tilde{r}_M), \quad T_*^3 \equiv \frac{\rho_t c_t h \omega_t}{2\varepsilon_t \sigma_B}, \quad (67a, b, c)$$

Eq. (65) becoming

$$\frac{\partial \hat{T}}{\partial \varphi} = \left(\frac{T_\infty}{T_*} \right)^3 \times (\cos^2 \varphi - \hat{T}^4). \quad (68)$$

For $h = 0.05$ mm, 30 minutes spin, and emissivity as high as $\varepsilon_t = 0.8$, we have

$$T_\infty \approx 458.0 \times F_1^{1/4} \text{ K}, \quad T_* \approx 167.3 \text{ K}, \quad (69a, b)$$

giving a very large cubed ratio in Eq.(68),

$$(T_\infty / T_*)^3 \approx 20.5 \times [F_1(\tilde{r}_M)]^{3/4}, \quad (70)$$

where $F_1^{3/4}$ varies from 29.0 at $r_p = 1.1 R_J$ to 6.17 at $r_p = 1.4 R_J$. Note that the temperature T_∞ also varies from 1406.2 K at $r_p = 1.1 R_J$ to 839.5 K at $r_p = 1.4 R_J$. Clearly, the large values of $(T_\infty/T_*)^3$ in Eq.(98) will make the temperature follow quasi-steadily the

variation in angle φ . Maximum temperature would be $T \approx T_\infty$ at $|\cos\varphi|=1$, which is extremely high even for perijove at $1.4 R_J$.

5.3 Heating at perijove with no ohmic effects

The no ohmic-effects limit, best accommodating actual conditions, should just slightly overestimate temperature. We can now ignore the first term on the right-hand sides of both Eqs. (61) and (48), and readily solve for bias versus distance s ,

$$\Delta V(s) = E_m(L - s). \quad (71)$$

Equation (47) now directly gives the current collected by a tether length-element δs at distance s in Fig.9,

$$\delta I(s) = \frac{2w}{\pi} eN_e \sqrt{\frac{2e}{m_e} E_m(L - s)} \delta s. \quad (72)$$

The power reaching that element is then

$$\dot{w}_{th}(s)\delta s = \Delta V \times \delta I = eN_e \frac{2w}{\pi} \sqrt{\frac{2eE_m L}{m_e}} E_m L \times \left(1 - \frac{s}{L}\right)^{3/2} \delta s. \quad (61'')$$

Using $E_m = v'B \cos\varphi$ and Eq.(64), and using Eq.(36) for the plasma density, the energy equation reads

$$\frac{\partial T}{\partial t} = \frac{2}{\pi} \frac{N_s}{hc_t \rho_t} \frac{ev_s B_s L}{m_e} \sqrt{\frac{2ev_s B_s L}{m_e}} \times F_2 F_1^{3/4} \times \left(1 - \frac{s}{L}\right)^{3/2} \cos^{3/2} \varphi - \frac{2\varepsilon_i \sigma_B}{hc_t \rho_t} T^4, \quad (73)$$

where we have

$$F_2(\tilde{r}_M) \equiv f_N \times \exp(2.72\tilde{r}_M^{2/3} - 3.43) \quad (74)$$

Defining

$$\bar{T} \equiv \frac{T}{T_0}, \quad \frac{N_s}{2\varepsilon_i \pi \sigma_B} \frac{ev_s B_s L}{m_e} \sqrt{\frac{ev_s B_s L}{m_e}} F_2(\tilde{r}_M) [F_1(\tilde{r}_M)]^{3/4} \equiv T_0^4, \quad (75a, b)$$

Eq.(73) becomes

$$\frac{\partial \bar{T}}{\partial \varphi} = \left(\frac{T_0}{T_*} \right)^3 \left[\left(2 \frac{L-s}{L} \right)^{3/2} |\cos \varphi|^{3/2} - \bar{T}^4 \right]. \quad (76)$$

with T_* as given in Eq.(67c).

For $\varepsilon_i = 0.8$ and $L = 80$ km we have

$$T_0 \approx 194.3 \times F_2^{1/4} F_1^{3/16} K, \quad (77)$$

ranging from 1092 K at $r_p = 1.1 R_J$ to 511 K at $r_p = 1.4 R_J$, when taking $f_N = 1$. We then find a ratio

$$T_0^3 / T_*^3 = 1.57 \times F_2^{3/4} F_1^{9/16}, \quad (78)$$

ranging from 278.1 at $r_p = 1.1 R_J$ to 28.5 at $r_p = 1.4 R_J$, still suggesting a quasi-steady temperature evolution with angle φ .

Note that the energy law is here dependent on the tether point considered. There are two simple limiting cases, corresponding to values $s = L/2$ and $s = 0$ (L), respectively. In the first case, the $L/2$ value clearly holds throughout the entire $-\pi/2 < \varphi < 3\pi/2$ range, Eq.(76) reading

$$\frac{\partial \bar{T}}{\partial \varphi} = \left(\frac{T_0}{T_*} \right)^3 \left[|\cos \varphi|^{3/2} - \bar{T}^4 \right], \quad -\pi/2 < \varphi < 3\pi/2. \quad (79)$$

In the second case, a value $s = 0$ for $-\pi/2 < \varphi < \pi/2$ corresponds to a value $s = L$ for $\pi/2 < \varphi < 3\pi/2$, the energy equation then reading

$$\frac{\partial \bar{T}}{\partial \varphi} = \left(\frac{T_0}{T_*} \right)^3 \left[2^{3/2} \cos \varphi^{3/2} - \bar{T}^4 \right], \quad -\pi/2 < \varphi < \pi/2 \quad (80a)$$

$$\frac{\partial \bar{T}}{\partial \varphi} = - \left(\frac{T_0}{T_*} \right)^3 \times \bar{T}^4, \quad \pi/2 < \varphi < 3\pi/2. \quad (80b)$$

If the temperature still follows quasisteadily the changing angle in both Eqs. (79) and (80), its absolute maximum will occur at the tether ends, with $\bar{T} = 2^{3/8}$. Figure 11 shows

T/T_0 versus φ from Eqs.(80a, b) for $r_p = 1.4 R_J$, with $T_0^3 / T_*^3 = 28.5$. Maximum temperatures would then be

$$T_{max} = T_0 = 511 \text{ K}, \quad (81a)$$

$$T_{max} = 2^{3/8} \times T_0 = 662 \text{ K} \Rightarrow 389 \text{ }^\circ\text{C}, \quad (81b)$$

at tether midpoint and end point(s), respectively.

To reduce the absolute maximum at the tether ends, notice that inverse rise-time and temperature T_0 scale as

$$\left(\frac{T_0}{T_*} \right)^3 \propto \frac{\varepsilon_t^{1/4} L^{9/8}}{\rho_t c_t h \omega_t} \times (F_2 F_1^{3/4})^{3/4}, \quad (82)$$

$$T_0 \propto \frac{L^{3/8}}{\varepsilon_t^{1/4}} \times (F_2 F_1^{3/4})^{1/4}. \quad (83)$$

Both T_0 and inverse rise-time can be reduced by reducing the tether length. Moving from 80 km to 50 km, the rise time would still be short,

$$(T_0 / T_*)^3 \approx 16.8 \quad (L = 50 \text{ km}, \quad r_p = 1.4 R_J), \quad (84)$$

but the maximum possible temperature would be substantially reduced,

$$(50/80)^{3/8} \times 2^{3/8} \times 511 \text{ K} \Rightarrow 282 \text{ }^\circ\text{C} \quad (L = 50 \text{ km}, \quad r_p = 1.4 R_J). \quad (85)$$

Alternatively, one could place the perijove a little farther from Jupiter. At $r_p = 1.5 R_J$ with L back to 80 km, we would have

$$(T_0 / T_*)^3 \approx 15.4 \quad (L = 80 \text{ km}, \quad r_p = 1.5 R_J), \quad (86)$$

$$T_{max} \approx 266 \text{ }^\circ\text{C} \quad (L = 80 \text{ km}, \quad r_p = 1.5 R_J). \quad (87)$$

The rise time could be further increased by using a faster spin; moving from 30 to 20 minutes spin period, with $L = 80 \text{ km}$, $r_p = 1.5 R_J$, yields $(T_0 / T_*)^3 \approx 10.3$, temperature now barely reaching the possible $2^{3/8} T_0$ maximum. Notice, however, that placing the perijove farther

from Jupiter or reducing the tether length (thus reducing the parameter λ in Fig.10 too), makes SC capture harder.

5.4 – Tether tension under spinning

In the simplest, ideal situation, the gravity gradient force can keep a tether taut in circular orbit around a planet. The standard formula for the gravity-gradient tension T_f on a tether kept straight along the local vertical while orbiting under negligible lateral force is

$$T_f = \frac{3\omega^2 LM_{SC}}{4}, \quad (88)$$

where a massless tether with equal masses $M_{SC}/2$ at either end was considered. Two thirds of the tension above arise from the fact that gravitational forces decrease as the inverse square of distance from the planet center. Taking into account tether mass, with equal end masses $(M_{SC} - m_t)/2$, yields a small correction that makes the tension vary with distance $s' \equiv (L/2) - s$ from mid-tether (Fig.9),

$$\begin{aligned} T_f &= \frac{3\omega^2 LM_{SC}}{4} \times \left[1 - \frac{m_t}{2M_{SC}} \times \left\langle 1 + \left(\frac{s'}{L/2} \right)^2 \right\rangle \right] \\ &\approx \frac{3\omega^2 LM_{SC}}{4} \times \left[1 - \frac{2m_t}{3M_{SC}} \right]; \end{aligned} \quad (89)$$

we finally averaged T_f over the tether length for use in simple estimates to follow.

Conditions in the Jovian mission are far from ideal, however. First, Kepler's law

$$\omega^2 = \mu/a^3 \propto \rho R^3/a^3, \quad (90)$$

shows that, with the density of Jupiter being one fourth the Earth's density, and other factors being equal, tether tension for a grazing ($a \approx R$) Jovian orbit is one fourth the tension in standard (roughly grazing) Low Earth Orbits. Further, tether orbits along the Jovian mission are far from grazing; this makes the gravity gradient much weaker. Orbits are also far from

circular. Finally, the lateral Lorentz force may be here extremely large at capture and result in substantial bowing.

Spinning with $\omega_t^2 \gg 3\omega^2$ can provide the tension required to keep lateral deflection small. Neglecting the gravity-gradient contribution as given in Eq.(89), the tension under tether spin is obtained from Eq.(89) itself through the simple replacement $3\omega^2 \Rightarrow \omega_t^2$,

$$T_f \approx \frac{\omega_t^2 L^2 \rho_t h w}{4} \times \left[\frac{M_{sc}}{m_t} - \frac{2}{3} \right]. \quad (91)$$

As regards the Lorentz force f_L , Eqs.(23) and (24) give, in the no ohmic effects limit,

$$f_L = LB \times \frac{4wL}{5\pi} eN_e \sqrt{\frac{2eL}{m_e} v' B \cos \varphi}. \quad (92)$$

Using Eq.(64) for $v'B$ and setting $\tilde{r} = 1$, and $\cos \varphi = 1$ in order to consider the case of maximum force and deflections, we find

$$\begin{aligned} f_L &= \frac{4wL}{5\pi} LN_s e B_s \times \sqrt{\frac{2eLv_s B_s}{m_e}} \times \frac{\tilde{r}_M^2}{2} F_2(\tilde{r}_M) [F_1(\tilde{r}_M)]^{1/4} \\ &\approx \frac{w}{3 \text{ cm}} \left(\frac{L}{80 \text{ km}} \right)^{5/2} \times \frac{\tilde{r}_M^2}{2} F_2 F_1^{1/4} \times 88 \text{ N} \end{aligned} \quad (93)$$

where F_1 and F_2 are given in Eqs.(66) and (74).

5.5 Maximum tether bowing at capture

For a simple, conservative estimate of bowing, consider the classical equation of statics for a rope loaded laterally and supported at the two ends (Fig. 12),

$$\frac{d^2 y}{dx^2} = \frac{q}{T_f}, \quad (94)$$

where y is the lateral deflection of the rope. Here, the distributed lateral load $q(x)$ is the Lorentz force per unit tether length,

$$q(x) \equiv \delta f_L / \delta x = BI(x), \quad (95)$$

and x is measured from (say) the anodic end. We are assuming the tension large enough to keep deflections small.

In the ohmic-dominated limit we would have $I = \text{const} = \sigma_c E_m w h$ over near the entire tether length. Integrating Eq.(127) twice with boundary conditions $y(0) = y(L) = 0$, yields the classical result for uniform load distribution, with maximum deflection (at mid-point, $x = L/2$)

$$\frac{|y|_{\max}}{L} = \frac{f_L}{8T_f}. \quad (96)$$

In the opposite limit, reasonably appropriate to the Jovian case, Eq.(47), and Eq.(48) with the first term dropped, readily yield

$$\frac{I(x)}{I_{\max}} = 1 - \left(1 - \frac{x}{L}\right)^{3/2} \quad (97)$$

with $3I_{\max} = 5I_{av}$, and I_{av} as given in Eq.(3). We then have for $q(x)$ in Eq.(95),

$$q(x) = \frac{3f_L}{5L} \left[1 - \left(1 - \frac{x}{L}\right)^{3/2} \right]. \quad (98)$$

A straightforward integration yields a maximum deflection (at $x \approx 0.564 L$)

$$\frac{|y|_{\max}}{L} = \frac{f_L}{7.6 T_f}. \quad (99)$$

Requiring this percent deflection not to exceed some small value, say, 0.1, sets a condition,

$$T_f / f_L > 1.31, \quad (100)$$

roughly. For $L = 80$ km, $r_p = 1.5 R_J$, and $w = 3$ cm say, we find $f_L = 250$ N. Taking $M_{SC} = 3m_t$ with a 30 minutes spin (and aluminium tape thickness $h = 0.05$ mm) we find too weak a corresponding tension $T_f = 185$ N. Note that the tension-to-force ratio scales as

$$\frac{T_f}{f_L} \propto \frac{(r_p/R_J)^3 \times \rho_t h \omega_t^2}{F_2(r_p/R_J) [F_1(r_p/R_J)]^{1/4} \times \sqrt{L}} \times \left(\frac{M_{SC}}{m_t} - \frac{2}{3} \right), \quad (101)$$

independently of width w . Just taking a faster spin of $30 / \sqrt{2} \approx 21$ minutes period, say, yields a ratio satisfying the condition (100),

$$T_f/f_L \approx 1.48 > 1.31. \quad (102)$$

5.6 – Tensile stress under spinning

Too high a spin, however, may result on unacceptable tensile stress, which, under spinning, is given as

$$\begin{aligned} \frac{T_f}{wh} &= \frac{\omega_t^2 L M_{SC}}{4wh} \times \left(1 - \frac{2m_t}{3M_{SC}} \right) \\ &= \left(\frac{M_{SC}}{m_t} - \frac{2}{3} \right) \times \frac{\rho_t \omega_t^2 L^2}{4}. \end{aligned} \quad (103)$$

For $M_{SC} = 3 m_t$, and an aluminium, 80 km long tether, at 21 minutes spin, Eq.(103) yields

$$\frac{T_f}{wh} = 2.64 \times 10^8 \frac{N}{m^2}. \quad (104)$$

The tensile strength of some aluminium alloys may be over twice as high. Alloys would have somewhat lower electrical conductivity than pure aluminium but, as noticed at the end of Ch.4., one might still be in the no ohmic effects limit, which is independent of conductivity. An alternative would be to have a thin slice of sandwiched Kevlar, which has a tensile strength as high as 30×10^8 N/m². Kevlar would also reinforce the aluminium tape against tearing.

5.7 Brief conclusions

At this point we can summarize some preliminary conclusions:

- Tether temperature will be in local quasisteady equilibrium, heat and radiated power keeping nearly equal at each point as the tether rotates.
- In the no-ohmic effects limit best representing conditions at the Jovian mission, heating arises from the impact of collected electrons, and maximum temperatures occur at tether ends, even though they only receive heating when acting anodically, i.e. half the time.
- To keep acceptable tether temperatures around perijove, at capture, an aluminum tape will require coating to reach emissivity as high as $\varepsilon_t = 0.8$.
- Too powerful capture leads to unacceptable temperatures at the perijove. For an 80 km, 0.05 mm tape, temperatures will be acceptable, if $r_p \geq 1.5 R_J$ (for a 50 km tape, r_p / R_J could be as low as 1.4).
- Low gravity gradients and high lateral Lorentz forces at Jupiter make tether spin necessary.
- For an 80 km, 0.05 mm tape, with 1/3 the full SC mass and capture perijove at $r_p = 1.5 R_J$, a spin period of about 20 minutes is required to keep bowing below 10 per cent of tape length.
- Tensile stress then keeps below the tensile strength of characteristic aluminium alloys.
- Capture in Eqs. (43') and Fig. 10 under thermal and bowing/tensile-stress constraints is made easier by allowing a low β in Eq. (1) [leading to a first orbit of extreme eccentricity]; lowering the excess hyperbolic velocity v_∞ ; reducing tape thickness h and density ρ_t (by using Kevlar on part of the cross section).

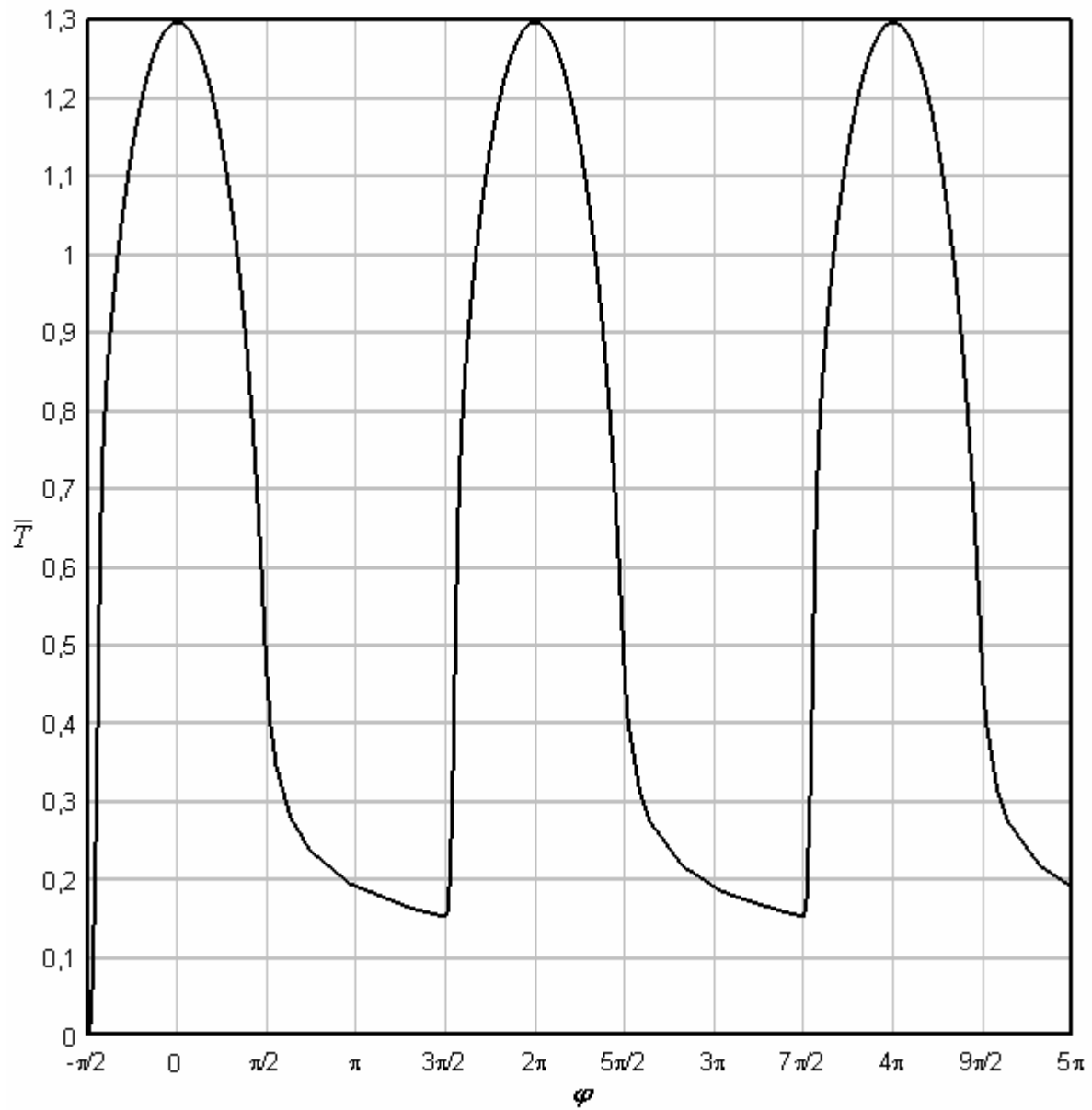


Figure 11. Temperature ratio T/T_0 at the tether end that is anodic when $\cos\varphi$ is positive in Fig.4, versus angle φ ; T_0 defined in Eq. (75b), $T = 0$ at $\varphi = -\pi/2$.

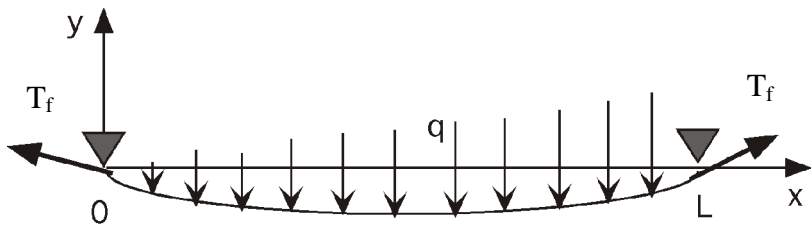


Fig. 12. Schematics of tether under lateral load and tension T_f .

6 – Tether deployment, (rotational) dynamics, and power budget

Making the tether spin will require using rocket propellant. Consider equal thrust applied by rockets at both tether ends, with tether current still off. Neglecting the weak gravity gradient, the equation for the rotational motion of the tether would be

$$I_{CM} \frac{d\omega_t}{dt} = \frac{\dot{m}_{prop}}{2} v_{exh} \times L, \quad (105)$$

where v_{exh} is the rocket exhaust velocity, \dot{m}_{prop} is the joint propellant mass flow rate at the two tether ends, and I_{CM} is the moment of inertia of the SC with respect to the center of the tether, as discussed below,

$$I_{CM} = \frac{L^2 M_{SC}}{4} \times \left(1 - \frac{2m_t}{3M_{SC}}\right). \quad (106)$$

Integrating Eq.(105) from an initial zero spin to the desired final value, determines the propellant mass consumed as proportional to the final spin,

$$m_{prop} = \frac{2I_{CM} \omega_t}{v_{exh} L} = M_{prop} \times \frac{\omega_t L}{2v_{exh}} \times \left(1 - \frac{2m_t}{3M_{SC}}\right). \quad (107)$$

For $L = 80$ km, $v_{exh} \approx 3$ km/s, a 21 minutes spin, and $m_t = M_{SC}/3$, Eq.(107) yields

$$m_{prop} \approx 0.05 M_{SC}. \quad (108)$$

Additional propellant mass would be consumed in orbit fine-tuning while in the cruise phase. Note, however, that none such propellant makes part of the mass that need be captured into a Jovian orbit, because it would be consumed well before capture proceeds. Only propellant mass possibly consumed in moon tour operations if at all, and some small fraction of total propellant mass for plumbing, which may be as low as 0.1, need be accounted for in M_{SC} .

This suggests rocket thrust may be also used to help deployment, with no mass penalty on the capture and orbit tour operations.

6.1 – Tether deployment

Deployment of tethered systems is carried out by utilizing passive (non-motorized) or active (motorized) deployers. If tether retrieval or length control is not an issue, a passive deployer is normally well suited for deploying the tether and keeping its length stationary and, when properly designed, is much lighter and simpler than an active deployer. Deployers either active or passive have been developed for handling cylindrical and tape tethers. Examples of the former type are the TSS, SEDS and PMG deployers while an example of the latter type is the Atex deployer. The SEDS deployer has also been tested successfully on (thin) tape tethers with a width of few millimeters.

The most common type of deployers uses a drum to reel out (and in if necessary) the tether which is spooled on it. If the tether needs only to be deployed, no leveling mechanism is required to distribute the tether evenly along the axis of the drum, to complement the reeling system. Other deployers use a stationary spool whereby the tether unravels from the spool by pulling it out along the spool axis. This type of deployer (e.g., the SEDS deployer) can not reel in the tether but is very simple and light. Moreover, in a stationary spool the only moving mass is the exiting portion of the tether mass and, consequently, the tether can receive sudden accelerations without incurring very high values of tension. This consideration implies that a spring ejection system that imparts a strong initial acceleration is not suitable to be used with a reeling deployer but it is for a stationary-spool deployer.

Actual tether deployments (i.e., in flight missions) have thus far taken place in Low Earth Orbit (LEO) following the librating-deployment strategy. In librating deployment the

system does not spin but rather it librates about its local-vertical stable position determined by the gravity gradient. The librating strategy was primarily dictated by the fact that the tether had to terminate deployment aligned with the local vertical, that is, stationary with respect to the orbital reference frame. For a system that has to be spinning with respect to that frame at the end of deployment, it is more convenient to use a spinning deployment.

A gravity gradient is not required for such type of deployment and, consequently, it can take place in deep space or more generally in conditions of weak gravity gradient. The centrifugal forces generated by the spin produce a tether tension that facilitates the extraction of the tether from the deployer. Spinning deployment can be faster than librating deployment because there are no limits imposed on the tether exit velocity by the maximum (stable) amplitude of the libration. Spinning deployment has not been experimented in space yet but it has been studied by several authors and its realization is expected to be quite straight forward (M.L.Cosmo, E.C.Lorenzini and C.Bombardelli, *Space Tethers as Testbeds...*, 14th AAS/AIAA Space Flight Mech.Conf., Paper 04-171 /2 004).

In a spinning deployment, the two end masses are separated initially at a relatively low speed; the system is then put into a spin by lateral thrusters placed on the end masses, and deployment proceeds with the help of centrifugal forces while the tether tension is controlled by a breaking mechanism that lets the tether out.

An existing deployer that is closest to the specifications of a tape tether for a Jupiter mission is the deployer of Atex, which was designed to deploy a 1-inch wide (non-conductive) tape by using a passive reel with motorized pinch rollers to pay the tether out. A reeling system seems preferable for deploying wide tapes than a stationary spool because the wide tape could be twisted while exiting along the axis of the stationary spool and likely to produce high friction or even to cause jamming. Unlike the flat-metal-pushing ejection

system adopted by ATeX for the initial separation of the end mass, we envision an in-line (along the tether) thruster, like in TSS, to provide the separation force during the early stage of deployment for the Jupiter mission. Since the spin rate would decrease as deployed length increases, in-line thrust should be kept until some particular tether length is deployed.

6.2 Tether rotational motion during capture

Equal mass points at the tether ends make for a gravity-gradient torque at its center O (Fig.13)

$$\frac{L}{2} \bar{u} \wedge \left(-m \frac{\mu_J \bar{r}_A}{r_A^3} + m \frac{\mu_J \bar{r}_C}{r_C^3} \right), \quad (2m = M_{SC} - m_t).$$

Similarly, considering (symmetric) mass elements $m_t ds' / L$ (a and c) at distance s' from the center of the tether, on both sides, the tether contribution to that torque is

$$\int_0^{L/2} s' \bar{u} \wedge \left(-\frac{m_t ds'}{L} \frac{\mu_J \bar{r}_a}{r_a^3} + \frac{m_t ds'}{L} \frac{\mu_J \bar{r}_c}{r_c^3} \right).$$

Using $\bar{r}_A = \bar{r}_C + L \bar{u}$, $\bar{r}_a = \bar{r}_c + 2s' \bar{u}$ with $2s' < L \ll r$, the total gravity-gradient torque, to order $(L/r)^2$, becomes

$$\left[\frac{L^2}{4} (M_{SC} - \frac{2}{3} m_t) \right] \times \frac{-3\mu_J}{2r^3} \sin\{2(\alpha + \varphi)\}. \quad (109)$$

The factor in the bracket above is the moment of inertia I_{CM} with respect to the center of mass, as noticed.

Next, the electrodynamic torque is (Fig.13)

$$-(s_F - \frac{1}{2} L) \bar{u} \wedge (i_{av} \sigma_c wh E_m LB \bar{k} \wedge \bar{u})$$

where $\xi_F \equiv s_F / L^*$ can be readily obtained from Sec.4.5 : we have

$$\xi_F(\hat{L}) = \frac{\int_0^{\hat{L}} \xi i d\xi}{\int_0^{\hat{L}} i d\xi} < 1/2, \quad (110)$$

with denominator taken from Eq.(54), and numerator given as

$$\int_0^{\hat{L}} \xi i d\xi = \frac{\hat{L}^2}{2} + \int_{\psi_A}^0 \xi d\psi = \frac{\hat{L}^2}{2} - \int_0^{\psi_A} \frac{\psi d\psi}{\sqrt{1-\psi_A^{3/2} + \psi^{3/2}}}, \quad (111)$$

where we used Eqs.(52) and (48'), and where $\psi_A(\hat{L})$ is taken from Eqs.(57a, b).

The equation for the rotational motion is then

$$\frac{d\omega_t}{dt} = -\frac{3\mu_J}{2r^3} \times \sin[2(\alpha+\varphi)] - \left(\frac{\xi_F}{\hat{L}} - \frac{1}{2} \right) \times \frac{4i_{av}\sigma_c whB^2 v'}{M_{SC} - 2m_t/3} \times \cos\varphi. \quad (112)$$

In the absence of Lorentz torque, Eq.(112) with ω_t as shown in Eq.(21) of Sec. 4.1, would be the usual description of oscillations in the angle $(\alpha + \varphi)$ between tether and local vertical, as driven by motion on a noncircular-orbit. The Lorentz torque makes a significant change by introducing the angle φ separately in Eq. (112). Further, a fast spin as assumed in Sec. 4.1 allows angle-averaging this equation to obtain a very simple result, the gravity-gradient torque averaging to zero,

$$\left\langle \frac{d\omega_t}{dt} \right\rangle \approx -\frac{4\sigma_c whB^2 v'}{M_{SC} - 2m_t/3} \left\langle \cos\varphi \times i_{av}(\hat{L}) \times \left(\frac{\xi_F(\hat{L})}{\hat{L}} - \frac{1}{2} \right) \right\rangle, \quad (113)$$

with ξ_F given by Eqs. (54), (110), and (111). Next, integrating over the time on the drag arc, as carried out for Eqs. (28) and (41), we find

$$\int \left\langle \frac{d\omega_t}{dt} \right\rangle dt = \langle \Delta\omega_t \rangle = -\omega_* \times \frac{m_t}{M_{SC} - 2m_t/3} \times \Delta(\lambda, \tilde{r}_M) \quad (114)$$

$$\omega_* \equiv \frac{2^{1/3} \sigma_c a_s B_s^2}{\rho_t L} \approx \frac{50 km}{L} \times 0.0754 s^{-1}, \quad (115)$$

$$\Delta \left[\lambda, \frac{r_p}{R_J} \right] \equiv 2 \tilde{r}_M^{7/3} \int_1^{\tilde{r}_M} \frac{d\tilde{r} \sqrt{\tilde{r}_M^2 - 2\tilde{r}_M \tilde{r} + \tilde{r}^3}}{\tilde{r}^{11/2} \sqrt{\tilde{r} - 1}} \langle \cos \varphi \times i_{av} \times \left(\frac{\xi_F}{\hat{L}} - \frac{1}{2} \right) \rangle. \quad (116)$$

Equations (44') and (116) may appear similar but they are actually quite different. Figure 14 shows Δ versus λ at several values of r_p/R_J . Whereas S increases monotonically with λ at fixed r_p/R_J , Δ first increases, then decreases with λ ; also Δ is typically an order of magnitude smaller. Both facts are due to an essential difference between factors i_{av} in Eq.(44') and $i_{av} \times \left[(\xi_F / \hat{L}) - 1/2 \right]$ in Eq. (116); the first increases monotonically with \hat{L} , the second one vanishes both as $\hat{L} \rightarrow 0$ (with $i_{av} \rightarrow 0$) and $\hat{L} \rightarrow \infty$ (with $s_F \rightarrow L/2$), as shown in Fig. 15.

The moderate values of Δ then result in moderate values of $\langle \Delta \omega_t \rangle$. For a tether with $L = 80$ km, $h = 0.05$ mm and a $f_N = 1$ plasma density profile ($\lambda = 1.6$), a mass ratio $M_{SC}/m_t = 3$, and perijove at $1.5 R_J$, Fig. 14 and Eq. (115) yield $\Delta \approx 1/3$ and $\omega_* \approx 0.047$ s⁻¹, Eq.(114) finally giving $\langle \Delta \omega_t \rangle \approx -0.0067$ s⁻¹. Note the negative sign here. This sign is a general result, the Lorentz torque on a bare tether with cathodic device *on*, and just OML-collection impedance and tether resistance, being always parallel to the magnetic field, which, at the equator, is itself antiparallel to the planetary spin in the case of Jupiter. Consider the above tether entering the drag arc with an initial spin rate $\omega_{t0} = -0.0053$ s⁻¹ (about 20 minutes period). The full variation in tether spin over the drag arc would then amount to about doubling the spin rate during capture, possibly having no sensible effect on tether dynamics. In case ω_t was initially positive, however, it could be greatly reduced in magnitude by the Lorentz torque, dangerously affecting tether dynamics. Thus, an important consequence of that negative sign is that the tether should enter the drag arc of the orbit with spin antiparallel

to the Jupiter spin; actually, the Lorentz torque itself might be used to help make the spin, if low at deployment, reach a required value.

The factor $(\tilde{r}_M - \tilde{r})$ inside the integrals in Eqs.(33), (44) and (44'), for Σ , S_∞ and S respectively, changed sign as one moved beyond r_M , marking the transition from drag to thrust. No sign change appears in Eq.(116), however, the Lorentz torque keeping antiparallel to the Jupiter spin beyond r_M ; i.e., with the hollow cathode on and just OML-collection impedance and tether resistance, the Lorentz torque is parallel to the magnetic field \mathbf{B} *whatever* the direction of the Lorentz force. Note, however, that if one switches off the cathodic devices, making the bare tether to electrically float (current vanishing at both ends), the torque switches direction, current then being maximum very near the anodic end: the anodic segment is a fraction of tether length equal to the cubic root of the electron-to-ion mass ratio. The average tether current, now dominated by ion OML collection, drops by more than two orders of magnitude from the corresponding value with the cathodic device *on* (M.Martinez-Sanchez and J.R,Sanmartin, J. Geophys. Res. **102**, 27257 / 1997 /; A.van Dijk *et al.*, *LeBRETON, A Lightweight...*, IAC-03-S.P.05 Paper / 2003).

6.3 - Power budget

During capture, a very large amount of energy is taken from the orbital motion of the SC into the tether electrical circuit, and transformed ultimately into thermal energy of the tether, which it radiates away as discussed in Ch.5. From Eq.(2) one could have

$$|W_C| \sim 0.75 M_{SC} v_\infty^2 \approx 6 \text{ MWh} \quad (117)$$

where we set $\beta \sim 0.5$, $v_\infty \sim 5.6 \text{ km/s}$, and $M_{SC} = 972 \text{ kg}$, corresponding to $w = 3 \text{ cm}$, $L = 80 \text{ km}$, $h = 0.05 \text{ mm}$ ($m_t = 324 \text{ kg}$) and $M_{SC}/m_t \approx 3$. Clearly, a small fraction of that energy could be derived to electric loads at the tether ends, with negligible effect on tether current and thus on the dynamics of capture. A small part of that energy could be used during

capture, but a much greater part, E_{st} , might be saved/stored in batteries or regenerative fuel cells, for later use (for instance, for powering electrical propulsion, if required).

The saved energy is basically limited by the mass of the storing device. Storing a 0.5 per cent energy fraction, or $E_{st} \sim 30$ kWh, could provide 250 W power during 120 hours. For secondary batteries with specific density about 200 Wh/kg, or 5 kg/kWh, the required mass would be about 150 kg, which is of course too high. Actually, the cycle life of the batteries would be low, less than 100 cycles, possibly allowing use of primary-type batteries, with specific energy as high as 500 Wh/kg, for a mass of 60 kg. In case of a regenerative fuel-cell, both cell and fuel (hydrogen *plus* required oxygen) masses contribute to system mass. The ideal specific power of the fuel is about 4.3 kWh/kg but the masses of storage tanks and inefficiencies (C.P.Garcia *et al.*, *Round Trip Energy Efficiency of NASA Glenn Regenerative Fuel Cell System*, NASA/TM 2006-214054) would make 2 kWh/kg a more realistic figure, yielding a fuel related mass of 15 kg. With a cell specific power of order 100 W/kg, the overall storage mass would be under 20 kg. Fuel storage could be a main issue.

Actually, power of the order of 250 W could be locally generated over a substantial fraction of the orbit following capture, and over following orbits in the tour to be discussed in Ch.7, saving fuel-cell power for the regions outside the denser parts of plasmasphere and torus. Away from those regions, one could keep (hollow cathodes and) current on, using the tether in a generator mode, which requires the impedance of some electrical load be comparable to the impedance of OML current-collection. Although the power taken from the SC motion will be very small (when compared with the power produced during high-current operations, thus having negligible effect on orbit dynamics), the load would take a fraction (the generator efficiency) of order unity of such power. An efficiency about 0.5 can be obtained in an optimal generator tether, which must have a large segment insulated (J.R.Sanmartin and E. Lorenzini, *Spherical Collectors versus Bare Tethers for Drag, Thrust*

and Power Generation, IEEE Trans. Plasma Sci. / Oct. 2006 issue). With our Jovian tether fully bare as required for propulsion, efficiency may just reach 1/3.

Consider the angle-averaged mechanical (Lorentz) power discussed in Ch.4. In the simple no ohmic-effects approximation, Eq.(29) may be used to write

$$\frac{|\langle \dot{W} \rangle|}{m_t} = \frac{4\sqrt{2} \times 0.556}{5\pi} \times \frac{wL^2 eN_e B}{\rho_t hwL} \times \sqrt{\frac{eBL}{m_e}} \times \frac{vv'_t}{\sqrt{v'}}. \quad (118)$$

Using $B = B_s \times (a_s / r)^3$ and Eqs.(13a, b) and (34) for v' and v , Eq.(118) can be rewritten as

$$\begin{aligned} \frac{|\langle \dot{W} \rangle|}{m_t} &= \frac{0.2N_s}{\rho_t h} \times ev_s B_s L \times \sqrt{\frac{ev_s B_s L}{m_e}} \times \left(\frac{a_s}{r}\right)^{9/2} \frac{N_e}{N_s} \times \\ &\times \frac{|\tilde{r}_M - \tilde{r}|}{2^{1/4} \tilde{r}^{3/4} \sqrt[4]{\tilde{r}_M^2 - 2\tilde{r}_M \tilde{r} + \tilde{r}^3}} \end{aligned} \quad (119)$$

or finally

$$\frac{|\langle \dot{W} \rangle|}{m_t} = 0.179 \times \frac{0.05 \text{ mm}}{h} \times \left(\frac{L}{80 \text{ km}}\right)^{3/2} \frac{\text{kW}}{\text{kg}} \times \frac{\tilde{r}_M^3}{\tilde{r}^{21/4}} \times \frac{|\tilde{r}_M - \tilde{r}|}{(\tilde{r}_M^2 - 2\tilde{r}_M \tilde{r} + \tilde{r}^3)^{1/4}} \times \frac{N_e}{N_s}. \quad (119')$$

Note the $L^{3/2} / h\rho_t$ scaling.

Within the plasmasphere ($r < 3.8 R_J$), N_e / N_s is given by Eq.(36), written as

$$\frac{N_e}{N_s} = f_N \times \exp\left[2.72 \times \frac{\tilde{r}_M^{2/3}}{\tilde{r}} - 3.43\right]. \quad (120)$$

where we will set $f_N = 1$. Figure 16 shows the Lorentz power per unit mass of tether as given by Eq. (119') within the plasmasphere, for two values of perijove position and a 80 km, 0.05 mm tether ($\lambda = 1.6$); for comparison, at a characteristic position in the Io torus ($r = 6 R_J$, $N_e \approx 2 \times 10^3 \text{ cm}^{-3}$ in Fig.2), we find

$$\frac{|\langle \dot{W} \rangle|}{m_t} \approx 0.016 \frac{\text{kW}}{\text{kg}} \quad \text{at } r = 6 R_J. \quad (119'')$$

Figure 16 shows that power decays rapidly away from the perijove, which is a result of the density profile being very steep near Jupiter. Over most of the plasmasphere the Lorentz force has thus a negligible effect on the SC dynamics. The tether, however, can be used there to generate power. Although the results in Fig. 16 and Eq. (119”) correspond to having no electrical load in the tether circuit, they give the correct order of magnitude for the power on a load of impedance comparable to the impedance of OML current collection.

6.5 – Brief conclusions

At this point we can summarize some preliminary conclusions:

- Rocket thrust can be used to deploy the tether and provide its spin, with no mass penalty on capture and tour operations.
- Tether spin should be opposite Jupiter spin. The accumulative effect of the Lorentz torque on tether spin might be an issue.
- The tether, with *regenerative fuel-cells / batteries* and electric loads plugged in, might serve as its own power source over most of its mission.
- Power saved at high-current operations might possibly be used to power electrical propulsion at SC tour-points where thrusting needs might be a critical issue.

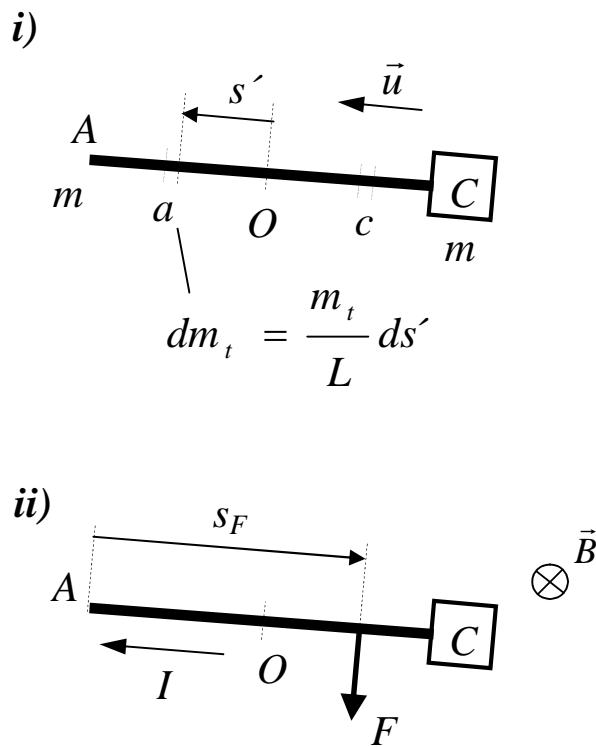


Figure 13. Sketch of torques on the rotating tether; $m = (M_{SC} - m_t) / 2$; point **O** marks the middle of the tether.

i) Gravity-gradient torque. *ii)* Lorentz torque.

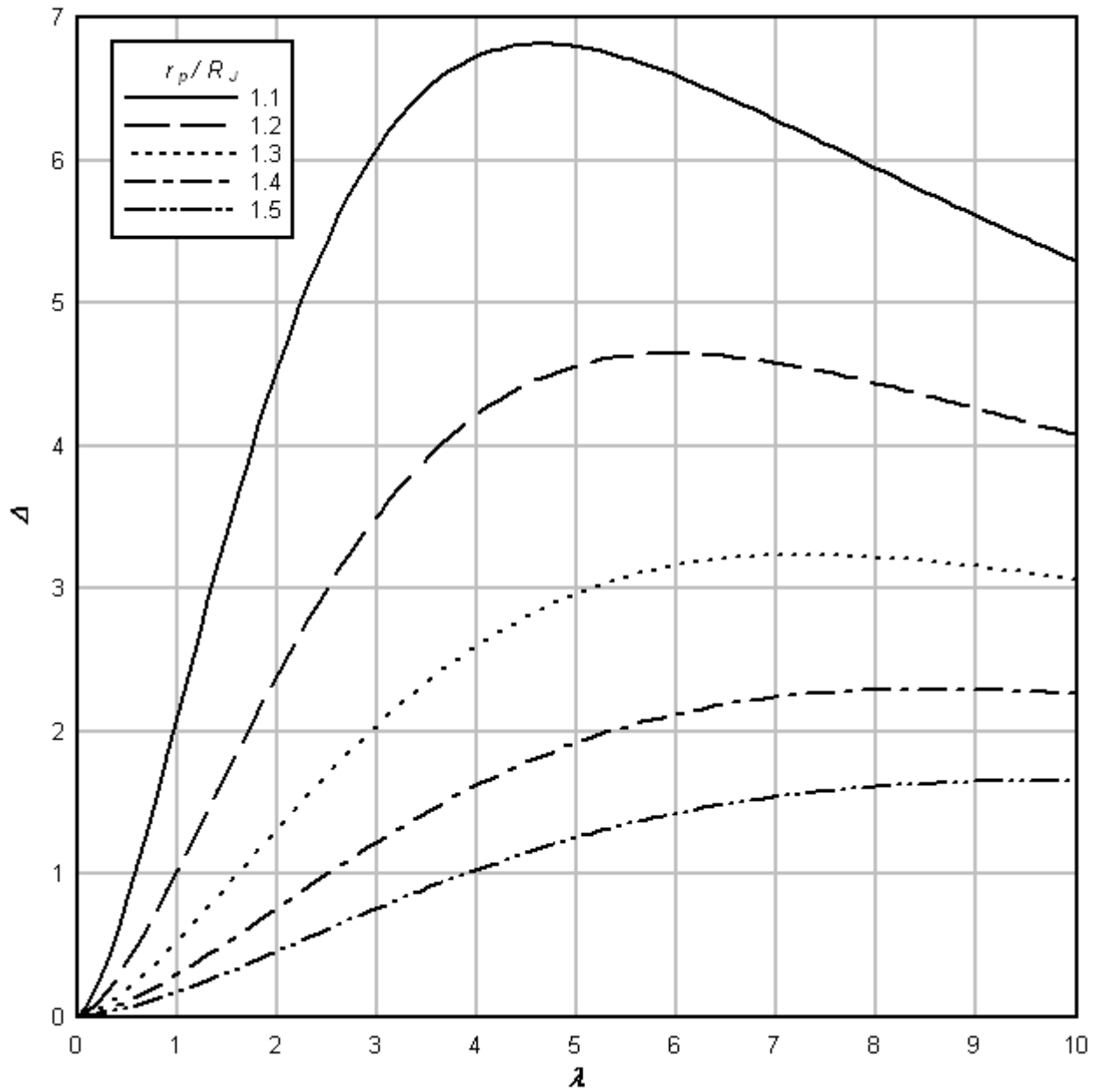


Figure 14. Factor Δ in equation (114) for the variation in tether spin over the full drag arc, versus parameter λ defined in equation (37b), for several values of perijove position.

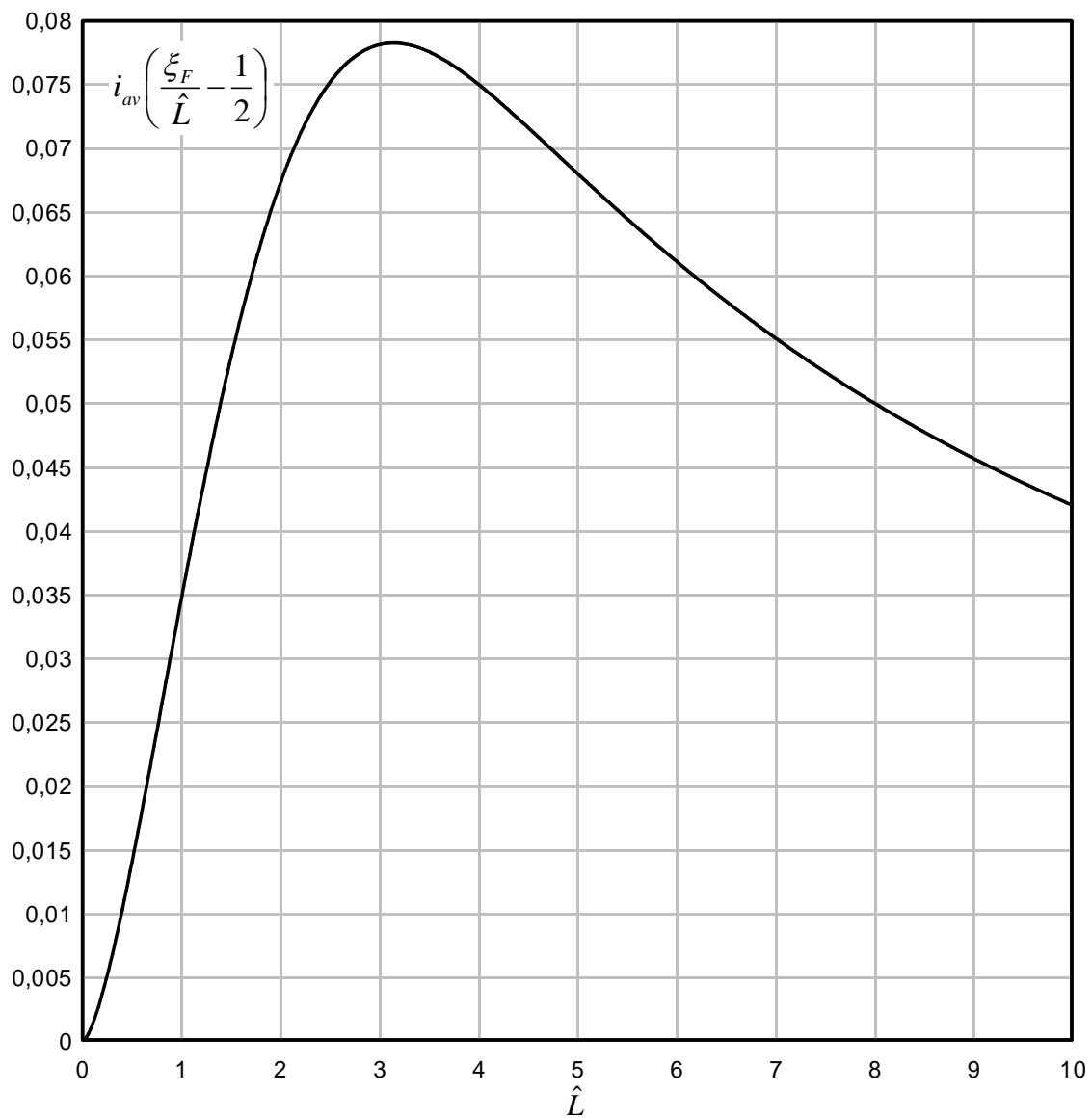


Figure 15. Normalized tether average current times lever arm of Lorentz force with respect to the center of the tether versus normalized tether length, defined through Eqs. (50) and (54).

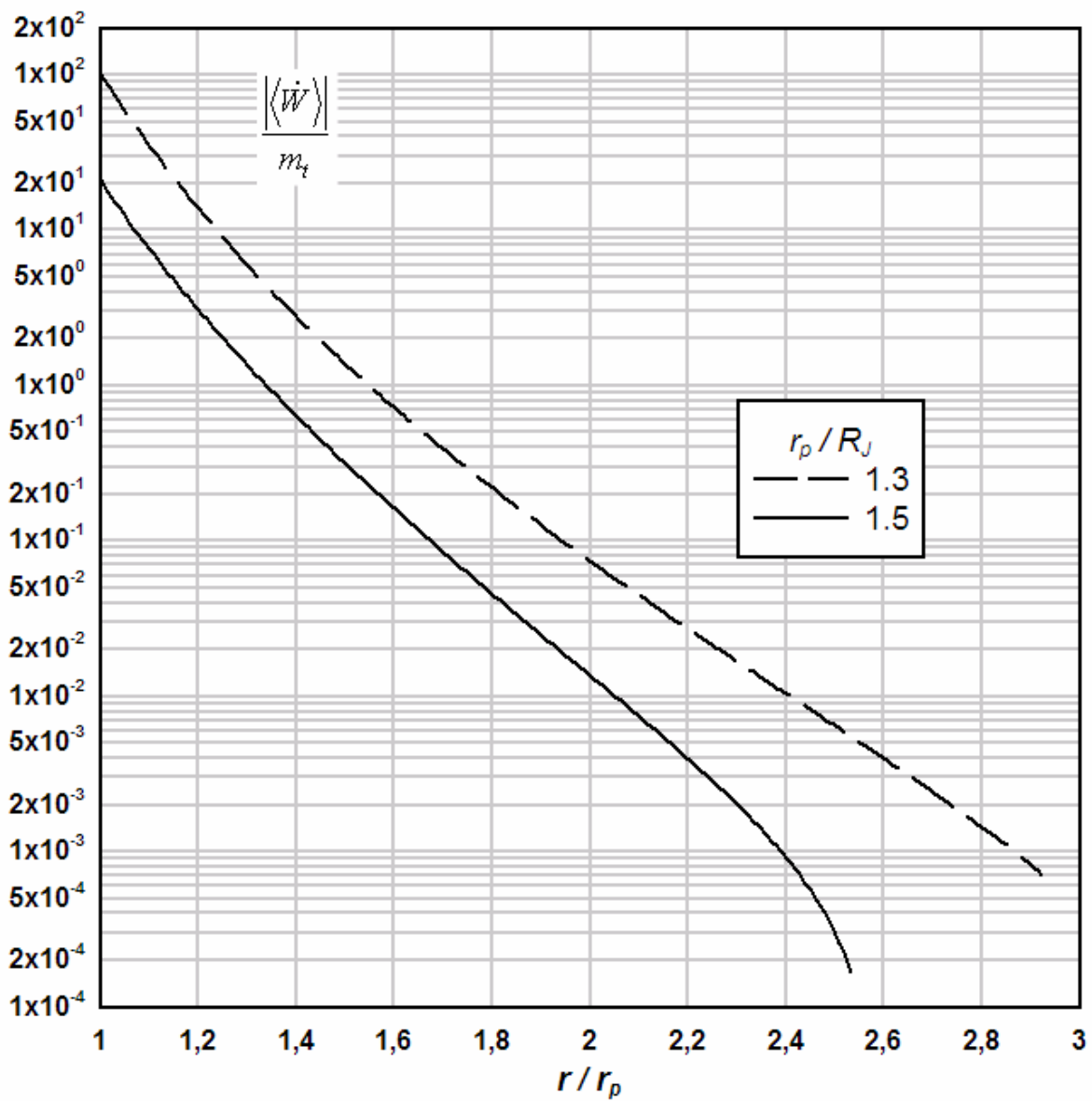


Figure 16. Lorentz-drag power per unit tether mass (kW / kg) versus position along the parabolic orbit of capture, within the plasmasphere ($r < 3.8 R_J$), for two perijove values and parameter λ [defined in equation (37b)] = 1.6.

7 – Tether-operated Jovian missions

We here consider two types of missions, which are made possible because repeated application of the Lorentz force after capture allows modifying the orbital motion of the tethered SC without using propellant. One type involves apojove lowering as suggested in Fig.1. We consider two missions of this type: 1) Frequent flybys of Galilean moons at resonance orbits with perijove around $1.5 R_J$ and 2) acquiring a low circular orbit around Jupiter. The other type of mission involves perijove raising, as also suggested in Fig.1. One such mission is 3) acquiring a low circular orbit around moon Io.

7.1 - Lowering the apojove

If current is again on along a drag arc as the spacecraft returns to the perijove neighborhood, the apojove radius r_a will be reduced. Further reductions will occur at successive perijove passes, resulting in a series of elliptical orbits with common perijove and decreasing eccentricities (changes in the perijove position are small, second-order effects). We can then make the apojove distance r_a meet the orbital radius of any Galilean moon. As with the capture analysis, calculations will be carried out as if eccentricity, though different from unity, was kept constant during each successive pass.

The orbital energy per unit mass of each elliptical orbit can be written as in Eq.(8a),

$$\varepsilon = \frac{-\mu_J}{2r_p} (1-e) \quad \Rightarrow \quad \Delta e = \frac{2r_p}{\mu_J} \Delta \varepsilon. \quad (121)$$

If $\Delta \varepsilon$ were equal to the value at capture, for the $e = 1$ case, $W_C / M_{SC} = -(1 + \beta) v_\infty^2 / 2$, we would have

$$\Delta e = -(1 + \beta) \frac{r_p^2 v_\infty^2}{\mu_J} = -0.018 \times (1 + \beta) \frac{r_p}{R_J} \quad (122)$$

at each pass. As we shall now see, the drag work per pass is indeed independent of e except for low enough e values.

To actually determine $\Delta\varepsilon$, replace Eqs.(9a, b) with the corresponding equations for $e < 1$,

$$v^2 = \frac{\mu_J}{r_p} \left[\frac{2}{\tilde{r}} - (1-e) \right], \quad 1 + e \cos \theta = \frac{1+e}{\tilde{r}}. \quad (123a, b)$$

Using conservation of angular momentum, $r^2 d\theta/dt = r_p v_p$, and Eq. (123b) we get

$$\sqrt{(\tilde{r}-1)(\tilde{r}_a - \tilde{r})} \frac{1-e}{2} dt = \frac{r_p}{v_p} \tilde{r} d\tilde{r}, \quad (124)$$

where $\tilde{r}_a \equiv r_a/r_p = (1+e)/(1-e)$ is the (dimensionless) apojove radius; note that v_p still is here the parabolic ($e = 1$) velocity at perijove used in Ch.4, even though we now have eccentricity $e < 1$. The drag work for an arbitrary eccentricity, $W_{e/d}$, equivalent to Eq. (42'), will then read

$$W_{e/d} = \int \langle \dot{W} \rangle dt = -2 \int_1^{\tilde{r}_u} \frac{r_p \tilde{r} dr \times \sigma_c LwhB^2 \left[v^2 - \omega_J r_p v_{pe} \right]}{v_p \sqrt{(\tilde{r}-1)(\tilde{r}_a - \tilde{r})(1-e)/2}} \times \langle i_{av} \cos^2 \varphi \rangle. \quad (125)$$

The upper limit r_u in the integral above is the smaller of two values: the apojove radius, and the radius where the bracket in the integral vanishes. In the first case, corresponding to low enough apojove and eccentricity, drag will act throughout the entire orbit, from apojove to perijove and back.

Using both Eq. (123a) and $v_{pe} \sqrt{2} = v_p (1+e)^{1/2}$ we have

$$v^2 - \omega_J r_p v_{pe} = 2\mu_J \frac{\tilde{r}_M - \tilde{r} \times \left[\sqrt{2(1+e) + (1-e)\tilde{r}_M} \right] / 2}{r_p \tilde{r}_M \tilde{r}}; \quad (126)$$

Eqs. (43') – (45') are then replaced by the equations

$$\frac{-2W_{e/d}}{m_t v_\infty^2} = \frac{\sigma_c B_s^2 a_s v_s}{2^{5/6} \rho_t v_\infty^2} \times S_e \left(\lambda, \frac{r_p}{R_J}, e \right) \quad (127)$$

$$\Rightarrow 2.11 \times S_e \left(\lambda, \frac{r_p}{R_J}, e \right), \quad (128)$$

$$S_e \left(\lambda, \frac{r_p}{R_J}, e \right) \equiv \tilde{r}_M^{8/3} \times \int \frac{\tilde{r}_u d\tilde{r}}{\tilde{r}^6} \frac{2\tilde{r}_M - \tilde{r} \left[\sqrt{2(1+e) + (1-e)\tilde{r}_M} \right]}{\sqrt{2(1-e)} \times \sqrt{(\tilde{r}-1)(\tilde{r}_a - \tilde{r})}} < 2i_{av} \cos^2 \varphi > \quad (129)$$

Again, note that v_s is the parabolic velocity at a_s , as given in (17). Also, i_{av} is the same function of \hat{L} studied in Ch.4. To find \hat{L} in Eq.(58) (where e was the electron charge), we again use $r^2 d\theta/dt = r_p v_p$ and Eq.(12) to write

$$v'^2 = v^2 - 2\omega_J r_p v_{pe} + \omega_J^2 r^2 \Rightarrow \frac{2\mu_J}{r_p \tilde{r}_M^2 \tilde{r}} \left[\tilde{r}_M^2 + \tilde{r}^3 - 2\sqrt{\frac{1+e}{2}} \tilde{r}_M \tilde{r} - \frac{1-e}{2} \tilde{r}_M^2 \tilde{r} \right]. \quad (130)$$

Equation (58') will hold if we just make the replacement

$$\left(\tilde{r}_M^2 + \tilde{r}^3 - 2\tilde{r}_M \tilde{r} \right)^{1/4} \Rightarrow \left[\tilde{r}_M^2 + \tilde{r}^3 - \left(\sqrt{2}\sqrt{1+e} + \frac{1-e}{2} \tilde{r}_M \right) \tilde{r}_M \tilde{r} \right]^{1/4}. \quad (131)$$

Note that as $e \rightarrow 1$ we indeed have $S_e \rightarrow S$, as given in Eq.(44').

7 – 2 Moon-flybys with perijove around $1.5 R_J$

Figures 17-19 show the function S_e in Eq. (129). As advanced, S_e is nearly independent of eccentricity e ($S_e \approx S$ or $W_{e/d} \approx W_C$) except at small e . Note that, For $r_p = 1.5 R_J$ ($\tilde{r}_M \approx 2.58$), we would have drag acting over the entire orbit, with $r_u = r_a$ in Eq.

(129) for $e < 0.17$ ($r_a < 2.1 R_J$). For $r_p = 1.1 R_J$ ($\tilde{r}_M \approx 4.11$), we would have $r_u = r_a$ for $e < 0.29$ ($r_a < 2.0 R_J$), which is roughly the eccentricity range showing a rapid increase of S_e in Fig. 18.

We can now readily describe orbit evolution in terms of the number of successive perijove passes. For $r_p = 1.5 R_J$ and $\lambda = 1.6$ (corresponding to a 80 km, 0.05 mm tether), β would need be low to ensure capture in Fig.10, as noticed in Ch. 5; for $\beta = 0.5$ say, Eqs. (8b) and (122) then yield $e_1 = 0.986$ and an eccentricity decrement $\Delta e = -0.041$. For simplicity we here set $e_1 = 0.98$ and $\Delta e = -0.04$. A series of passes at fixed perijove, with repeated small decrements in eccentricity, would lead to a sequence of e values, 0.98, 0.94, 0.90, 0.86, 0.82, 0.78, 0.74, 0.70, 0.66, 0.62,... The orbital period of the SC after each perijove pass is $\tau_{orb} \propto [r_p / (1 - e)]^{3/2}$, yielding a corresponding sequence of periods in days, 80.3, 15.4, 7.2, 4.3, 3.0, 2.2, 1.7, 1.4, 1.1, 0.97, ...

Following the first orbit after capture, the tethered-spacecraft apojove could be made to rapidly reach the orbits of the Galilean satellites. Note that elliptical orbits with perijove around $r_p = 1.5 R_J$ and apojove at the orbits of Io, Europa and Ganymede, would be at resonances 2:1, 9:4, and 5:2 with the respective moons. Drag fine-tuning at perijove passes by switching hollow cathodes and current appropriately, would result in a first flyby of any of those moons. Switching off the current afterwards over the entire corresponding orbit would allow repeated flybys, with the moon overtaking, each time, the slower moving SC.

Consider the moon Ganymede, its orbital radius being about $15.0 R_J$. The eccentricity of an elliptical orbit with perijove at $1.5 R_J$ and apojove at $15.0 R_J$ is $e \approx 0.82$. For the small $\Delta e = -0.04$ decrement mentioned above, the SC could reach that eccentricity with four passes following capture. The time invested in reaching that first apojove flyby, from the perijove capture pass would be a total of about 109 days. Each following flyby would require 5 SC

orbits, and a time lapse that is twice the Ganymede orbital period, or 8 times Io's period, i.e., $8 \times 1.77 \text{ days} = 14.2 \text{ days}$.

The orbital radius of Io is about $5.9 R_J$, the corresponding SC-orbit eccentricity for perijove at $1.5 R_J$ being 0.59. It could be reached in ten current-on perijove passes following capture, the total time to that first apojove flyby being 118 days. Each additional flyby would require 2 SC orbits, and a time lapse that is the Io orbital period of 1.77 days. In turn, the orbital radius of moon Europa is $9.4 R_J$, the corresponding SC-orbit eccentricity being 0.72. It could be reached in seven perijove passes following capture. Each flyby would require 9 SC orbits, and a time lapse that is four times the Europa orbital period, i.e. again 8 times Io's period, or 14.2 days.

The extremely frequent access of the tethered SC to the orbits of Galilean moons is to be compared to the frequency of visits in the *Galileo* mission. Galileo made 34 close encounters or flybys in almost 8 years. It thus took nearly three months on the average from one visit to the next. Notice, however, that the tethered SC would orbit through the intense radiation belts near Jupiter on each visit to a moon; radiation dose calculations are discussed in the next section.

To reduce the number of orbits (and the radiation dose) required to get the SC apojove to the orbit of any of those moons, prior to a sequence of visits, the eccentricity jump per orbit Δe should be as large as possible. Use of $\Delta \varepsilon = W_{el/d}/M_{SC}$ and Eqs. (121) and (127) yields

$$\Delta e = - \frac{r_p v_\infty^2}{\mu_J} \times \frac{m_t}{M_{SC}} \times \frac{\sigma_c B_s^2 a_s v_s}{2^{5/6} \rho_t v_\infty^2} \times S_e. \quad (132)$$

Following conclusions in Ch.5, $|\Delta e|$ can be increased, at given r_p , L , and mass ratio, by reducing tape thickness and density. Note that $|\Delta e|$ is independent of v_∞ and β , whereas the first eccentricity after capture decreases with them, as it follows from Eqs. (7) and (8b),

$$1 - e_1 = \beta \times \frac{r_p v_\infty^2}{\mu_J}. \quad (133)$$

7 – 3 A mission to low orbit around Jupiter

Figures 17-19 show S_e steepening with decreasing e after a long stretch at nearly constant value. Getting the apojuve fully down to a perijove radius $1.5 R_J$ could require about 20 perijove passes following capture. The SC would finally be in a low circular orbit around Jupiter. Then, switching on the current over the entire $1.5 R_J$ orbit would make the SC to spiral inwards to reach some altitude optimal for a full exploration of the planet. Note that the SC will be free of damaging radiation effects once it reaches down to an orbit lying within $1.3 R_J$, roughly. Here stands the inner edge of the radiation belt, where belt electrons are lost through a variety of mechanisms that include scattering to the atmosphere of Jupiter, and energy loss through synchrotron emission.

A simple benchmark for estimating radiation effects over the orbit evolution of the tethered spacecraft would be a calculation of dose over the parabolic orbit of capture. Calculations were carried out starting at $15 R_J$ inwards and ending at $15 R_J$ outwards, using the GIRE radiation model, which is an updated version of the 1983 Divine-Garrett model for energetic particles beyond $8 R_J$, as mentioned in Ch.3. A more recent modification for the range $2 - 4 R_J$, introduced to better modelling synchrotron emission itself and also discussed in Ch.3, has a weaker effect on radiation dose and was not included.

Figure 20 shows the 1-MeV electron fluence (typically characterizing internal charging effects) for both $1.2 R_J$ and $1.5 R_J$ capture perijove, as function of its West Longitude in standard SIII coordinates. Fluence, which is particle flux at any given energy integrated over time, is a proxy for dose. The dependence on longitude is weak, reflecting the low values of both tilt and offset of the dipole describing the magnetic field in the inner magnetosphere,

which we had just ignored in our analysis of capture and orbit evolution. At distances so close to Jupiter, fluence decreases, though weakly, as the perijove is located closer and closer to the planet. The fluence of 20 MeV protons was found to be smaller by $1\frac{1}{2}$ orders of magnitude.

Figure 21 shows the omnidirectional fluence spectra of both electrons and protons for perijove at 200° and 290° W longitudes (roughly corresponding to minimum and maximum of fluences) and $1.2 R_J$ and $1.5 R_J$ perijove distance. Note that, for each species, the curves of all four cases are near indistinguishable. Electron fluence exceeds proton fluence beyond about 0.8 MeV.

Figure 22 shows dose/depth curves for the four perijove cases. Dose involves both fluence and the stopping power of some shielding material, typically aluminium; for any given shield-thickness, incident particles below some energy will not come out at the opposite side of the shield. As a result, radiation dose, characterizing damage to some reference material (silicon) placed behind the shield, will decrease with shield thickness. A geometrical standard shielding configuration was used in the calculation of radiation dose, the generic code involving an aluminium spherical shell for all 4π steradians. Figure 22 shows that dose is not strongly dependent on perijove position, as regards either its longitude or its distance from Jupiter. Full dose over the radiation capture is about 39 krad(Si) and 49 krad(Si) for 10 mm shield, and $r_p = 1.2 R_J$ and $1.5 R_J$, respectively. It is generally accepted that electronic equipment to use in future Jovian missions will need be hardened well over 1 Mrad(Si), with thickness equivalent to 10 mm Al; using a tantalum shield to reduce mass has been suggested.

If one proceeds along a sequence of orbits of decreasing apojove, comparable values of dose per orbit result. For our rough calculations we used dose (per-unit-time) rates versus distance to Jupiter $\dot{D}_s(r)$, for several shield thickness, as obtained in a mission-to-Jupiter ESA study using the Divine/Garrett model [P.Renard *et al.*, in *System Concepts...*, IAC-04-Q.2a.02 paper / 2004 / (Fig,4)]. We extrapolated dose-rate profiles to the region near Jupiter

in order to fit Fig. 22 for the parabolic orbit, but ignored modifying the profiles beyond $8 R_J$, as prescribed at GIRE, because the relative effect on the dose for orbits reaching inwards through the intense region near Jupiter is actually weak; we then conservatively extrapolated results for shielding thickness from less than 8 mm to 10 mm. The dose increment $\Delta D_s(r_p, e)$ over a full elliptical orbit of given perijove r_p and apojove $r_a = r_p \times (1 + e)/(1 - e)$ is then given as

$$\Delta D_s \left(e, \frac{r_p}{R_J} \right) = 2 \int_1^{\tilde{r}_a} \frac{r_p}{v_p} \frac{\dot{D}_s(\tilde{r}) \tilde{r} d\tilde{r}}{\sqrt{(\tilde{r}-1)(\tilde{r}_a-\tilde{r})}} \sqrt{\frac{2}{1-e}}, \quad \tilde{r}_a = \frac{1+e}{1-e}, \quad (134)$$

with dose rate \dot{D}_s in the integrand neglected if beyond $15 R_J$. Figure 23 shows the dose increment per orbit, for two perijove values, versus eccentricity (or equivalently, apojove). Figure 24 then presents the accumulated dose for two sequences of orbits corresponding to moderate decrements of eccentricity per orbit. Circular orbits around Jupiter, below the radiation belt, can be reached with accumulated dose under 1 Mrad(Si) for 10 mm shield. The SC could make over 25 flybys of Io before the accumulated dose exceeds 3 Mrad(Si), for a total mission duration of over five months after capture. It would take about 12 flybys of Ganymede to reach a similar dose, the corresponding duration being about nine months.

7 – 4 Getting a tethered SC into low orbit around Io

Once the apojove of a tethered spacecraft has reached down to the Io torus, an orbit evolution alternative to a series of flybys might get the SC into a low circular orbit around Io. The operation would involve switching off the current at each perijove pass and switching it on within the torus, around apojove, to produce thrust. Use of the high plasma density inside the torus may then lead to an inverted process of orbit evolution, with apojove fixed and perijove progressively increased; note that the eccentricity would keep decreasing, however.

Figure 2 represented radial density and temperature profiles, corresponding to the Divine-Garrett model. The density profile in the plasmasphere ($r < 3.8 R_J$) is described by Eq.(36). We note that r is radial distance in a plane tilted, with respect to the equator, $2/3$ of the small magnetic-dipole tilt with respect to the spin of Jupiter (which is about 9.6°); the density scale height perpendicular to that plane, however, is large enough in the plasmasphere to allow using the profile in Eq.(36) for our equatorial orbits.

On the other hand, the (ion) temperature T_i in the inner torus gets so low that the scale height is small enough for the torus tilt to affect the plasma density found by a SC in an equatorial orbit; note, however, that the small angle ($\alpha = 6.4^\circ$) of the tilted plane still allows use of r as radial distance in the equator itself. The early Divine/Garrett model gives the density at points in the equator, within the torus, as

$$N_e = N \times \exp \left[- \left(\frac{r \tan \alpha \times \cos l}{0.2 R_J \times \sqrt{2} \times \sqrt{k T_i / 1 eV}} \right)^2 \right], \quad (135)$$

where $N(r)$ and $T_i(r)$ are as given in Fig. 2, l is longitude measured from some reference meridian, and the $\sqrt{2}$ factor accounts for a temperature correction introduced in 1985 (F.Bagenal *et al.*, J. Geophys. Res. **90**, 1755 / 1985).

The speed of the corotating torus is about $(5.9 / 2.24)^{3/2} \approx 4.27$ times greater than the speed of Io, which moves itself faster than the SC when in its apojove neighbourhood, inside the torus, in any of the successive elliptical orbits. The longitude l at the SC position will thus vary fairly rapidly in Eq. (135), as the torus sweeps past the SC. We now simplify calculations by averaging Eq. (135) over a full torus revolution, to get a ‘mean’ density N_{em} to use in determining tether currents,

$$N_{em}(r) \approx N(r) \times \int_0^{\pi/2} \frac{2}{\pi} dl \exp \left[- b(r) \cos^2 l \right] \equiv N(r) \times F(r), \quad (136a)$$

$$b \equiv \left(\frac{r \tan \alpha}{0.2 \sqrt{2} \sqrt{T_i(\text{eV})} R_J} \right)^2 \approx \frac{0.157}{T_i(\text{eV})} \times \left(\frac{r}{R_J} \right)^2. \quad (136b)$$

The “mean radial” profile N_{em} is also represented in Fig. 2. Errors arising from the fact that the torus-to-SC speed ratio is only moderately large should be broadly washed out by the fact that, as we shall later see, the number of orbits required to raise the perijove to the torus is itself large.

The latitudinal scale height in the torus is still poorly established, as opposite the equatorial density profile. In general, possible temperature differences among species and possible temperature anisotropies, as well as the fact that electron temperature catches up with T_i when moving from the center to the inner region of the torus, keep a degree of uncertainty in torus thickness. This does affect the torus scale height, which still appears as an open issue. Figure 2 also shows a “mean” density profile higher than as given in Eqs. (136), with $N_{em} = N(r) \sqrt{F(r)}$, which roughly accounts for late Voyager data that indicate greater latitudinal broadening in the “ribbon” torus region from $5.7 R_J$ to $5.9 R_J$, as mentioned in Ch.3 (F. Bagenal, J. Geophys. Res. **99**, 11043 / 1994). Finally, we are taking into account recent Galileo data suggesting that the plasma density in the torus is higher by a factor of 2 than obtained from Voyager data, as also mentioned in Ch.3 (F.J.Crary *et al.*, J. Geophys. Res. **103**, 29359 / 1998); we will thus use a “mean” torus density

$$N_{em}(r) \equiv 2 \times N(r) [F(r)]^{1/2}. \quad (137)$$

Equations (127)-(129) for elliptical orbits can be readily rearranged to describe the thrust work for arbitrary eccentricity $W_{e/t}$ by writing

$$-W_{e/d} \Rightarrow W_{e/t}, \quad \tilde{r} \equiv \hat{r} \times \frac{1+e}{1-e}, \quad \hat{r} = \frac{r}{r_a}. \quad (138a, b)$$

We then have

$$\frac{W_{e/t}}{m_t v_\infty^2 / 2} = \frac{\sigma_c B_s^2 a_s v_s}{2^{5/6} \rho_t v_\infty^2} \times I_o \left(\lambda, \frac{r_a}{R_J}, e \right) \quad (139)$$

$$I_o = \left(\frac{a_s}{r_a} \right)^4 2^{4/3} \int_{\hat{r}_l}^1 \frac{d\hat{r} \langle 2i_{av} \cos^2 \varphi \rangle}{\hat{r}^6 \sqrt{(\hat{r} - \hat{r}_p)(1 - \hat{r})}} \times \left[\hat{r} \left\{ \sqrt{\frac{1-e}{1+e}} + \sqrt{1+e} \left(\frac{a_s}{r_a} \right)^{3/2} \right\} - \frac{2}{\sqrt{1+e}} \left(\frac{a_s}{r_a} \right)^{3/2} \right] \quad (140)$$

with the lower limit in the integral being the larger of two values: the perijove radius, and the radius where the bracket vanishes. In the first case, thrust will act over the entire elliptical orbit, from perijove to apojove and back. Equation (128) can be rewritten accordingly too, and the (mean) density profile given by Eq.(137) is then used in Eq. (58) for \hat{L} .

Equation (121) can also be rearranged to read as

$$\varepsilon = \frac{-\mu_J}{2r_a} (1+e) \quad \Rightarrow \quad \Delta e = -\frac{2r_a}{\mu_J} \Delta \varepsilon. \quad (141)$$

Use of $\Delta \varepsilon = W_{e/t}/M_{SC}$ and Eq. (139) finally gives

$$\Delta e = -\frac{r_a v_\infty^2}{\mu_J} \times \frac{m_t}{M_{SC}} \times \frac{\sigma_c B_s^2 a_s v_s}{2^{5/6} \rho_t v_\infty^2} \times I_o. \quad (142)$$

Figure 25 shows I_o versus eccentricity, for apojove at $5.9 R_J$, around the Io orbit, and several values of parameter λ .

Comparing Eq. (132) with Eq.(142), and Figs. 18 or 19 with Fig.25, shows dramatically that raising the perijove from near Jupiter to the Io torus will require a very large number of apojove passes. Basically the low I_o values are a result of a dipole magnetic field decreasing as the cubed inverse power of distance; for the weak ohmic effects case of interest,

the Lorentz force will roughly vary locally as $B \times N_e$, “mean” plasma densities in the torus being comparable to densities near Jupiter.

Note also that the orbit arc where thrust applies is typically larger than the drag arc in the ratio r_a / r_p ; this is reflected in the factor r_a in (142), as compared with r_p in (132), and partially compensates the disparity in S_e and I_0 values. Independently, the full time required for raising the perijove to the torus is actually moderate because each orbit takes less than, or about, one day. The radiation dose accumulated during the entire orbit sequence appears unacceptable, however. Figure 26 presents the dose per orbit versus eccentricity (or equivalently, perijove) for apojoyve at Io. For $r_a = 5.9 R_J$ and $M_{SC} = 3 m_t$, Eq.(142) becomes

$$\Delta e \approx 0.075 I_0. \quad (142')$$

Taking $I_0(\text{av}) = 0.06$ as an average value in the $0 < e < 0.59$ range for $\lambda = 1.6$ in Fig.25, the number of torus passes required to raise the perijove from its initial value $1.5 R_J$ to the Io orbit would be

$$\text{Number of apojoyve passes} \approx 0.59 / 0.075 \times 0.06 \approx 130.$$

The entire sequence might require just about 4 months, ending about 8 months after capture. However, taking 55 krad as a mean dose per orbit from Fig. 26, and adding the 500 krad accumulated in first getting the apojoyve to the Io orbit, as discussed in Secs.7.2 / 7.3, would yield a total dose of about 7.5 Mrad(Si) behind 10 mm Al shielding for carrying the SC into low orbit around Io. As with Eq. (132), Δe can be increased in (142) by reducing tape thickness and density.

Independently, we have explored whether it might be advantageous to thrust from apojoyve slightly below or above Io itself; Figs. 27 and 28 present results corresponding to $r_a / R_J = 5.5$ and 6.5 respectively. We further considered first thrusting from an apojoyve down at the plasmasphere (beyond the stationary orbit), where density is lower than at the torus but the magnetic field is much larger (Fig.29). Comparing Figs. 25, 27 - 29 suggests that thrusting

near the Io orbit (Fig.25) is best for realistic values $\lambda \sim 1 - 2$, though thrusting at a lower apojoove would be better in case high λ values were attainable.

Regarding Fig.29, note that once the orbit is made circular at $3.25 R_J$, raising the full orbit to the torus still requires further thrust at the plasmasphere to first raise the apojoove, then thrust at the torus to bring the perijoove there. On the other hand, eccentricities would be low throughout the entire process. Figures 25 and 27-29 show that thrusting is less efficient at the highest eccentricities. Possible preliminary use of an electrical thruster (powered by energy saved from the high-current drag-passes that lowered the apojoove to the Io orbit) for limited perijoove rise, would make tether start thrusting at lower eccentricity apojoove passes. A complete sweep of possible orbit sequences is required for definite conclusions.

7.5 - Survivability of tape tethers to micrometeoroids

The distribution of micrometeoroids (MM) in deep space around Jupiter can be taken as isotropic. Very near the planet there is a focusing effect of its gravity (which increases both MM flux and velocity), and some shielding from the planet itself. Most of the time after capture, however, SC and tape will not be very close to Jupiter. As a result, tape and round-wire tethers with both length and cross-section area equal (and having thus equal mass) would present quite different probabilities of survival against MM impacts.

A round tether will respond to the MM flux equally around its perimeter, thanks to both flux isotropy of the distribution and tether cylindrical symmetry. Survival estimates involve the flux for MMs above some critical size; in simple calculations the critical particle diameter d_{cp} for wire severance is taken to be equal to 1/3 the wire diameter, d_w . A tape, however, reacts differently to strikes along the edge or normal to the side.

In case of a thin tape of width $w = \pi d_w^2 / 4h \gg d_w$, a particle with diameter d_{cp} will only drill a small hole if the impact is perpendicular (or more generally, at not too small incidence) with respect to the tape surface. Particles at such incidence angles will need a much larger critical size because they have to drill a hole of size comparable to the tape width to sever it. On the opposite hand, d_{cp} particles can sever the whole tape if the angle of incidence of the particle with respect to the tape surface is shallow enough. The shallow angle range is small however.

A tape 80 km long, 0.05 mm thick, and 3 cm wide say, could survive 1 year under the micrometeoroid flux near Jupiter with probability very close to unity. It should thus survive the short missions here considered. As regards, the Jovian rings, note that ring-particles are typically 1 – 10 μm large; this is of the order of 10^{-4} times the tape width.

7 – 5 Brief conclusions

At this point we can summarize some preliminary conclusions:

- Following capture, repeated application of Lorentz drag at perijove passes can efficiently lower orbit apojove.
- A tethered SC can rapidly and frequently visit Galilean moons. Elliptical orbits with (capture) perijove at $r_p \approx 1.5 R_J$ and apojoves at Io, Europa and Ganymede orbits, are in resonances 2:1, 9:4, and 5:2 with the respective moons. For a 80 km, 0.05 mm Al tape, and full SC mass 3 times tether mass, about 25 *slow* flybys of Io could take place before the accumulated radiation dose exceeds 3 Mrad(Si) for 10 mm Al shield thickness, reached about 5 months after capture; the respective number of flybys for Ganymede would be 12, reached about 9 months after capture.
- A tethered SC can acquire a safe, low circular orbit around Jupiter (below the radiation belts) and manoeuvre to get an optimal altitude, with no major radiation effects.

- A tethered SC can acquire a low circular orbit around moon Io (by thrusting at the apojove within its torus to raise the perijove from the plasmasphere) in about 4 months, or about 8 months after capture, but the accumulated radiation dose, about 7.5 Mrad S_i , poses a critical issue. Radiation dose for all three indicated missions could be reduced by decreasing tape thickness and density.
- Thrusting at the torus to raise the perijove is more efficient the higher the perijove. Preliminary use of rocket thrust for limited perijove rise could make tether avoid thrusting at inefficient apojove passes.
- Once a full orbit is inside the torus, raising the apojove to moon Europa through a series of (torus) perijove passes would again face a radiation issue.
- A tape 80 km long, 3 cm wide and 0.05 mm thick could survive 1 year in the Jovian environment with probability very close to unity.

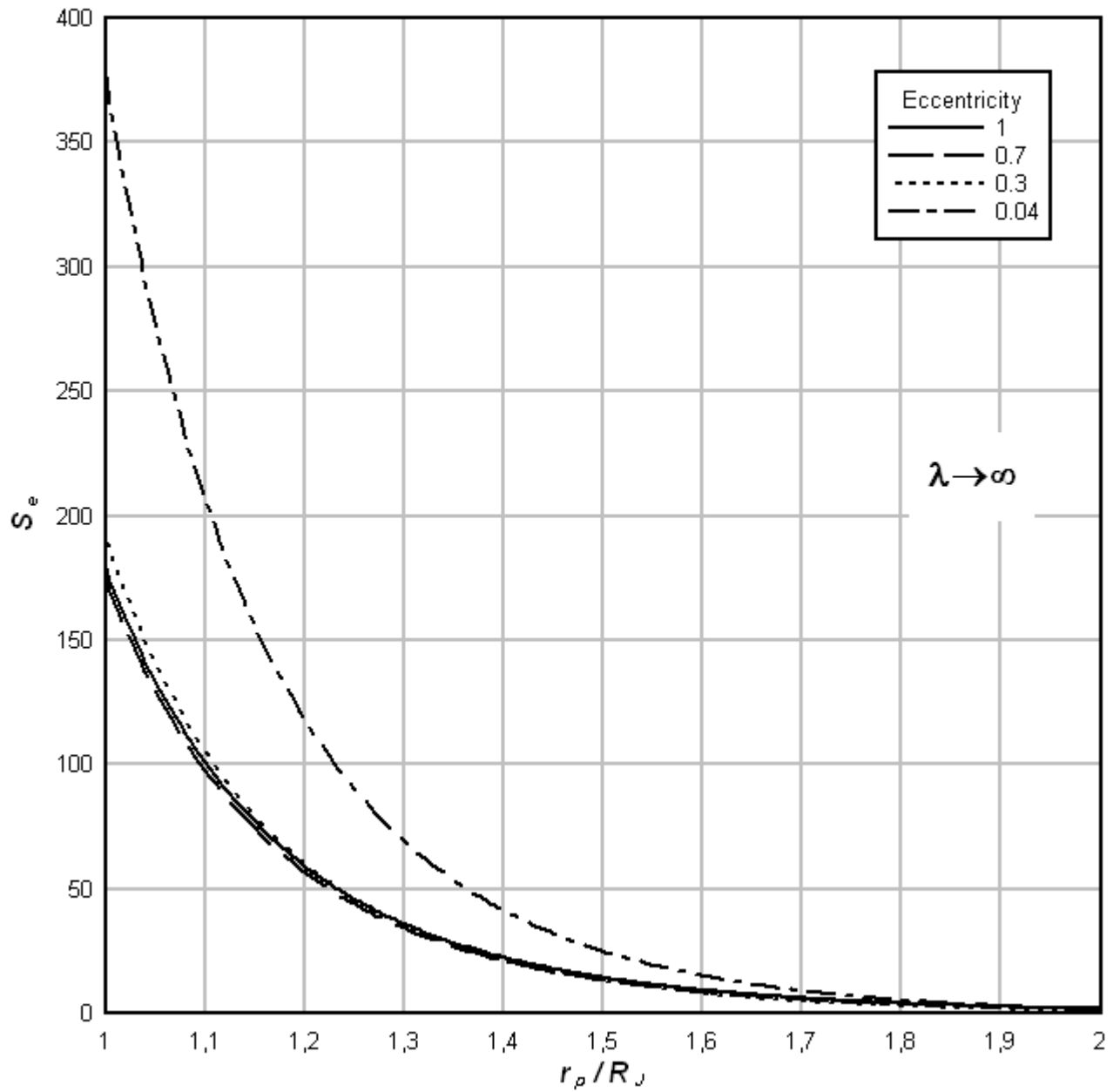


Figure 17. Factor S_e in Eq. (127) for drag work per orbit versus perijove position, for dominant ohmic effects ($\lambda \rightarrow \infty$) and several eccentricity values

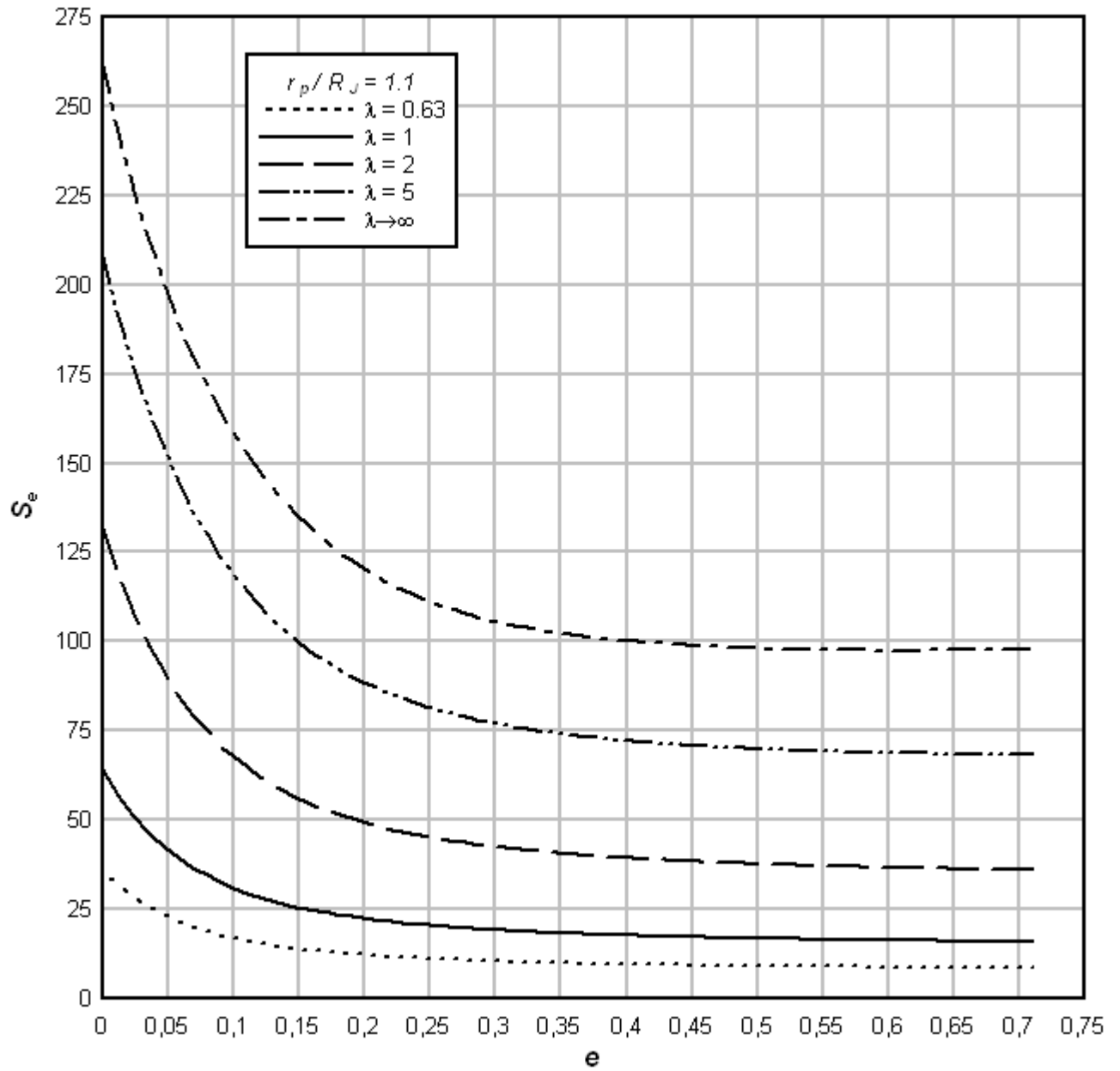


Figure 18. Factor S_e in Eq. (127) for drag work per orbit versus eccentricity, for perijove at $1.1 R_J$ and several values of the parameter λ .

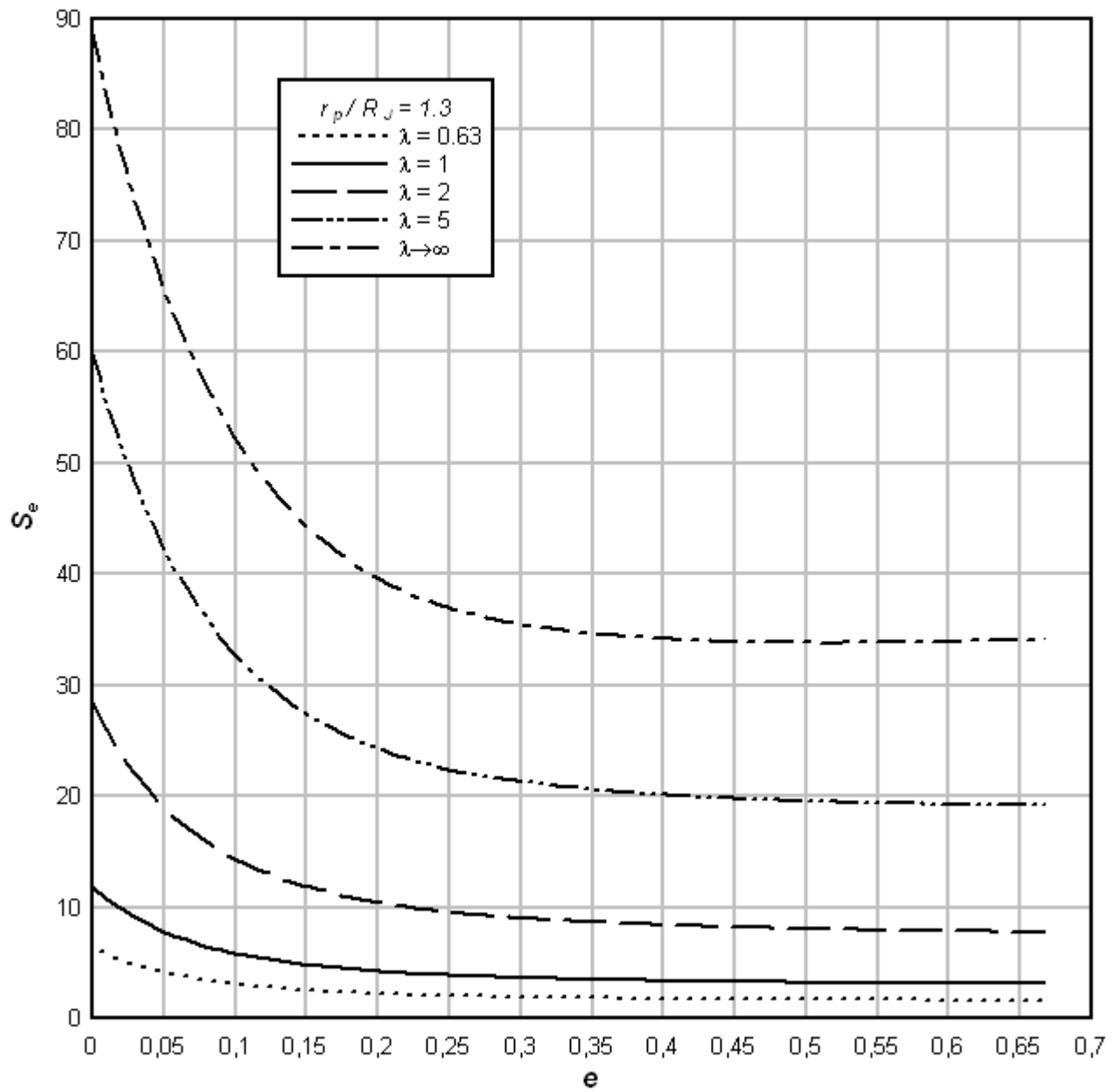


Figure 19. Same as in Figure 18, for perijove at $1.3 R_J$

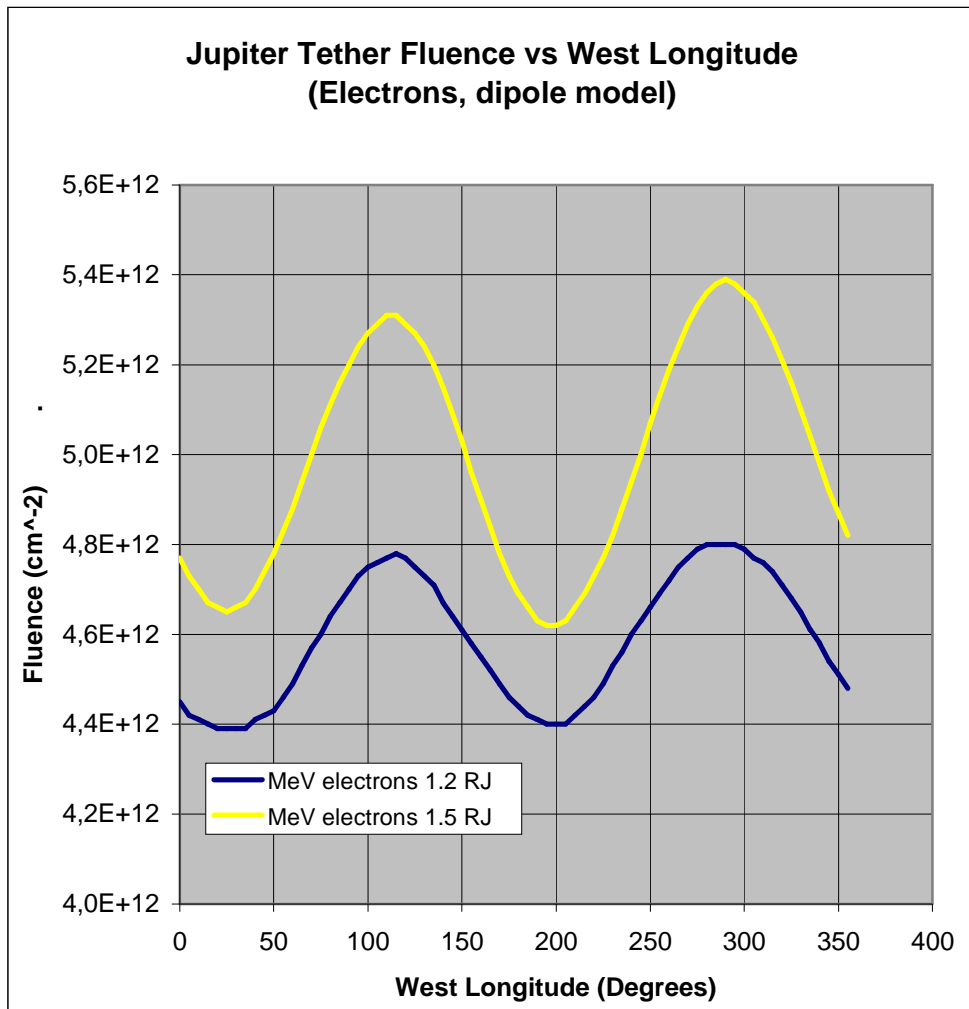


Figure 20. Electron fluence at 1 Mev for an equatorial and parabolic orbit of capture versus West Longitude of perijove, for two values of perijove distance (Garrett and Evans)

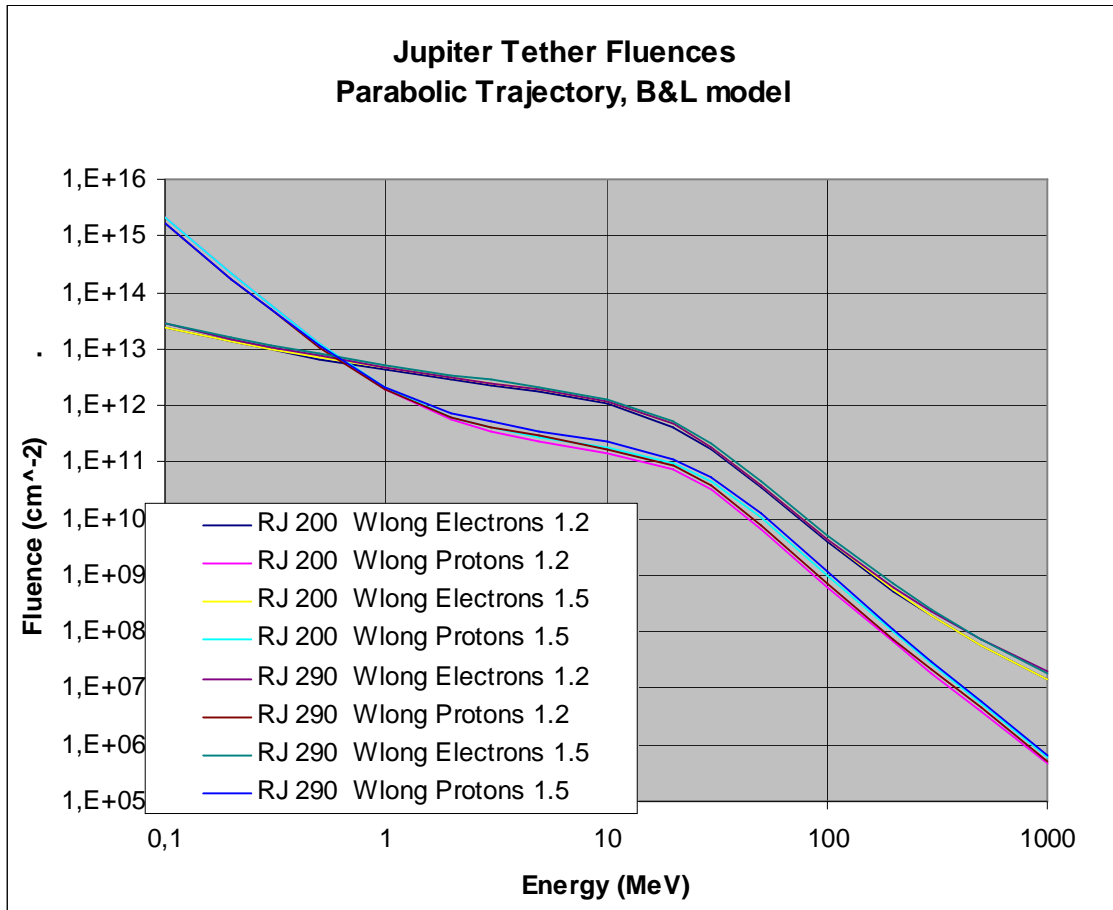


Figure 21. Omni-directional fluence spectra for electrons and protons, perijove longitude 200° W and 290° W, and distance 1.2 and 1.5 R_J, for the capture orbit of Fig. 20 (Garrett and Evans)

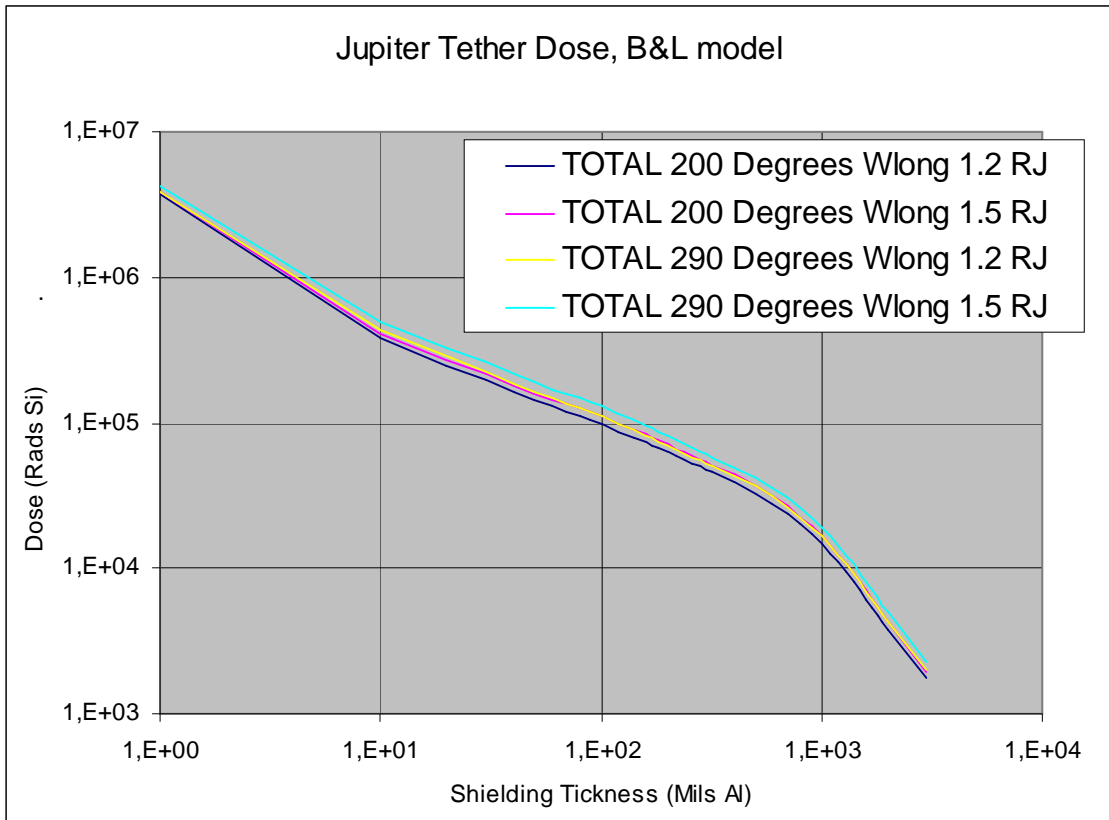


Figure 22. Total dose-depth curves corresponding to Figs. 20 and 21 (Garrett and Evans)

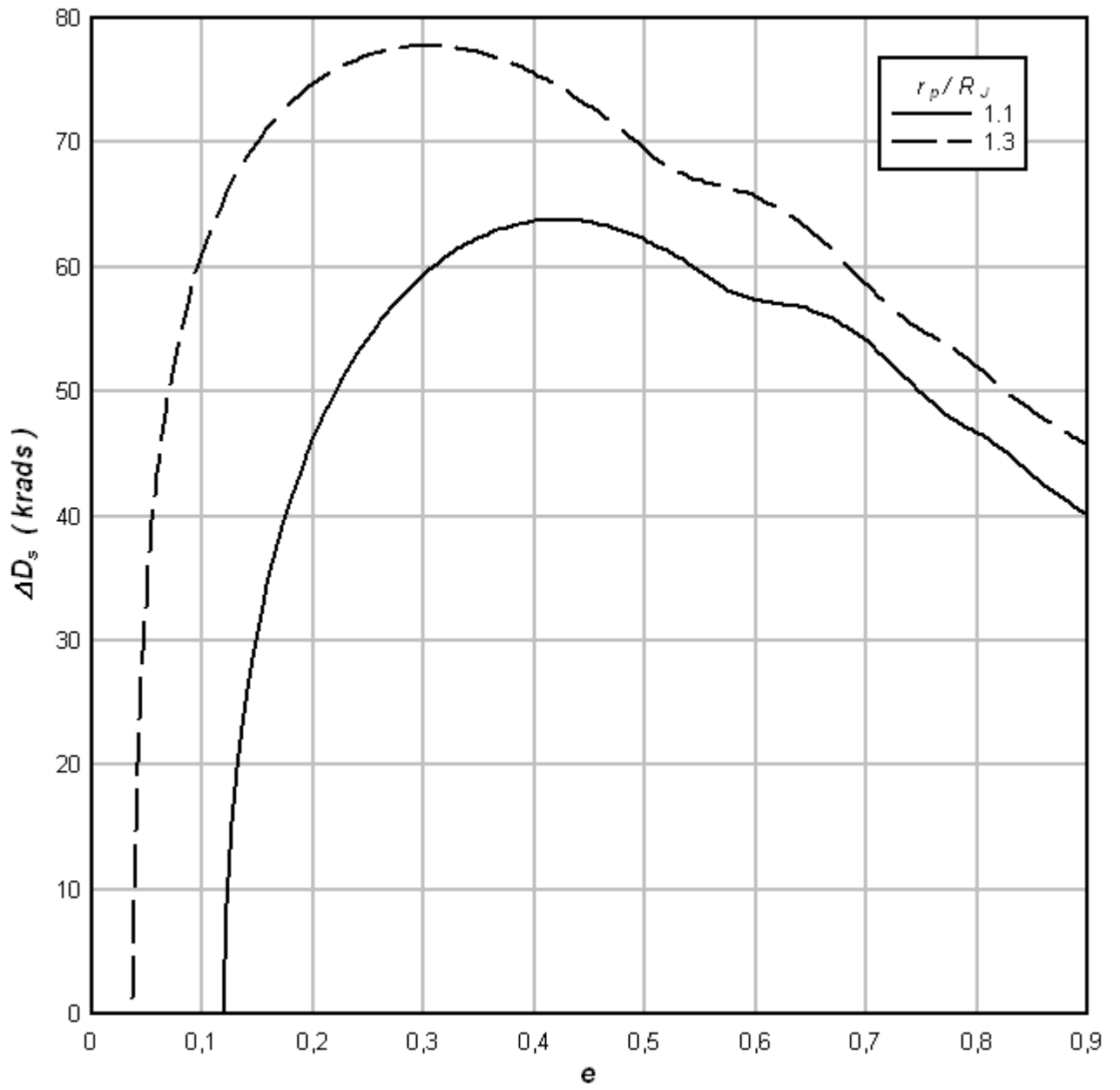


Figure 23. Radiation dose per orbit versus eccentricity for two perijove values and 10 mm Al shield thickness.

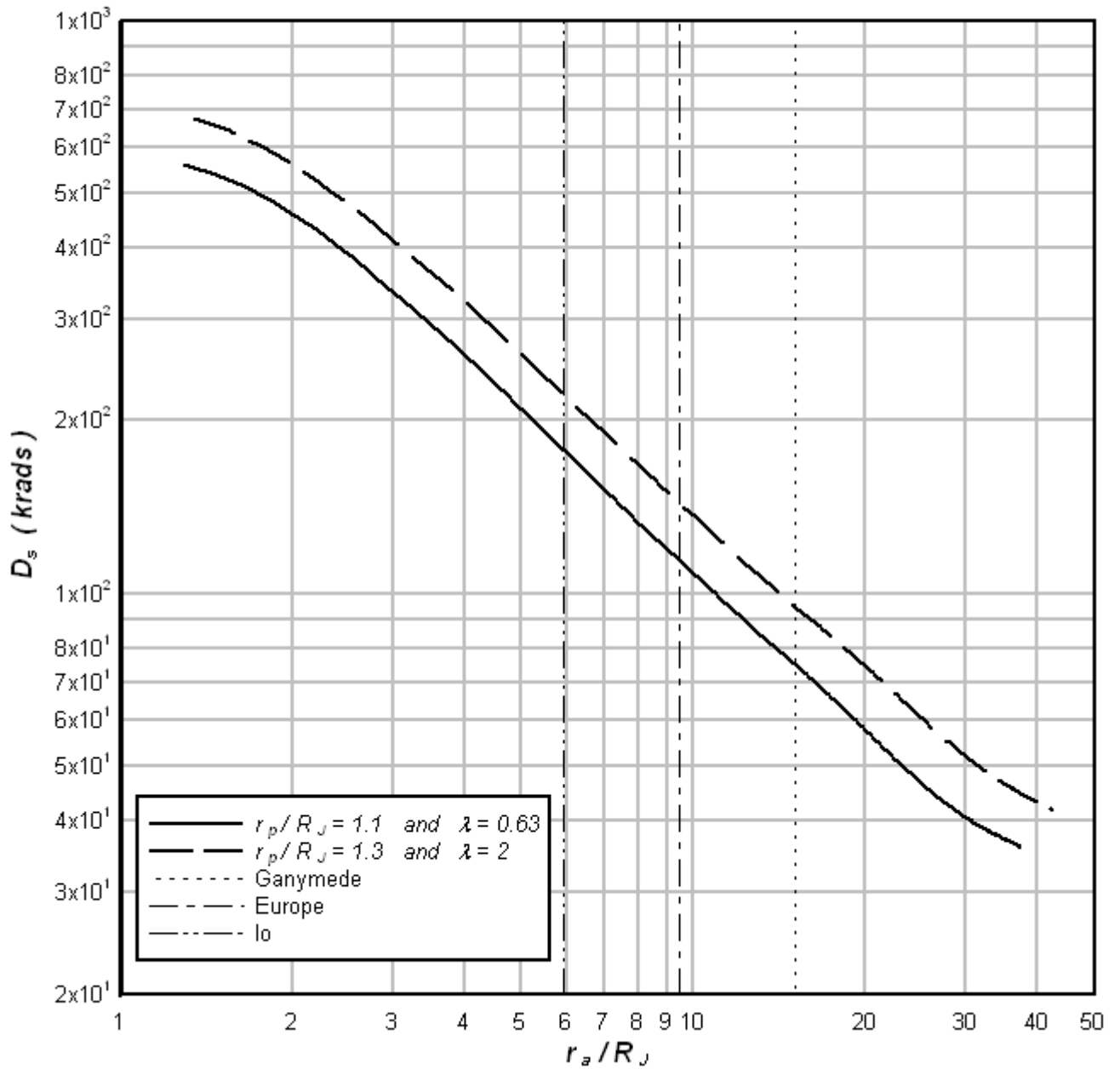


Figure 24. Radiation dose accumulated over the sequence of orbits, from capture down to any particular apojove radius, for two combinations of perijove position and parameter λ resulting in moderately small eccentricity decrements per orbit (10 mm Al shield thickness). Distances from moons to Jupiter are marked.

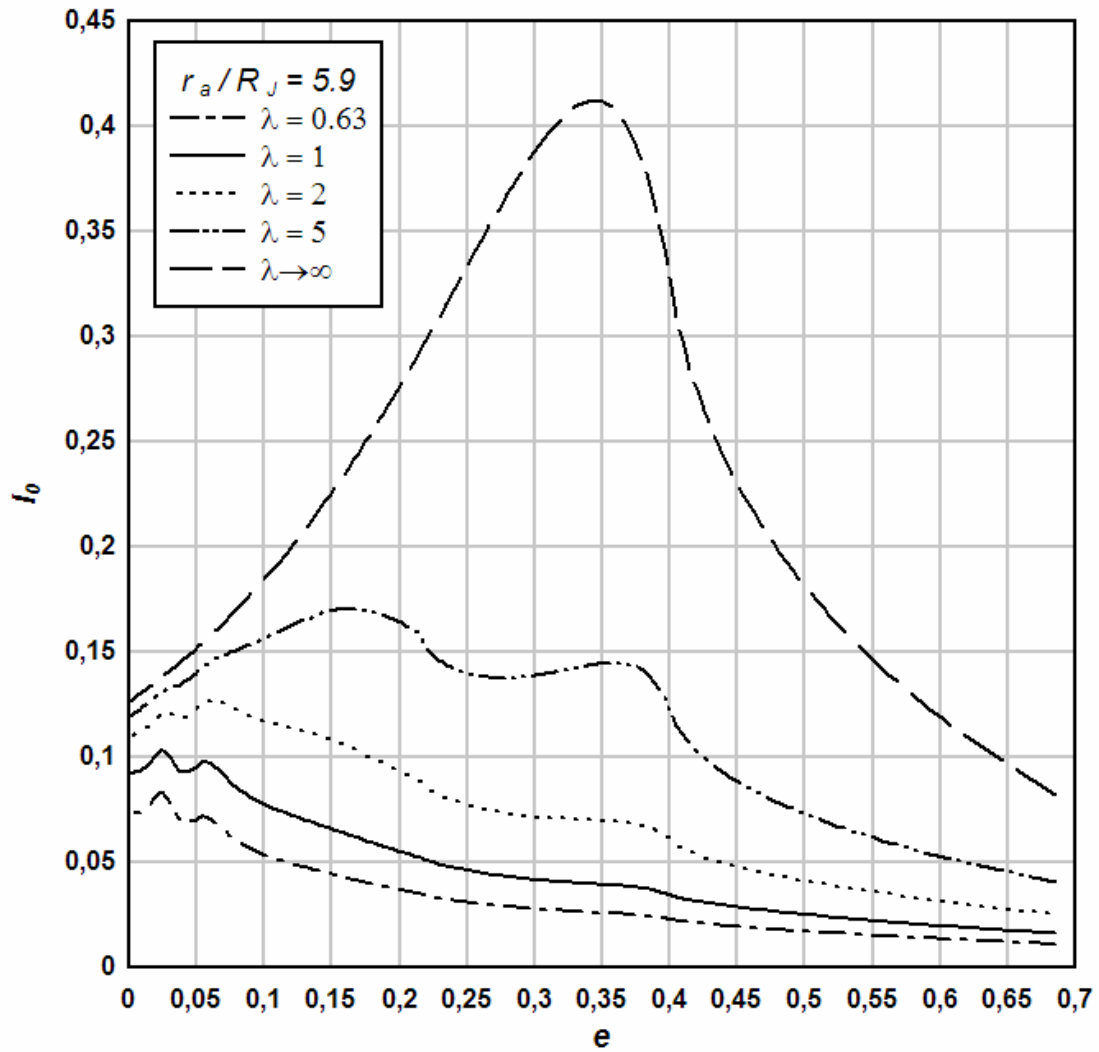


Figure 25. Function I_0 in Equation (139) versus eccentricity, for apojoive at $5.9 R_J$, several values of parameter λ , and the higher torus “mean” density in Figure 2.

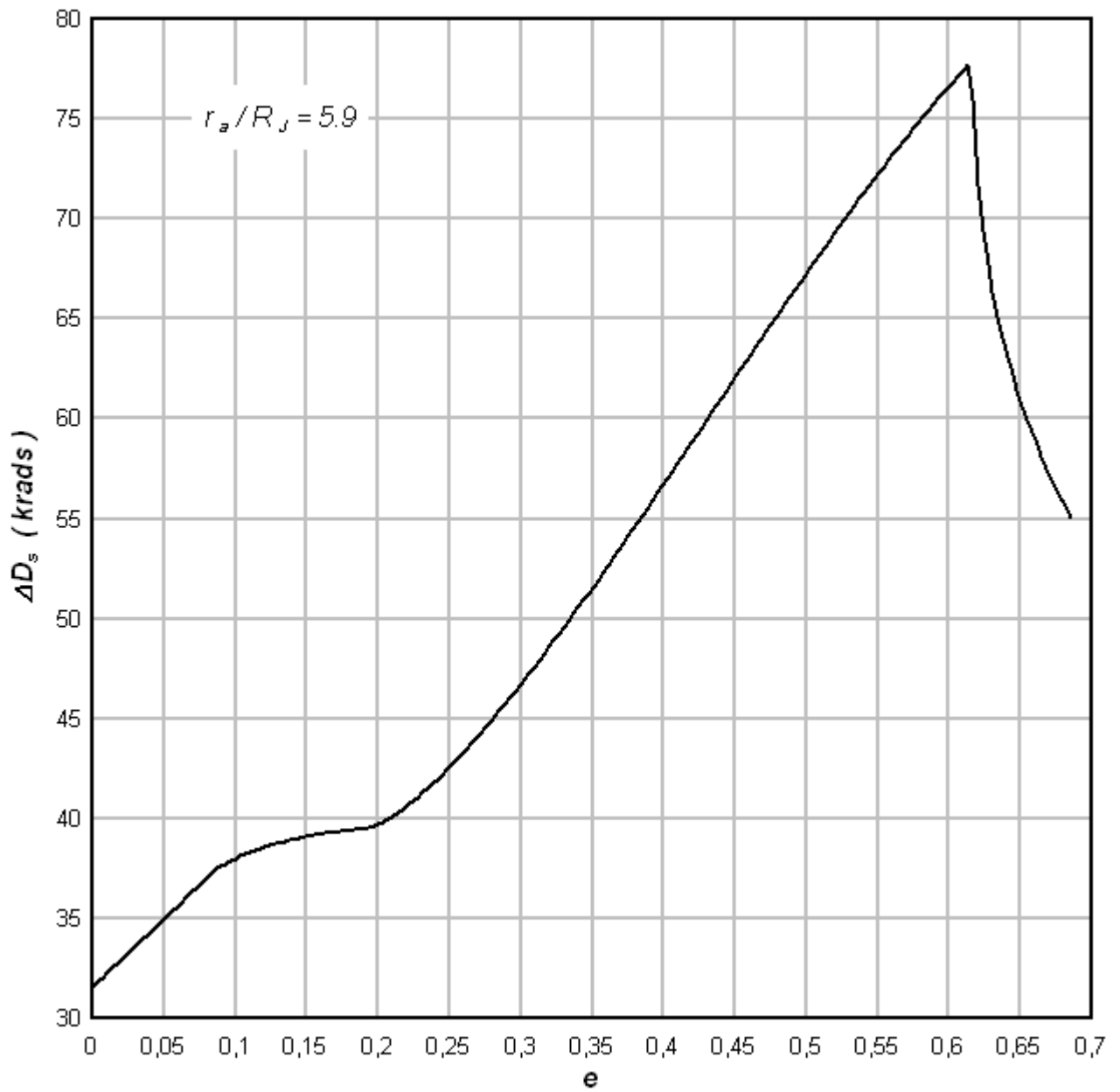


Figure 26. Radiation dose per orbit versus eccentricity for apojoive at the *Io* orbit, and 10 mm Al shield thickness.

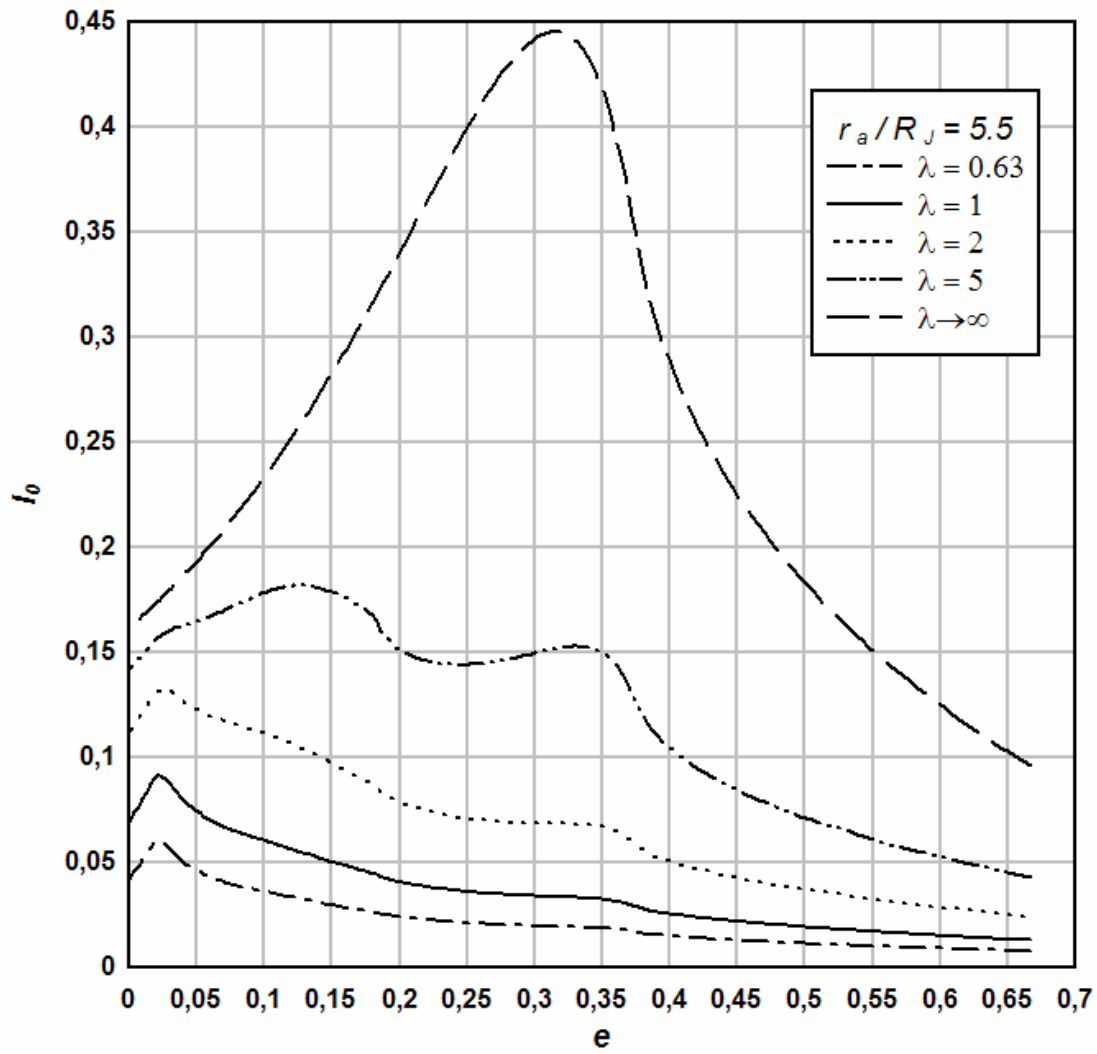


Figure 27. Same as in Figure 26, for apojoive at $5.5 R_J$ and the highest “mean” density in Fig. 2.

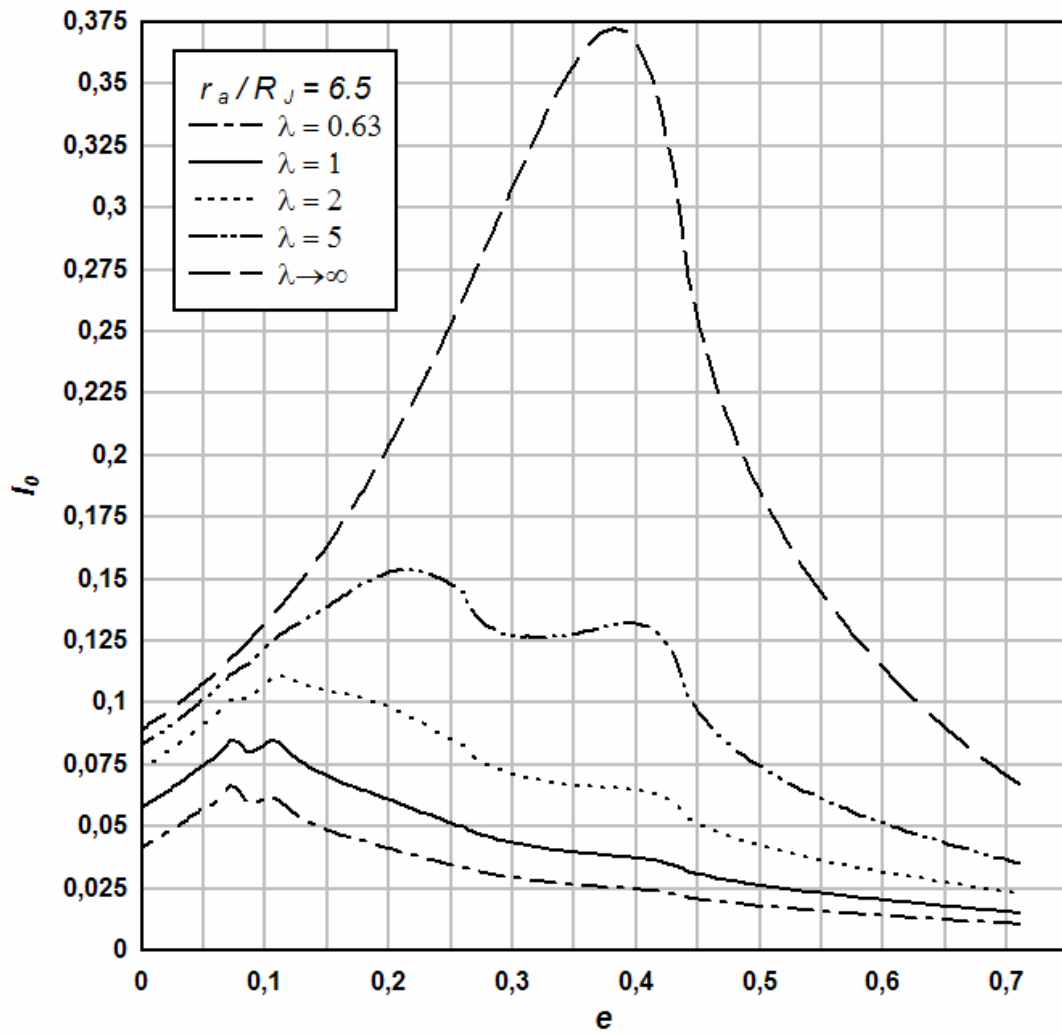


Figure 28. Same as in Figure 26, for apojoive at $6.5 R_J$

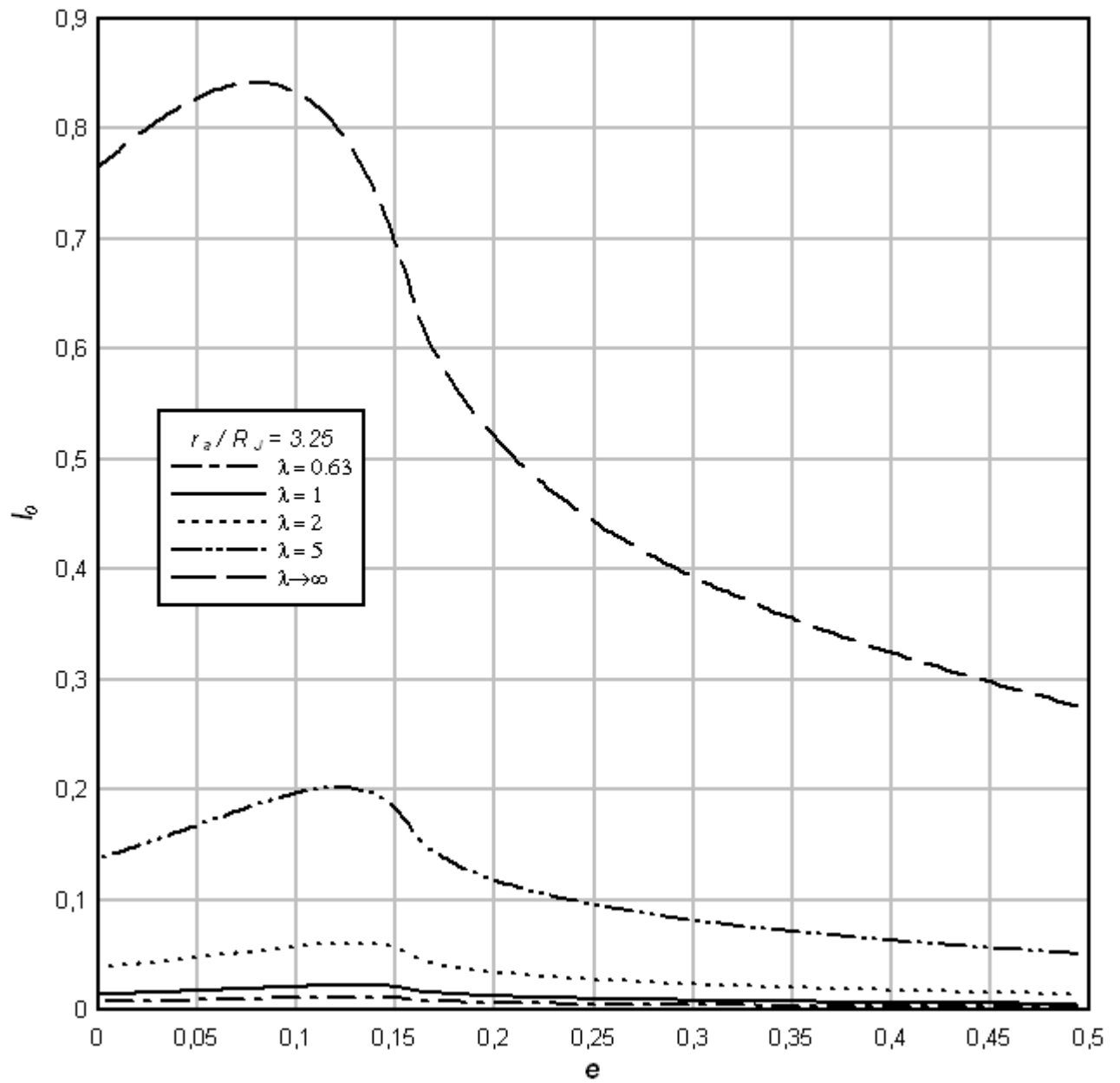


Figure 29. Same as in Figure 26, for apojoive at $3.25 R_J$

8 – Conclusions

Future ESA/NASA missions to the Jovian system face technology issues particularly concerning both power and propulsion. This is the more so as regards ESA's power needs. This Study on ED-tether missions to Jupiter has addressed those issues.

8.1 – Tethered-SC capture operation and constraints

The critical phase for the Jovian mission is SC capture; closed orbits can substantially evolve afterwards under repeated Lorentz force. The issue was whether a ED tape-tether can capture a SC, with full mass M_{SC} a few times tether mass m_t , into an equatorial, highly elliptical, low perijove orbit at Jupiter.

Design parameters, tape length L and thickness h , and perijove radius r_p , face opposite criteria. A high mass-ratio M_{SC} / m_t requires a low perijove and (in the weak ohmic-effects limit best representing conditions at the Jovian mission) a high $L^{3/2}/h$ ratio (i.e. a relatively long and thin tape). Low gravity gradients and high lateral Lorentz forces at Jupiter make a tether spin ω_t necessary (HCs at both tether ends take turns in becoming cathodic as the tether rotates). Tether tensile stress scales as $\rho_t \omega_t^2 L^2$ ($\rho_t \equiv$ tether density) while tether bowing from the Lorentz force scales as $L^{1/2} / h \rho_t \omega_t^2$, or $L^{5/2} / h$ for a given upper bound on stress.

Also, tether temperature is in thermal equilibrium both local and quasisteady, heating and radiated power keeping nearly equal at each point as the tether rotates. In the weak ohmic effects limit, heating arises from the impact of collected electrons, and maximum temperatures occur at tether ends, even though they only receive heating when acting anodically, i.e. half the time. Maximum tether temperature scales as $L^{3/8} / \varepsilon_t^{1/4}$, with ε_t being tether surface emissivity. Beyond limiting tether length, an acceptable temperature around

perijove will require coating the tape to reach values $\varepsilon_t \approx 0.8$. In addition, both tether temperature and bowing are greater the closer to Jupiter is the perijove.

A preliminary design that sets a mass ratio $M_{SC} / m_t \approx 3$ and the perijove at $1.5 R_J$, and uses a coated *Al* tape that is 80 km long and 0.05 mm thick, with emissivity $\varepsilon_t \approx 0.8$ and a 20 minutes spin, satisfies all constraints, though it barely captures the SC. Capture may be eased by decreasing the excess hyperbolic velocity below the Hohmann-transfer value, about 5.6 km/s, and reducing both ρ_t and h : with ohmic effects weak, the tape cross section need not be all conductive; it could be partly made of aluminium and partly of fiber, e. g. *Kevlar*, to both reduce density and increase tensile strength (and prevent tape tearing).

No characteristic dimensionless number involves the tape width w , which may easily range from 1.5 cm to 15 cm. The upper end arises from OML-regime validity considerations, with the thermal electron gyroradius reaching a minimum value during capture about 7.5 cm. Below $w = 1$ cm, there might be an issue of survivability to micrometeoroid cuts. For a 3 cm wide tape, m_t and M_{SC} would be 324 kg and 972 kg respectively; the spacecraft mass will just scale up with w , from 500 kg to 5000 kg for the width range above.

If ignoring thermal and bowing considerations, tether current at capture could be increased by decreasing r_p and $h/L^{3/2}$ but would be ultimately limited by ohmic effects to a (short-circuit) value independent of ambient plasma density. Ambient conditions could then only affect the capture mass ratio through the planetary magnetic field B . In the capture region, B (for both Jupiter and *Saturn*) is dominantly produced by currents inside the planet, a magnetic-dipole field approximation being valid for estimates. It was found that, in the case of Saturn, where B is 20 times smaller than at Jupiter, a ratio M_{SC} / m_t below unity appears required for tether capture, which would appear make it impossible.

8.2 - Tether-operated Jovian missions

Following capture, repeated application of Lorentz drag at perijove passes can efficiently lower the orbit apojove. This can give lead to three different mission profiles:

Mission 1. Frequent Galilean Moons Flybys

A tethered SC could rapidly and frequently visit Galilean moons. Elliptical orbits with (capture) perijove at about $r_p = 1.5 R_J$ and apojoves down at the Io, Europa and Ganymede orbits, are in resonances 1:2, 4:9, and 2:5 with the respective moons. For the design tape, about 25 *slow* flybys of Io could take place before the accumulated radiation dose exceeds 3 Mrad(Si) with 10 mm Al shield thickness, for a total mission duration of over 5 months after capture. The respective number of flybys for Ganymede would be 12, with total duration of about 9 months.

Mission 2. Low Circular Jovian Orbit

A tethered SC could acquire a safe, low circular orbit around Jupiter (below the radiation belts) and manoeuvre to get an optimal altitude, with no major radiation effects in less than 5 months after capture. A 80 km long, 0.05 mm thick tape, if several centimeters wide, could survive 1 year in the Jovian environment with probability very close to unity, allowing all three missions here.

Mission 3. Low Circular Orbit at Io

By thrusting at the apojove once down at the torus, in order to raise the perijove from the plasmasphere, a tethered SC could acquire a low circular orbit around moon Io in about 4 months, or 8 months after capture. This corresponds, however, to well over one hundred apojove passes, torus thrusting being weak; the accumulated radiation dose, about 7.5 Mrad(Si), poses a critical issue.

Again, accumulated radiation dose for all three types of missions could be reduced by decreasing tape thickness and density. Also, thrusting at the torus to raise the perijove in Mission 3 is more efficient the higher the perijove; preliminary use of rocket thrust for

limited perijove rise could skip tether thrusting at inefficient apojove passes. Once a full orbit is inside the torus, raising the apojove to moon Europa through a series of (torus) perijove passes would again face a radiation issue.

8.3 - Main pending issues for further study

Basic standing issues concern high radiation dose and model uncertainties in plasma density. Radiation damage could effectively block Mission 3, which will require advances in electronics hardening, and a design that allows greater shielding (use of ESA's **HIPS**). As regards plasma modeling, the capture operation requires an accurate inner-plasmasphere description, whereas Mission 3 is strongly affected by uncertainties in torus radial and latitudinal profiles; beyond a factor of 2 error in published ion temperatures entering the Divine/Garrett model, late Galileo data suggest plasma density in the torus is higher by a factor of 2 than indicated by Voyager data, while there are reports of greater latitudinal extent in the torus "ribbon" region.

Issues deserving further detailed study include:

- Sensitivity of performance to uncertainties and temporal variations in plasma density at the inner plasmasphere and in torus latitudinal extent. A mismatch between model and actual values would be particularly problematic for the critical capture phase in all three Missions. Possible temperature differences among species and possible temperature anisotropies keep a degree of uncertainty in torus thickness, affecting Mission 3; also, recent analyses from a Cassini flyby show long term variations in plasma conditions in the Io torus, from the Voyager 1, 2 era, but also monthly and even hourly variations.
- A thorough determination of radiation dose per orbit and accumulated dose for all three missions.
- Assuming the SC in Io orbit, use of the Lorentz force to make that orbit stable against the pull of Jupiter. The radius of the 'sphere of influence' of Io against its planet is only 7200

km, Io's radius itself being 1820 km. Galileo data showed that Io has a substantial ionosphere, with electron densities at hundreds of kilometers above Io's surface reaching values $\sim 10^5 \text{ cm}^{-3}$, well above the ambient magnetospheric density; and with plasma that arises from Io, and goes into its torus, corotating with the Jupiter's magnetosphere at distances from Io's center as close as 7 times Io's radius, or about 13,000 km only.

- Both tether lateral dynamics and the long-term effect of the Lorenz torque on tether spin. Deployment uses 2-phase, in-line / off-line rocket thrust that provides temporary spin with no mass penalty on capture and tour operations. Off-line rocket thrust would also provide the 20 minutes spin (opposite the Jupiter spin), that eases tether dynamics and keeps it taut.
- Detailed power strategy in using electrical energy generated over high-current segments of orbits, and saved/stored in regenerative fuel cells / batteries, to cover overall power needs; in particular, the possibility of powering electric propulsion at the critical thrusting needs for Mission 3.
- Radiation impedance for tether-circuit current closure in the Jovian plasma, throughout the missions above.
- Detailed selection of tape materials, when considering tensile stress and possibly large thermal excursions in the tether.
- Detailed analysis of survivability of tapes to hypervelocity micrometeoroid impacts in case of Mission 2, which could be extended for several years.
- Detailed design of conductive-tape deployer.
- Mission cruise analysis on the reduction of the excess hyperbolic velocity.